The Dynamics, Stability and Manifestation of Circumbinary Orbits

Samuel Doolin

Balliol College
University of Oxford

A thesis submitted for the degree of
Doctor of Philosophy
2012

To my family

Statement of Originality

The work presented within this thesis is believed to be original, and is a direct result of my own research. Explicit references are made to the works of other authors where these are discussed. No part of this thesis has been, or is being, submitted for any other qualification other than the degree of Doctor of Philosophy at the University of Oxford.

Sam Doolin

Samuel Doolin
August 22, 2012

Abstract

I numerically investigate the dynamics of orbits in 3D circumbinary phase-space as a function of binary eccentricity and mass fraction. I find that inclined circumbinary orbits in the elliptically-restricted three-body problem display a nodal libration mechanism in the longitude of the ascending node and in the inclination to the plane of the binary. I analyse and quantify the behaviour of these orbits and investigate their stability over time. This work is the first dynamically aware analysis of the stability of circumbinary orbits across both binary mass fraction and binary eccentricity. This work also has implications for exoplanetary astronomy in the existence and determination of stable orbits around binary systems.

I also present an examination of the so-called radio ruff around the microquasar SS433, which I show to precess on a timescale of approximately 550 days. The observed precession in the projected angle of the ruff on the sky may be explained if the ruff feature arises from an inclined circumbinary excretion disk. In addition, I describe a pilot study in the near-infrared waveband in search of circumbinary material around other microquasars.

Acknowledgements

First and foremost I would like to thank my supervisor Katherine Blundell for her excellent guidance, enthusiasm and support. It has been an honour and a privilege to work with Katherine and *"los gatitos"* Paul and Sebastián.

I count myself fortunate to have worked within the Oxford Astrophysics department, which has provided a stimulating environment and a wonderful community. My thanks to everyone who has made this so, and especially to those who travelled with me through our postgraduate years — Sam, Calum, Ben, Emma, Graeme, Nic, *et al.*, and our older and younger colleagues.

I would like to thank the Science and Technology Facilities Council for supporting my postgraduate studies. And also to Balliol College and the lovely postgraduate community at Holywell Manor which has been my home for some years.

I am incredibly grateful to my amazing friends from Balliol College, my housemates Chris, Mike and Beth, and my older friends from St John's College and The North.

Many thanks to my parents for everything, amongst which their upbringing, kindness, support and belief. And a final word of thanks to the people who have been incredibly supportive during difficult times — Sam, Calum and Amy.

“ A table, a chair, a bowl of fruit and a violin;
what else does a man need to be happy? ”

Albert Einstein

Contents

List of Figures

Chapter 1

Introduction

1.1 Circumbinary Orbits

The recent discovery of a circumbinary disk around the microquasar SS433 (Blundell et al., 2008) along with evidence that such disks may be dynamically coupled to the accretion and outflow from such active systems (Artymowicz and Lubow, 1996; Regös et al., 2005; Doolin and Blundell, 2009; Perez M. and Blundell, 2010) led me to investigate the behaviour of orbits encompassing binary systems.

In the course of my studies I discovered a libration mechanism in the longitude of the ascending node and inclination to the plane of the binary of all inclined circumbinary orbits. This behaviour is explored in detail in Chapter 3, but essentially corresponds to the observation that test particles in inclined circumbinary orbits do not remain in one orbital plane, but their orientation to the plane of the binary evolves over time. I also investigate the long term stability of these circumbinary orbits.

An unknown but significant fraction of stars are confined to multi-stellar systems, indeed whilst different authors quote differing figures the consensus is of a fraction $\geq 50\%$. Yet in this era of exoplanetary astronomy, with new planets being discovered almost every week, only a minority of those so far known are in binary systems (Raghavan et al., 2006). And further still, only a small number of these are circumbinary in nature (e.g. Lee et al., 2009; Beuermann et al., 2011; Qian et al., 2011; Doyle et al., 2011). The circumbinary regime is therefore an under-explored but possibly fruitful region in which to search for exoplanets. With new technologies and methods to detect circumbinary planets (e.g. Schwarz et al., 2011), it is crucial that we understand the dynamics and stability of circumbinary orbits.

1.1.1 A metaphor with marbles

The numerical studies which comprise the first chapters of this thesis may be visualised as follows: Imagine yourself in a dark room with an irregular floor which you cannot see. Perhaps the floor is carpeted with black cloth, but in any case you cannot tell if it is flat or not. In your possession you have a bucket of marbles (which are conveniently easy to see). To work out where the bumps and holes are in the floor you could roll some marbles out in front of you, and by observing their path, as influenced by the unseen structure of the floor, you could infer which regions of the floor are higher or lower than others.

In much the same manner I investigate the elliptically restricted three body problem by “rolling” millions of test particle “marbles” around in the 3D gravitational potential of a computed binary system and monitoring their behaviour.

1.2 Circumbinary Structures

In the latter chapters of this thesis I consider the observational appearance and manifestation of circumbinary structures. First I investigate the radio-ruff of the microquasar SS433, the angle of which precesses on the sky. I consider whether this outflow could be due to an circumbinary excretion disk (as suggested by Blundell et al., 2008 and others), which, if inclined, would precess in the longitude of the ascending node relative to the plane of the binary, and hence could produce the observed ruff evolution.

Finally I present the first results from a pilot spectroscopic survey in search of circumbinary disks around other Galactic microquasars. Such structures could actively influence the mass flows within and emanating from microquasars, and provide diagnostics of the internal behaviours of these complex systems. Given the stability of mass in circumbinary orbits we should not presume any given binary system to lack a circumbinary component unless otherwise demonstrated. Such a component may be a source of obscuration, emission, inflow or outflow.

1.3 Outline of thesis chapters

In Chapter 2 I describe the numerical methods employed in the following two chapters: Chapter 3, in which I investigate the dynamics of circumbinary orbits; and Chapter 4, where I consider the long-term stability of circumbinary orbits. In Chapter 5 I introduce a special class of stars known as microquasars and discuss their observational appearance. I also introduce the microquasar SS433, which is one of the most highly studied objects in our Galaxy besides the Sun. In Chapter 6 I investigate the precession of SS433's radio ruff on long timescales. And in Chapter 7 I present the first results of my search for circumbinary disks around other microquasars. Chapter 8 concludes.

Chapter 2

Numerical Framework

In this chapter I describe how numerical methods are employed to investigate the dynamics and stability of cirumbinary orbits that are described in later chapters.

2.1 Tools

The main body of my numerical code was written in the programming language "C", which is a compiled procedural language. C provides low-level access to memory with pointers and dynamic memory allocation. It has a low runtime demand on system resources and is known to compile to efficient code. We used double-precision floating-point arithmetic throughout the code to allow for greater numerical accuracy.

The simulation data are stored in a MYSQL relational database. This provides a highly organised, efficient and flexible method to manage the $\sim$ 50GB of data explored in this thesis. The database maintains relationships between data — for example, every test particle belongs to one simulation — which enforces consistency and allows for logical data manipulation.

We interrogate the database via SQL queries, taking advantage of the underlying database relationships, and allowing for complex questions to be asked of the data irrespective of the underlying storage mechanism.

Data are analysed in PYTHON, which is an interpreted higher-level programming language. PYTHON is a very powerful platform for both interactive and scripted data analysis (and visualisation) using modules such as NUMPY and MATPLOTLIB. We use the PYTHON module MYSQLDB to query the MYSQL database.

2.2 Orbits in two dimensions

We first solve the two-body problem for the orbit of two masses M_1 and M_2 situated at locations $\mathbf{r}_1$ and $\mathbf{r}_2$, and attracted to one another by a gravitational force given by Newton et al. (1729):

$$\mathbf{F} = -\frac{GM_1M_2}{r^2}\hat{\mathbf{r}}, \tag{2.1}$$

where G is the universal gravitational constant and $\mathbf{r} = \mathbf{r}_2 - \mathbf{r}_1$. The equations of motion for $\mathbf{r}_1$ and $\mathbf{r}_2$ are therefore given by

$$\begin{aligned} M_1\ddot{\mathbf{r}}_1 &= -\mathbf{F} \\ M_2\ddot{\mathbf{r}}_2 &= \mathbf{F}. \end{aligned} \tag{2.2}$$

The problem may be reduced from the coupled equations above by considering the relative acceleration between the bodies (e.g. Green, 1985):

$$\ddot{\mathbf{r}} = \ddot{\mathbf{r}}_2 - \ddot{\mathbf{r}}_1 = -\frac{G(M_1+M_2)}{r^2}\hat{\mathbf{r}}. \tag{2.3}$$

Writing $\mathbf{r}$ in polar coordinates, $\mathbf{r}(r, v)$, where r is the radius and v the polar angle (true anomaly), we extract the coupling between r and v through Equation 2.3 via the eccentric anomaly E:

$$\begin{aligned} r &= a(1 - e\cos E) \\ \tan\frac{v}{2} &= \sqrt{\frac{1+e}{1-e}}\,\tan\frac{E}{2}. \end{aligned} \tag{2.4}$$

Here we have introduced the standard ellipse notation for r, with semi-major axis a and eccentricity e. $E = 0$ corresponds to the point of perihelion (or periastron) — $\min|\mathbf{r}|$, and $E = \pi$ to the point of aphelion (apastron) — $\max|\mathbf{r}|$. E rotates through 2π over the course of one orbit but is non-linear in time.

Defining the mean motion n by

$$n^2a^3 = G(M_1 + M_2) \tag{2.5}$$

we obtain a quantity which is linear in time. This quantity is the mean anomaly M, which increases linearly in time proportional to the mean motion n, and defines the time dependence of the eccentric anomaly $E(t)$ via Kepler's equation:

$$M = nt = E - e\sin E. \tag{2.6}$$

Incidentally, as the mean anomaly M rotates through 2π in one orbital period P, and substituting Equation 2.5, we obtain Kepler's third law:

$$\frac{a^3}{P^2} = \frac{G(M_1 + M_2)}{4\pi^2}. \tag{2.7}$$

> “The square of the orbital period of a planet is directly proportional to the cube of the semi-major axis of its orbit.”

2.3 A simulated binary

In our simulations we integrate test particles around binary systems of various eccentricities e_{b} and mass fractions α_{b}. Fixing the free parameters in the derivation of § 2.2 we obtain the position of the binary as a function of time. First we fix the centre of mass of the system to the origin

$$\begin{aligned} M_1\mathbf{r}_1 + M_2\mathbf{r}_2 &= 0 \\ M_1\dot{\mathbf{r}}_1 + M_2\dot{\mathbf{r}}_2 &= 0. \end{aligned} \tag{2.8}$$

Second, we choose an appropriate coordinate system to describe the motion. In our simulations this equates to setting the orbital plane of the binary to be the xy plane by parameterising the vector $\mathbf{r}$ in 3D polar coordinates $\mathbf{r}(r, v, z)$, where r is radial in xy, v is the polar angle (true anomaly), and $z = 0$.

And third, with sufficient care taken in the rotation of $\mathbf{r}(r, v, z)$ in the xy plane at $t = 0$ we set the binary to be at periastron, with the more massive star M_1 on the negative x-axis, and the less massive star M_2 on the positive x-axis. As time increases M_1 and M_2 orbit according to Equation 2.4, with M_1 down into the negative-x negative-y quadrant and M_2 moving up into the positive-x positive-y quadrant, anti-clockwise if one looks down on the xy plane.

But Kepler's equation (Equation 2.6) is non-linear, and hence solving for $E(t)$ is not simple. To do this we employ a root-finding algorithm on Equation 2.6. The procedure used is a combination of the bisection algorithm and the Newton-Raphson algorithm (Press et al., 1988). It steps iteratively from a guessed value E_1 in the vicinity of the root, increasing the accuracy of the solution with each iteration $E_2, E_3 \ldots E_n$.

The Newton-Raphson algorithm considers both the value of the function $f(E_{\mathrm{n}})$ and the value of the first derivative $f'(E_{\mathrm{n}})$ with respect to the variable in question, to estimate the next guess for the value of $E_{\mathrm{n}+1}$.

$$\begin{aligned} f(E) &= E - e\sin E - nt && (2.9)\\ f'(E) &= \frac{df}{dE} = 1 - e\cos E && (2.10)\\ E_{\mathrm{n}+1} &= E_{\mathrm{n}} - \frac{f(E_{\mathrm{n}})}{f'(E_{\mathrm{n}})}. && (2.11) \end{aligned}$$

This algorithm converges quadratically — that is to say that the number of significant digits of the solution approximately doubles with each step, especially given the smoothly varying first derivative of Kepler's equation.

The other half of the root-finding algorithm is a simple bisection step. This is only called for the initial guess and in the unlikely case that the Newton-Raphson algorithm predicts a bad next guess.

It is important that the root-finding algorithm gives a solution that is accurate enough to satisfy the requirements of the integrator (see § 2.5), but this is not a problem as the algorithm requires only a few low-cost steps to reach a very precise solution.

So to find the positions of the binary components at time t:

1. Find the root of Kepler's equation at time t.

2. Plug this value of the eccentric anomaly E into Equation 2.4 and solve for radius r and true anomaly v.

3. Convert $\mathbf{r}(r, v, z)$ into Cartesian coordinates $\mathbf{r}(x, y, z)$.

4. Calculate $\mathbf{r}_1$ and $\mathbf{r}_2$ from $\mathbf{r}$. The inverse transformation may be derived from Equation 2.8:

$$\begin{aligned}\mathbf{r}_1 &= -\frac{M_2}{M_1+M_2}\mathbf{r}\\ \mathbf{r}_2 &= +\frac{M_1}{M_1+M_2}\mathbf{r}.\end{aligned} \tag{2.12}$$

2.4 Orbits in three dimensions

2.4.1 Keplerian Orbital Elements

A general orbit in three dimensions is described intuitively by the Keplerian orbital elements (a, e, i, W, w, v) illustrated by Figure 2.1. The eccentricity e, semi-major axis a and true anomaly v describe the motion of a body in its orbital plane (as in § 2.2), whilst the inclination i, longitude of the ascending node W and argument of perihelion w describe the orientation of this orbital plane with respect to some reference plane and direction.

In this coordinate space all trajectories are uniquely represented, with a Keplerian orbit having the property of conserving all quantities but the true anomaly $v(t)$, which describes the exact position of a body on its orbital path.

The three angles i, W and w can be viewed as the Euler angles (Landau and Lifshitz, 1969) describing the orientation of the orbital plane with respect to the coordinate frame defined by the reference frame and direction.

In terms of intrinsic rotations, if one were to start in a reference frame as defined by the reference plane and direction (call it xyz) and seek to move to the frame of the orbit specified by (a, e, i, W, w, v) one would need to apply the following three rotations in succession:

1. rotate xyz about the z-axis by W

$$\mathbf{R}_W = \begin{pmatrix} \cos W & \sin W & 0 \\ -\sin W & \cos W & 0 \\ 0 & 0 & 1 \end{pmatrix}, \tag{2.13}$$

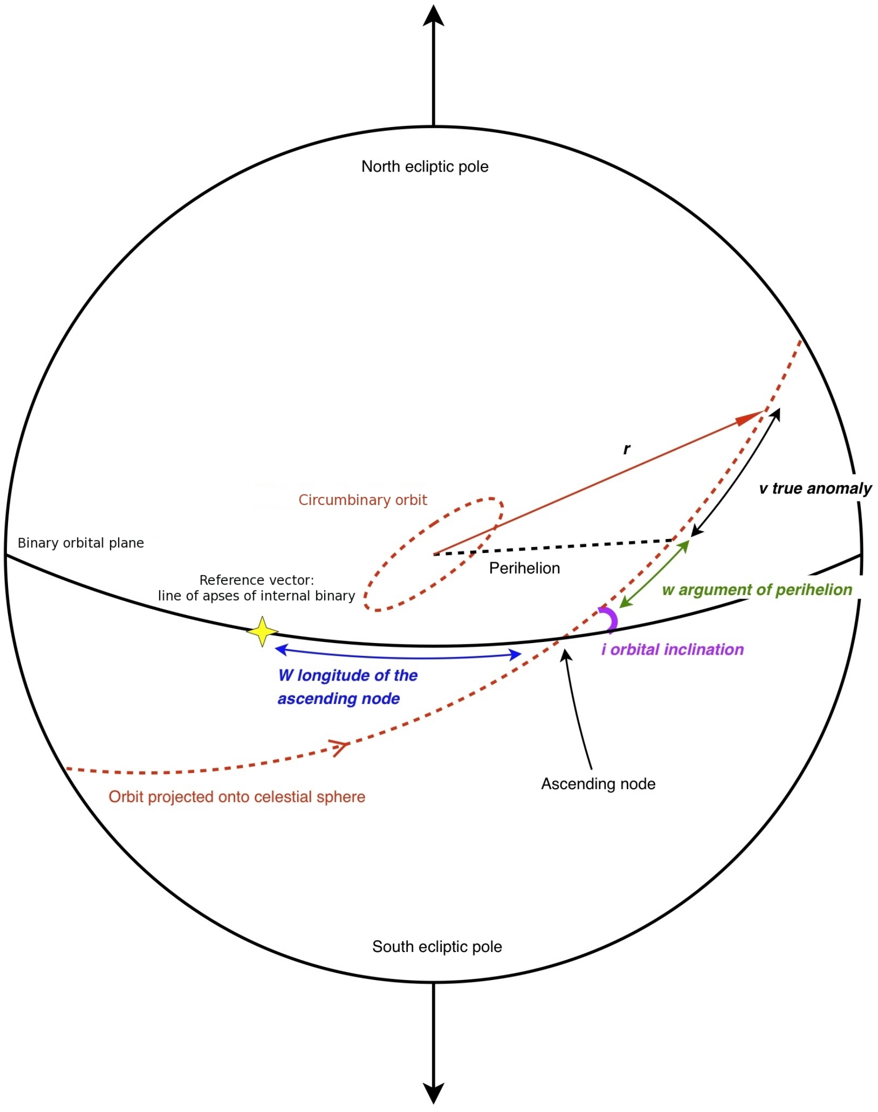

Figure 2.1: The Keplerian orbital elements.

2. rotate the new xyz about the x-axis by i

$$\mathbf{R}_i = \begin{pmatrix} 1 & 0 & 0 \\ 0 & \cos i & \sin i \\ 0 & -\sin i & \cos i \end{pmatrix}, \tag{2.14}$$

3. rotate the penultimate xyz a third time about the new z-axis by w

$$\mathbf{R}_w = \begin{pmatrix} \cos w & \sin w & 0 \\ -\sin w & \cos w & 0 \\ 0 & 0 & 1 \end{pmatrix}. \tag{2.15}$$

In the circumbinary case we define the reference plane as the natural plane of the internal binary, and the reference direction as the vector along the binary's line of apses (i.e. the binary system's semi-major axis). In our studies we consider the *osculating* orbital elements of test particles — that is to say their instantaneous orbital elements about the barycentre of the binary system.

2.4.2 State vector

Whilst the orbital elements of a test particle represent an informative and intuitive coordinate system they are computationally not very useful. The integrator (see § 2.5) operates in Cartesian coordinates, working with position and velocity, or equivalently a test particle's state vector $(x,\, y,\, z,\, v_x,\, v_y,\, v_z) = (\mathbf{r}, \dot{\mathbf{r}})$.

The transformations between state vectors and orbital elements are given below. A formal derivation may be found in Morbidelli (2002) amongst others. These transforms require an additional variable $\mu = G(M_1 + M_2)$ which parameterises the gravitational acceleration of the orbit.

2.4.3 Orbital elements $\longrightarrow$ state vector

This is the more straight forward of the two transformations. We first define two quantities p (related to the conservation of angular momentum) and r (the orbital radius):

$$\begin{aligned} p &= a(1-e^2) & (2.16)\\ r &= \frac{p}{1+e\cos v}. & (2.17) \end{aligned}$$

Next we derive the position and velocity of the orbit in the so-called "PQR frame" — the coordinate frame of the orbit itself, as defined by initial radius (P), velocity (Q) and angular momentum (R).

$$\begin{aligned} \mathbf{r}_{\text{PQR}} &= \begin{pmatrix} x \\ y \\ z \end{pmatrix}_{\text{PQR}} &= \begin{pmatrix} r\cos v \\ r\sin v \\ 0 \end{pmatrix} & \quad (2.18)\\ \dot{\mathbf{r}}_{\text{PQR}} &= \begin{pmatrix} v_x \\ v_y \\ v_z \end{pmatrix}_{\text{PQR}} &= \sqrt{\frac{\mu}{p}} \begin{pmatrix} -\sin v \\ e+\cos v \\ 0 \end{pmatrix}. & \quad (2.19) \end{aligned}$$

And finally we de-rotate out of this PQR frame back into the reference frame as defined by the reference plane and direction by carrying out the inverse of the rotations discussed in § 2.4.1 via the composite rotation matrix $\mathbf{R}$:

$$\mathbf{R} = \begin{pmatrix} \cos W & -\sin W & 0 \\ \sin W & \cos W & 0 \\ 0 & 0 & 1 \end{pmatrix} \cdot \begin{pmatrix} 1 & 0 & 0 \\ 0 & \cos i & -\sin i \\ 0 & \sin i & \cos i \end{pmatrix} \cdot \begin{pmatrix} \cos w & -\sin w & 0 \\ \sin w & \cos w & 0 \\ 0 & 0 & 1 \end{pmatrix} \qquad (2.20)$$

$$\mathbf{R} = \begin{pmatrix} \cos W \cos w - \sin W \sin w \cos i & -\cos W \sin w - \sin W \cos w \cos i & \sin W \sin i \\ \sin W \cos w + \cos W \sin w \cos i & -\sin W \sin w + \cos W \cos w \cos i & -\cos W \sin i \\ \sin w \sin i & \cos w \sin i & \cos i \end{pmatrix} \quad (2.21)$$

$$\begin{aligned} \mathbf{r} &= \mathbf{R}.\mathbf{r}_{\,\mathrm{PQR}} && (2.22) \\ \dot{\mathbf{r}} &= \mathbf{R}.\dot{\mathbf{r}}_{\,\mathrm{PQR}}. && (2.23) \end{aligned}$$

We have now recreated the state vector of the orbit $(\mathbf{r}, \dot{\mathbf{r}}) = (x,\, y,\, z,\, v_x,\, v_y,\, v_z)$.

2.4.4 State vector $\longrightarrow$ orbital elements

This transformation is a little more detailed. We must compute the Euler angles i, W and w from the $(\mathbf{r}, \dot{\mathbf{r}})$ state vector. First we derive the instantaneous velocity and radius

$$\begin{aligned} r^2 &= \mathbf{r}^T.\mathbf{r} && (2.24) \\ v^2 &= \dot{\mathbf{r}}^T.\dot{\mathbf{r}}. && (2.25) \end{aligned}$$

The semi-major axis a is given by

$$a = \left(\frac{2}{r} - \frac{v^2}{\mu} \right)^{-1}. \quad (2.26)$$

A value of $a < 0$ indicates an unbound orbit. Next we compute the quantities

$$\mathbf{h} = \mathbf{r} \times \dot{\mathbf{r}} \tag{2.27}$$

$$p = \frac{\mathbf{h}^T.\mathbf{h}}{\mu} = \frac{h^2}{\mu} \tag{2.28}$$

$$q = \mathbf{r}.\dot{\mathbf{r}}, \tag{2.29}$$

where **h** is the specific angular momentum vector, p is a conserved quantity relating to angular momentum, and q is a component which expresses how stretched the orbit is (a measure of velocity along the radius vector).

The remainder of the orbital elements are then extracted:

$$e = \sqrt{1 - p/a} \tag{2.30}$$

$$i = \arccos \frac{h_z}{h} \tag{2.31}$$

$$W = \arctan -\frac{h_x}{h_y} \tag{2.32}$$

$$v = \arctan \frac{hq}{h^2 - r\mu} \tag{2.33}$$

$$w = \arctan \left\{ \frac{r_z}{\sin i \times (r_x \cos W + r_y \sin W)} \right\} - v. \tag{2.34}$$

2.5 The Integrator

The integrator is the heart of the numerical code. It is responsible for evolving the state vector (position and velocity) of each test particle over the duration of the simulation according to the forces that it experiences. We apply a customised adaptive step-size fourth and fifth-order Runge-Kutta integrator (Press et al., 1988).

We model the restricted three-body system, which implies that the mass of a test particle is considered negligible. Each test particle is only aware of the binary system, and so we need not solve for a full gravitational potential but can take a simplified approach. We consider the acceleration of a typical test particle $\ddot{\mathbf{r}}_{\rm tp}$ at some time t where the binary stars M_1 and M_2 have positions $\mathbf{r}_1$ and $\mathbf{r}_2$.

$$\ddot{\mathbf{r}}_{\rm tp} = \mathbf{F}(\mathbf{r}_{\rm tp}) = \frac{GM_1}{|\mathbf{r}_1 - \mathbf{r}_{\rm tp}|^3}\,(\mathbf{r}_1 - \mathbf{r}_{\rm tp}) + \frac{GM_2}{|\mathbf{r}_2 - \mathbf{r}_{\rm tp}|^3}\,(\mathbf{r}_2 - \mathbf{r}_{\rm tp}). \tag{2.35}$$

This is an ordinary differential equation (ODE) of second order, which we reduce to a set of coupled first-order differential equations, such that for each of the six components of a test particle's state vector $(\mathbf{r}, \dot{\mathbf{r}})$ there exists a first-order differential equation:

$$\begin{aligned} \frac{d}{dt}\mathbf{r} &= \dot{\mathbf{r}} \\ \frac{d}{dt}\dot{\mathbf{r}} &= \mathbf{F}(\mathbf{r}). \end{aligned} \tag{2.36}$$

Each test particle is therefore represented by six numbers (its state vector). Whilst there are some additional derived quantities which persist for short times in the code for efficiency the overall the memory footprint is small.

The adaptive step-size fourth and fifth-order Runge-Kutta integrator (Press et al., 1988) is a standard, off-the-shelf component which we have customised to our requirements. It is a stepping algorithm which attempts to solve the differential equations by approximating the right-hand side of Equation 2.36 by a discrete function which may be numerically integrated in small steps from the initial conditions of the simulation to some specified final time.

The simplest form of this procedure is Euler's method. Consider some variable y which obeys the first order differential equation

$$\frac{dy}{dt} = f(y, t), \tag{2.37}$$

where the function $f(y,t)$ may be evaluated computationally. This equation is approximated numerically to

$$\triangle y = f(y,t)\triangle t, \tag{2.38}$$

and hence predicts the change in y in relation to a discrete change in t, otherwise known as the step size $h = \triangle t$. When Euler's method takes a step from $y(t)$ it predicts

$$y(t+h) = y(t) + hf(y(t),t). \tag{2.39}$$

It can be seen by comparing Equation 2.39 to a full Taylor expansion,

$$y(t+h) = y(t) + hy'(t) + h^2 y''(t)/2 + O(h^3), \tag{2.40}$$

that when Euler's method takes a step it neglects to account for terms in the Taylor expansion proportional to h^2 or higher, and hence the error incurred by taking a step of size h is proportional to h^2 (the local truncation error).

By subdividing each step into smaller hops it is possible to approximate the higher order terms in the Taylor expansion, and hence reduce the error incurred at the cost of doing more work for a given step size. The standard fourth-order Runge-Kutta algorithm costs four evaluations of Equation 2.36 per step and achieves a local truncation error $O(h^5)$.

In the scheme of Fehlberg (1969), the fifth-order Runge-Kutta algorithm costs six evaluations of Equation 2.36 per step to achieve a local truncation error $O(h^6)$. But remarkably Fehlberg (1969) also showed that a combination of the same six evaluations could reproduce the fourth-order approximation, hence calculating two estimates for each step. This fourth and fifth-order algorithm is often referred to as the Runge-Kutta-Fehlberg method.

With two estimates for each step, each of a different accuracy, the integrator has an inbuilt consistency check. Presupposing that fifth-order is better than fourth-order, the difference between the two gives the magnitude of the extra term $\propto h^5$ in the fifth-order estimate.

We may assume that this term represents an upper limit on the accuracy of the step taken, or "tolerance", and hence impose per-step requirements on this derived value. For example, if the error exceeds some maximum permitted value we go back, reduce the step size h, and try again. This is where an adaptive step-size algorithm pays dividends over a fixed step-size version. If the going is tough the algorithm is forced to be careful and take smaller steps, and yet if the going is easy we can try to increase the step size so long as the required accuracy is still attained.

We follow the methodologies laid out in Musielak et al. (2005) to ensure that we select a maximum permitted error such that numerical accuracy over the course of an entire simulation is sufficiently constrained, but that we do not seek to be excessively stringent at the cost of processor time. We employ a number of tests to constrain this tolerance:

1. A two-body case where test particles are set on initially circular orbits about a single point mass. Since the two-body problem is soluble we use deviations in test particle radius and orbital period from their analytic values over the course of a simulation to constrain numerical accuracy. The numerical tolerance is set such that these variations do not exceed 0.1%.

2. A subset of simulations drawn from the full suite of further chapters. Here a single simulation is repeated from identical initial conditions, but allowing for a variation in numerical tolerance. By comparing these simulations of differing numerical accuracies we select a maximum permitted error per step which specifies the point at which they show convergence, reproducing identical behaviour for our initial phase space sampling.

2.6 Test particles

Into these simulations I put a range of test particles to explore phase space. All test particles are set on initially circular orbits about the barycentre of the system. We sample radii out from some minimum to some maximum value, in units of the binary semi-major axis a_b.

After a few orbital periods the innermost test particles, experiencing the non-spherical tug of the binary's gravity most strongly, become unstable. The instability is manifested as particles on initially circular orbits about the centre of mass of the entire system are deflected to be captured by one of the central stars, or they may experience a gravitational kick that ejects them from the system.

2.6.1 Stability

An analytic approximation to the size of the region of gravitational influence of one body M_2 of a binary system $M_1 - M_2$ is given by the Hill radius (Morbidelli, 2002)

$$r_{\mathrm{H}2} \approx a_\mathrm{b} \left(\frac{M_2}{3M_1} \right)^{1/3} . \tag{2.41}$$

Since the Moon is close enough to the Earth (within the Earth's Hill radius) it primarily orbits the Earth, whilst the other planets (further from the Earth than its Hill radius) orbit the Sun.

In our case we are primarily interested in circumbinary orbits. From our initial sampling of phase space we check for test particles which remain in circumbinary orbits for the duration of a simulation. Those which approach either star too closely (within it's region of gravitational influence (Hill radius)) are considered unstable. Such test particles are either scattered by a close approach or fall into circumstellar orbits. In either case the numerical cost of maintaining these test particles is high and so the code catches them, marks them as unstable, notes the time at which the instability was caught, and removes them from the simulation.

A check is performed every n steps, where $n \sim$ hundreds, to identify unstable particles which are too close to either star or have attained escape velocity. These test particles are rejected from the simulations and the precise scattering is not computed.

In addition, post-simulation stability criteria are applied to identify and reject test particles which approach, but do not quite reach escape velocity at any time during integration.

2.7 Snapshots

The code is capable of outputting regular snapshots of either the state vector or the orbital elements of test particles. The state vector is not particularly informative and so the orbital elements are considered. We track the orbital elements of each test particle about the centre of mass of the binary during integration, outputting time-lapsed snapshots to a database.

2.8 Conventions

In the forthcoming chapters a parameter with the subscript “b” refers to a quantity of the internal binary system, such as binary eccentricity e_{b}, whilst parameters lacking such a subscript refer to the properties of the test particles.

With regards to the simulated binary we take the convention that $M_1 \geq M_2$, such that the binary mass fraction α_{b} lies in the range $0 < \alpha_{\mathrm{b}} \leq 0.5$, as defined by

$$\alpha_{\mathrm{b}} = M_2/(M_1 + M_2). \tag{2.42}$$

Chapter 3

The Dynamics of Circumbinary Orbits

The work presented in this chapter is based on Doolin and Blundell (2011).

3.1 Suite of simulations

This chapter concerns our first suite of simulations, which was designed to be extensively time-sampled to resolve and expose the dynamics of circumbinary orbits. This suite of simulations consists of 35 separate numerical experiments, each considering a synthetic binary system of prescribed eccentricity and mass-fraction. The binary parameter-space sampling is laid out in Table 3.1. In each simulation we integrate 5616 circumbinary test particles, sampling a wide range of possible circumbinary orbits, integrated for a total of 10^4 binary orbital periods. The initial phase-space sampling of test particles is laid out in Table 3.2. To constrain behaviour in the large-radius limit one additional spherical shell of 312 test particles at a semi-major axis $50a_\mathrm{b}$ was also integrated for $5 \times 10^6 T_\mathrm{b}$.

Table 3.1: Sampling of binary eccentricity and mass fraction

Orbital Element	min	max	$\triangle$
eccentricity e_{b}	0	0.6	0.1
mass fraction α_{b}	0.1	0.5	0.1

Table 3.2: Sampling of circumbinary phase space.
a_{b} = binary semi-major axis and T_{b} = binary orbital period.

Orbital Element	min	max	$\triangle$
semi-major axis a	$1.5a_{\mathrm{b}}$	$10a_{\mathrm{b}}$	$0.5a_{\mathrm{b}}$
inclination i	0	π	$\pi/20$
longitude of the ascending node W	0	2π	$\pi/2$
true anomaly v	0	2π	$\pi/2$
simulation length and snapshot $\triangle t$		$10^4 T_{\mathrm{b}}$	$10 T_{\mathrm{b}}$

3.2 A circumbinary nodal libration mechanism

As a typical test particle is integrated over the course of a simulation its orbital elements (§ 2.4.1) about the centre of mass of the system are closely monitored and recorded every 10 binary orbital periods. When examining these snapshots we noticed that the inclination i and longitude of the ascending node W of test particles exhibited tendencies to vary systemically. W either precesses through 360° or oscillates around some value, whilst i is coupled to oscillate in phase with W but at twice the frequency.

This behaviour is best illustrated in a plot of i against W, where the evolutionary history of a test particle is revealed. Since these coordinates correspond physically to angles, and W exhibits a tendency to precess, we use polar $(i \cos W, i \sin W)$ coordinates to examine test particle behaviour (Figure 3.1). A plot of this type represents a particular slice through parameter space and may be termed a surface of section. Each line in Figure 3.1 is traced out by an individual test particle over the course of a simulation.

Figure 3.1 reveals a nodal libration mechanism which couples the inclination i and

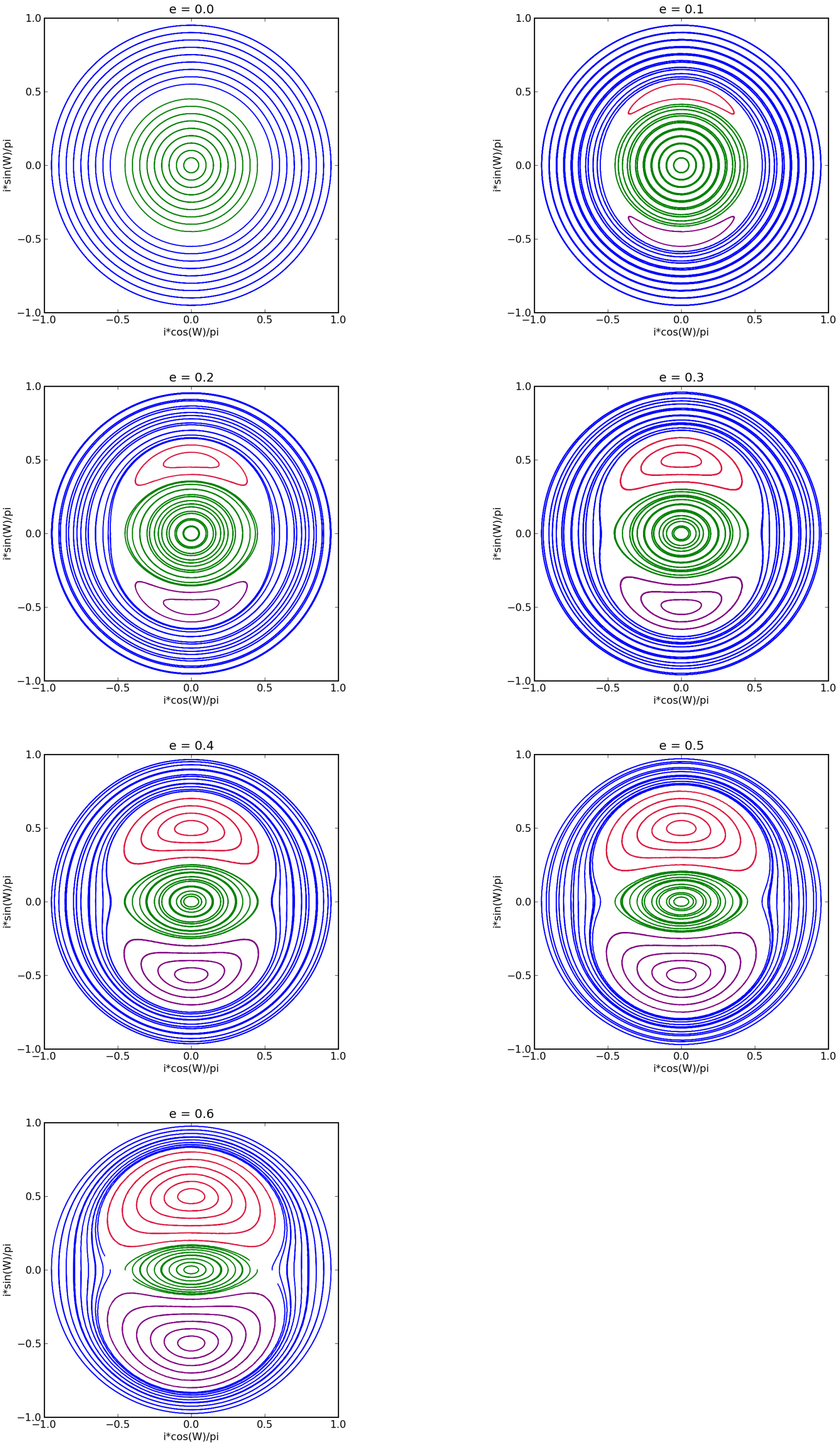

Figure 3.1: The $(i\cos W, i\sin W)$ surface of section for circumbinary orbits as a function of binary orbital eccentricity e_{b}. This geometry is both mass fraction and radius independent.
Green: prograde $(i < \pi/2)$. Precession is clockwise.
Blue: retrograde $(i > \pi/2)$. Precession is anti-clockwise.
Red: island of libration centred at $(i = \pi/2, W = \pi/2)$. Precession is anti-clockwise.
Purple: Island of libration centred at $(i = \pi/2, W = -\pi/2)$. Precession is anti-clockwise.

longitude of the ascending node W of all inclined circumbinary orbits. This mechanism divides phase-space into four distinct populations, which are now examined in turn.

3.2.1 Prograde orbits *(green)*

An inclination $i = 0$ corresponds to a coplanar prograde circumbinary orbit. Orbits of inclination $0 \leq i < \pi/2$, whilst not necessarily coplanar, we refer to as prograde. The prograde region of phase space therefore extends out from the centre ($i = 0$) of the surface of section (Figure 3.1) and encompasses all orbits of a similar behaviour.

Prograde orbits exhibit a precession in the longitude of the ascending node W. This evolution in W produces clockwise paths around the surface of section shown in Figure 3.1.

3.2.2 Retrograde orbits *(blue)*

An inclination $i = \pi$ corresponds to a coplanar retrograde circumbinary orbit. Orbits of inclination $\pi/2 < i \leq \pi$, whilst not necessarily coplanar, we refer to as retrograde. The retrograde region of phase space therefore extends inwards from the outer limit ($i = \pi$) of the surface of section (Figure 3.1) and encompasses all orbits of a similar behaviour.

Retrograde orbits exhibit a precession in the longitude of the ascending node W. But counter to the prograde orbits, the retrograde evolution in W produces anti-clockwise paths around the surface of section (Figure 3.1).

We expect that the precession in W observed in close-to-coplanar prograde and retrograde orbits is due to a coupling between the specific angular momentum of test particles on inclined orbits and the $\hat{z}$ angular momentum of the binary. Such a coupling would exert a torque on the test particle producing a precession in the ascending node, akin to gyroscopic precession.

3.2.3 Islands of libration *(red & purple)*

An inclination $i = \pi/2$ corresponds to a circumbinary orbit which is exactly perpendicular to the binary plane. Figure 3.1 shows two very clear libration islands centred on $i = \pi/2$, $W = \pm\pi/2$. A test particle on an orbit within a region of libration has its inclination i and ascending node W coupled to precess about the centre of libration. For both regions of libration this precession is anti-clockwise.

3.3 The geometry of the surface of section

The geometry of the $(i \cos W, i \sin W)$ surfaces of section shown in Figure 3.1 reveal a dependence on the internal binary eccentricity. More specifically, the extent of the two regions of libration can be seen to scale with binary eccentricity. A circular binary $e_\mathrm{b} = 0$ exhibits no libration islands, whereas for a binary of $e_\mathrm{b} = 0.6$ the libration mechanism is becoming the dominant behaviour in phase space. We quantify the extent of the libration regions in § 3.7.

Inspection of surfaces of section across values of binary mass fraction α_b and radius a lead us to conclude that the geometry is both mass fraction and radius independent. The period of the precession of each test particle however does show a strong dependance on both α_b and a, as explored in § 3.9.

3.4 Kozai cycles

The geometry of the polar (i,W) surface of section (Figure 3.1) with its islands of libration appears similar to that of the Kozai mechanism. Kozai (1962) showed analytically that an inclined *circumstellar*[1] orbit may experience an oscillating exchange between inclination

---

[1] An orbit about one star of a binary system. ‘S-type’ (Dvorak et al., 1989).

and eccentricity, and also a libration in the argument of perihelion. But whilst the *circumstellar* (i,w) plane may share similarities with our *circumbinary* (i,W) plane, we are dealing with a very different regime of the elliptically-restricted three-body problem.

3.5 Symmetry

The $(i \cos W, i \sin W)$ surface of section (Figure 3.1) is a 2D projection of the surface of a unit sphere (see Figure 3.2), where i corresponds to the polar angle and W to the azimuthal angle. The central point of the surface of section ($i = 0$) corresponds to a coplanar prograde orbit and at this point the longitude of the ascending node W is undefined. Equivalently one may regard this $i = 0$ point as situated at the north pole of a sphere, with the south pole at $i = \pi$ (a coplanar, retrograde orbit). Points of $i = \pi/2$ identify the equator. This type of spherical projection is known in cartographic circles as the azimuthal equidistant projection.

This unit sphere (Figure 3.2) essentially defines the direction of the specific angular momentum vector $\vec{h}$ of a test particle. We note three particular planes of symmetry through this sphere. These may be specified by considering components of a circumbinary orbit's specific angular momentum $\vec{h}$ along axes (i) parallel to the line of apses of the binary, (ii) perpendicular to the line of apses of the binary and yet remaining in the binary orbital plane, and (iii) perpendicular to the plane of the binary. We show these three planes of symmetry in Figure 3.3 via the colours:

green:	$i = \pi/2$	$h_z = 0$
blue:	$W \in \{0, \pi\}$	$h_{\|\text{apses}} = 0$
red:	$W \in \{\pi/2, 3\pi/2\}$	$h_{\perp\text{apses}} = 0$

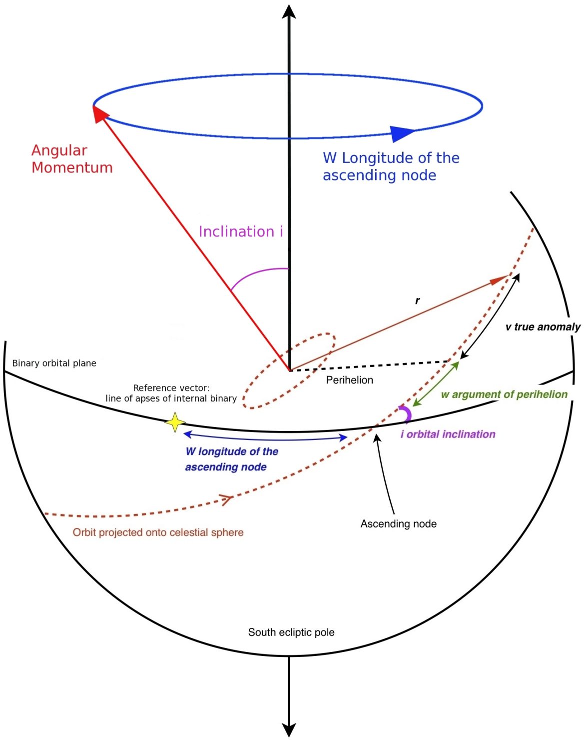

Figure 3.2: The $i - W$ unit sphere

3.6 Previous work

Confirmation that the features of Figure 3.1 are not numerical artefacts comes reports of from similar behaviour in Verrier and Evans (2009). In that work the authors report discovering a counter-play between the Kozai mechanism and a new circumbinary libration whilst modelling orbits within the double binary system HD98800.

Verrier and Evans (2009) used the MOIRAI code (Verrier and Evans, 2007) as their numerical integrator, a symplectic algorithm adapted for hierarchical multiple-component systems. But they also report achieving the same circumbinary behaviour using a standard Bulirsch-Stoer integration scheme Press et al. (1988). The circumbinary libration is therefore not a computational artefact, as it is reproduced in at least three different numerical schemes.

Following on from Verrier and Evans (2009) is the excellent analytic paper of Farago

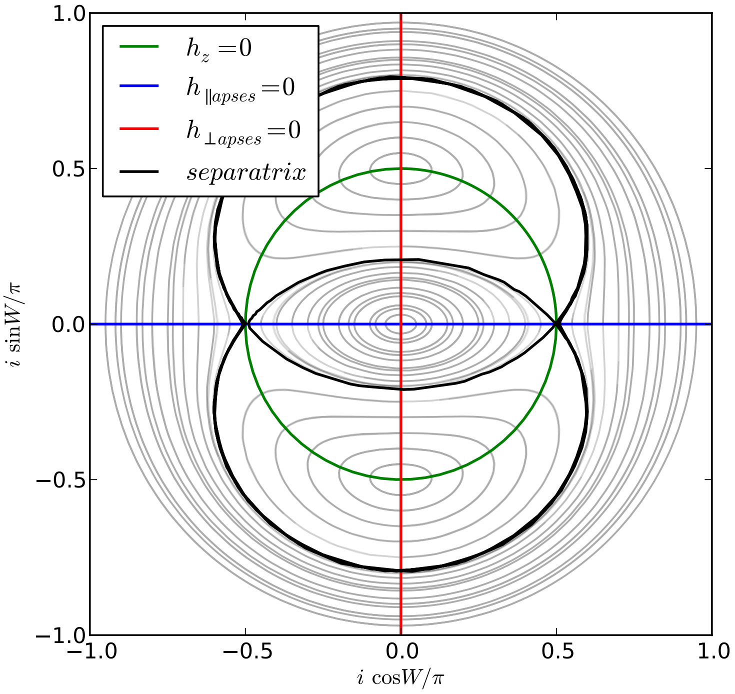

Figure 3.3: The separatrix and symmetries of the $(i \cos W, i \sin W)$ surface of section. h = specific angular momentum.

and Laskar (2010). In this article the authors present a time-averaged Hamiltonian of the elliptically restricted three-body problem in the circumbinary limit. Farago and Laskar (2010) pursue the assumption that the displacement of the circumbinary component from the centre of mass of the system r_3 is significantly greater than the relative separation of the internal binary r_{21}. Under this $r_3 \gg r_{21}$ approximation Farago and Laskar expand the elliptically restricted three body Hamiltonian to second order in r_{21}/r_3 and then average over the orbit of the binary and the third body to obtain a time-averaged quadrupolar Hamiltonian. In the following sections I show that this model proves to be a good fit to our numerical findings.

The time-averaged quadrupolar Hamiltonian of Farago and Laskar (2010) promises to be especially accurate in the regime $r_{21}/r_3 \ll 1$, as the neglected higher order terms in r_{21}/r_3 will tend to zero at a faster rate than those of second order. But this model is not so good for orbits closer to the binary system, where higher order terms play a more substantial role. In § 3.8.1 I investigate the accuracy of Farago and Laskar's model by testing the predictions that it makes, and the limits at which their quadrupolar approximation becomes insufficient.

3.7 Separatrix and critical angle

The separatrix (Figure 3.3: black) is the boundary in phase-space between different modes of behaviour. In our circumbinary surface of section the separatrix takes the form of a triple figure-of-eight, or two circles intersecting at ($W = 0$, $i = \pi/2$) and ($W = \pi$, $i = \pi/2$), dividing the regions of behaviour outlined in § 3.2. The separatrix which we plot in Figure 3.3 is actually the path of one very rare test particle which, due to our stepping integrator, sampled more than one region of behaviour.

In § 3.3 I mentioned that the geometry of the surface of section, and hence the size of the various behavioural regions, is dependent only on binary eccentricity. Here I quantify this statement. We note that each point on the surface of section (Figure 3.1) defines a unique path, and that every path intersects the vertical axis ($W = \pm\pi/2$). We define a critical angle $i_{\rm crit}$ as the inclination i at which the separatrix crosses the positive vertical axis ($W = +\pi/2$) in the region $0 \leq i \leq \pi/2$.

Subsequent to the discussion of symmetry in § 3.5 it follows that the three other intersections of the separatrix with the vertical axis are reflections of the critical angle $i_{\rm crit}$ defined in the region ($W = \pi/2$, $0 \leq i \leq \pi/2$).

3.7.1 Measuring the critical angle

We have run an additional suite of simulations to find and extract the critical angle as a function of binary eccentricity. These simulations were run with one shell of test particles at radius $25a_{\rm b}$, longitude of the ascending node $W = \pi/2$ and with a high resolution in inclination, namely intervals of $\triangle i = \pi/80$, at various values of binary eccentricity.

For each orbit sampled we visually identified the behaviour (§ 3.2) to locate an upper and lower boundary on the separatrix as a function of binary eccentricity. The results are plotted in Figure 3.4 preserving the colour scheme of Figure 3.1. The green, red and blue points in Figure 3.4 represent the behaviour of test particles at these locations. We only plot the sampled points that lie either side of the separatrix.

To provide an analytic expression to describe the position of the separatrix as a function of binary eccentricity we searched for the lowest-order polynomial fit to the data with the constraint that the fit must pass between every pair of green-red points. This fit is given by the fourth-order polynomial:

$$i_{\rm crit} = 0.5 + ae_{\rm b} + be_{\rm b}^2 + ce_{\rm b}^3 + de_{\rm b}^4 \tag{3.1}$$

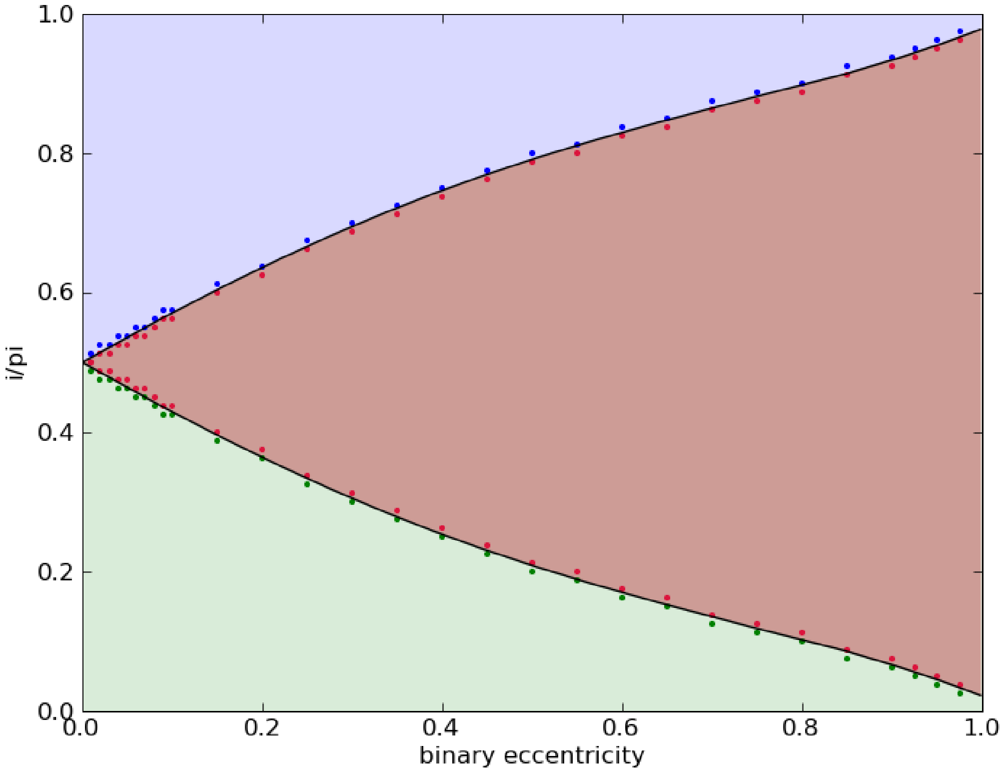

Figure 3.4: Orbital behaviour in the $W = \pi/2$ plane as a function of binary eccentricity.
Green: prograde ($i < \pi/2$)
Blue: retrograde ($i > \pi/2$)
Red: island of libration centred at ($i = \pi/2, W = \pi/2$)

$$a = -0.7138 \pm 0.0023$$

$$b = 0.1021 \pm 0.0030$$

$$c = 0.5264 \pm 0.0038$$

$$d = -0.3942 \pm 0.0047.$$

In all cases the angle of the separatrix in the region ($\pi/2 \leq i_{\mathrm{crit}} \leq \pi$) is at inclination $\pi - i_{\mathrm{crit}}$, as it should be by symmetry arguments.

3.7.2 Comparison with Farago and Laskar (2010)

The time-averaged quadrupolar model of Farago and Laskar (2010) predicts the separatix to lie at points which produce infinities in their calculations. Their equation 2.34 may be rearranged to give the critical angle of

$$i_{\mathrm{crit}} = \arcsin \sqrt{\frac{1 - e_{\mathrm{b}}^2}{1 + 4e_{\mathrm{b}}^2}}. \tag{3.2}$$

Since we measure the critical angle at a radius of $25a_{\mathrm{b}}$ from the binary we expect the quadrupolar approximation to hold, and indeed we find an excellent agreement between our measurements and Equation 3.2. The predicted location of the separatrix lies between every pair of our experimental limiting points.

We plot our data, experimental fit (Equation 3.1), and the Farago and Laskar prediction together in Figure 3.5. There is an exact agreement between model and data at this radius. The largest divergence from our experimental fit is at $e_{\mathrm{b}} \rightarrow 1$, which is an unphysical limit as the binary itself becomes unbound.

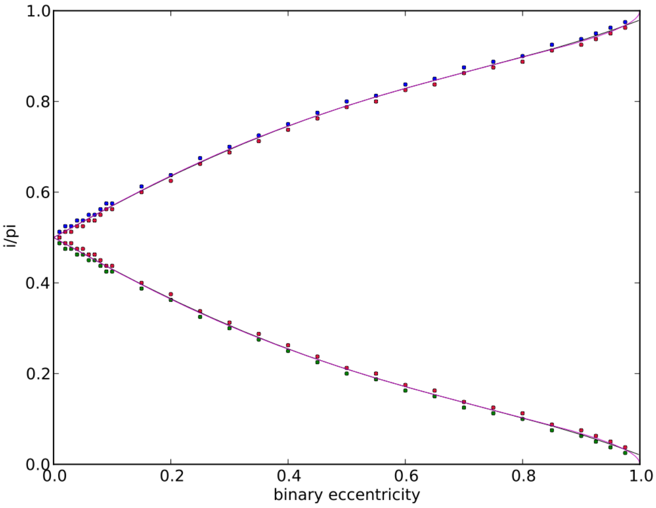

Figure 3.5: Our experimental fit to the critical angle of the separatrix (Eq 3.1) (black) and Farago and Laskar's analytic expression (Eq 3.2) (pink).
Green: prograde ($i < \pi/2$)
Blue: retrograde ($i > \pi/2$)
Red: island of libration centred at ($i = \pi/2, W = \pi/2$)

3.7.3 Automated identification of behaviour

It is possible to automate the process of identifying which behavioural regime that a test particle belongs to. We do this by dividing phase space into quadrants (see Table 3.3) and asking each test particle which regions it visited during a simulation. This is achieved via SQL queries of the database and, provided that the test particle has sampled greater than 50% of its libration, will accurately identify the behaviour. This pipeline was used to experimentally identify the behaviour of all test particles, i.e. see the colouring of Figure 3.1.

Table 3.3: Behavioural identification

behaviour type	$i < \pi/2$	$i > \pi/2$	$W < \pi$	$W > \pi$
prograde	✓	×	✓	✓
polar libration ($W = \pi/2$)	✓	✓	✓	×
polar libration ($W = 3\pi/2$)	✓	✓	×	✓
retrograde	×	✓	✓	✓

3.8 Constant of motion

Verrier and Evans (2009) proposed an integral of motion (see their equation 3) for the libration islands to be the component of the specific angular momentum of an orbit along the line of apses of the internal binary, which may be expressed as

$$h_{\parallel \mathrm{apses}} = h \sin i \sin W. \tag{3.3}$$

This makes intuitive sense as the libration islands are centred at ($i = \pi/2$, $W = \pm\pi/2$), i.e. the points at which a test particle's angular momentum is exactly parallel or antiparallel to the line of apses of the internal binary (see Figure 3.3). So for small deviations from these central points we find that $h_{\parallel \mathrm{apses}}$ is conserved.

Unfortunately this model breaks down as we move out from the centre of libration. In Figure 3.6 (upper panel) we show the Verrier and Evans constant of motion (Equation 3.3) over the course of our integration for example test particles in proximity to the centre of the island of libration ($i = \pi/2$, $W = \pi/2$). These example test particles are from our simulation of binary eccentricity $e_\mathrm{b} = 0.6$ and mass fraction $\alpha_\mathrm{b} = 0.5$. We observe that this suggested constant of motion becomes insufficient for test particles which sample phase space away from the centre of the libration.

A more promising integral of motion is given by the time-averaged quadrupolar model of Farago and Laskar (2010), their equation 2.20, which we translate to orbital elements as

$$h_\mathrm{FL} = \cos^2 i - e_\mathrm{b}^2 \sin^2 i (5 \sin^2 W - 1). \tag{3.4}$$

We see that this equation reduces to the square of Equation 3.3 for values of ($i \to \pi/2$, $W \to \pm\pi/2$) close to the centre of libration. But this model correctly predicts the paths of orbits across the entirety of the surface of section and incorporates the dependence on

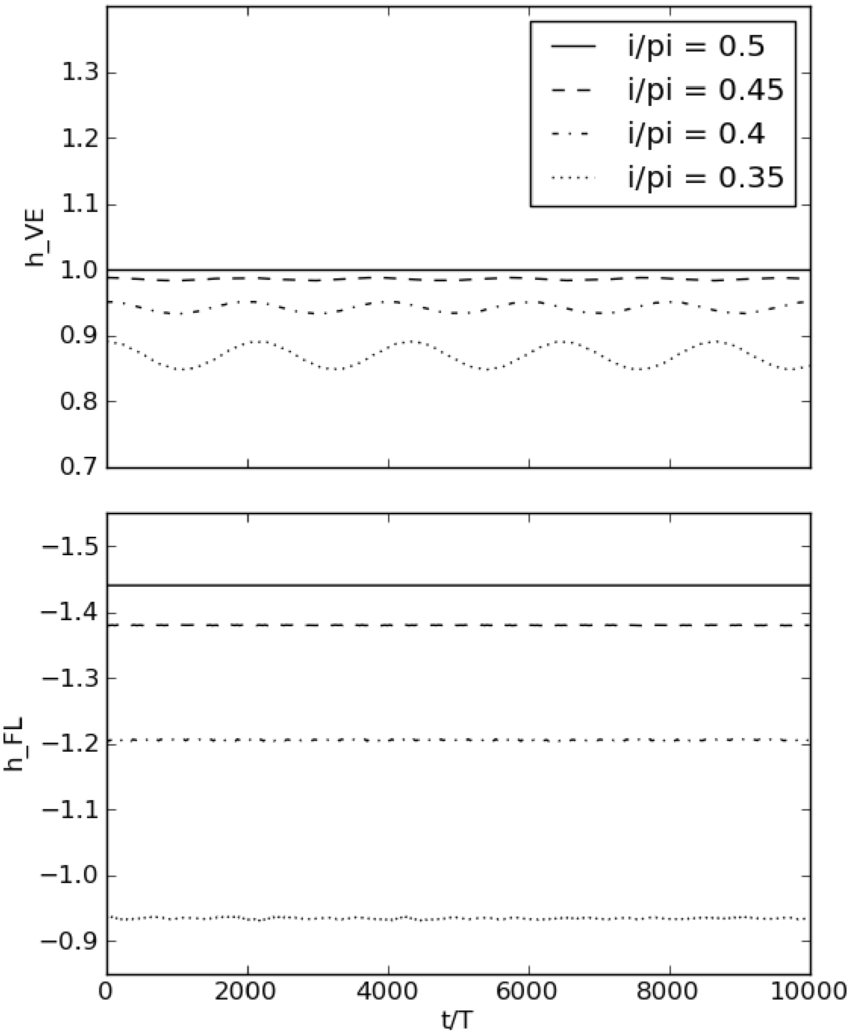

Figure 3.6: A plot of the suggested constants of motion for example test particles in proximity to the centre of the island of libration ($i = \pi/2$, $W = \pi/2$) from our simulation of binary eccentricity $e_\mathrm{b} = 0.6$ and mass fraction $\alpha_\mathrm{b} = 0.5$.
Upper panel: Verrier and Evans (2009) (Eq 3.3).
Lower panel: Farago and Laskar (2010) (Eq 3.4).

binary eccentricity e_b. We plot this constant of motion in the lower panel of Figure 3.6 for the same test particles as in the upper panel.

3.8.1 How constant is the constant of motion?

We use the constant of motion predicted by the time-averaged quadrupolar model of Farago and Laskar (2010) as a test of the limits of the quadrupolar approximation. For each simulated test particle we have 10^3 snapshots over the course of integration. We therefore calculate an instantaneous h_FL for each test particle at each snapshot and ask the question: *"exactly how constant is this constant of motion?"*

For example — in our shell of test particles at radius $50a_\mathrm{b}$ we find that a typical test particle experiences variation in h_FL of $\sim 1.4 \times 10^{-5}$. This is measured by taking the standard deviation σ of the instantaneous measurements of h_FL over the course of a simulation. Since h_FL is of order unity, this equates to a typical error of 0.0014% at these large radii.

Of course, the quadrupolar model should perform well at large radii as the neglected terms tend to zero. But when we consider orbits closer to the binary we begin to probe regions where neglected higher order terms become non-negligible. To do so we plot histograms of $\sigma(h_\mathrm{FL})$ for each shell of test particles sampled (see Table 3.2). In Figure 3.7 I show the histograms for the shells of test particles at radii 3, 4, 5 and $6a_\mathrm{b}$. These plots are also coloured according to binary eccentricity e_b.

As we consider orbits closer to the binary ($a < 10a_\mathrm{b}$), we see that the quadrupolar approximation begins to break down. At $6a_\mathrm{b}$ most orbits are accurate to the quadrupolar model to better than 0.5%, but as we move in to closer than $3a_\mathrm{b}$ some test particles experience deviations of $> 1\%$.

We also note that orbits around binary systems of higher eccentricity (Figure 3.7: purple) deviate significantly more than those around circular binaries (Figure 3.7: light

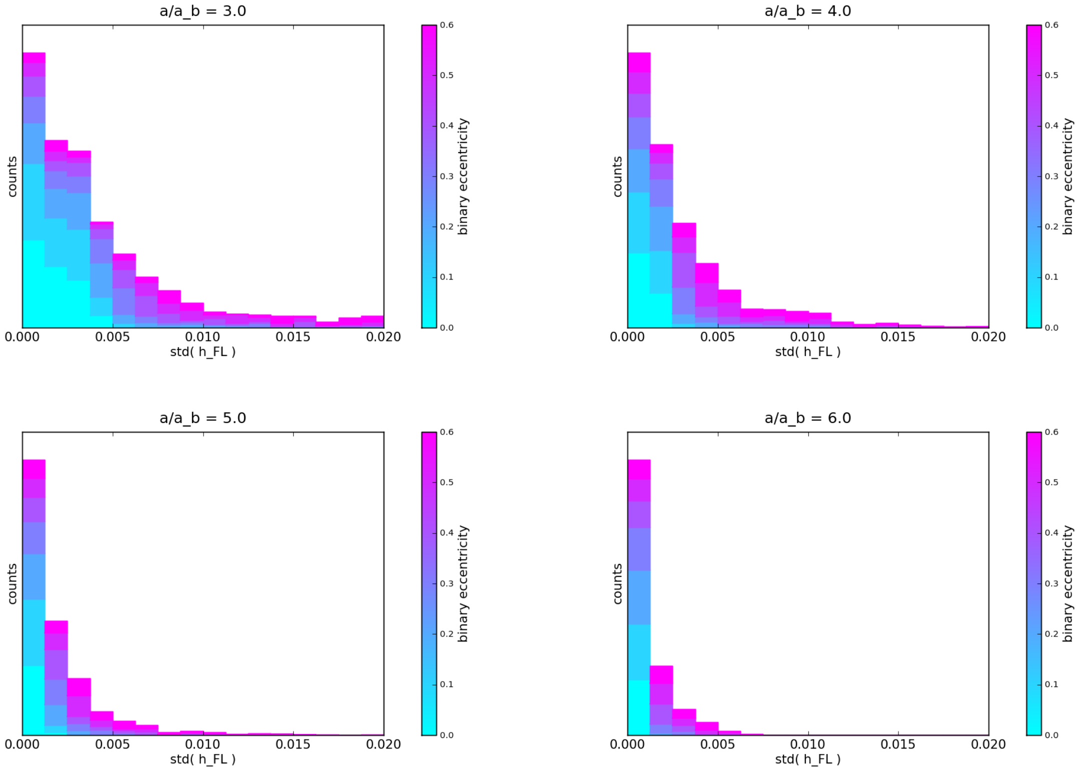

Figure 3.7: Histograms of $\sigma(h_{\mathrm{FL}})$ for radii 3, 4, 5 and $6a_{\mathrm{b}}$, coloured according to binary eccentricity e_{b}.

blue), which indicates that the higher order terms of Farago and Laskar's Hamiltonian have a greater dependence on binary eccentricity.

3.8.2 Significance of $\sigma(h_{\mathrm{FL}})$

In Figure 3.8 we examine the instantaneous measurements of h_{FL} in four typical test particles. These are selected from a random sample of 1000 such plots of test particles from the $3a_{\mathrm{b}}$ radius bin (Figure 3.7, upper-left panel).

Numerical noise from a stepping integrator could in principle accumulate over time. In Figure 3.8 we show that the variation in h_{FL} is present from the start and constant in magnitude over the duration of a simulation. Values of $\sigma(h_{\mathrm{FL}})$ are therefore not biased by an accumulation of numerical noise towards the end of the simulation.

This absence of bias is additionally supported by the appearance of tentative structure in Figure 3.8, most prominently in the lowest panel, which is further evidence of the genuine physical effect of higher order terms than those present in the quadrupolar Hamiltonian of Farago and Laskar (2010).

3.9 Period of precession

From our finely time-sampled $\triangle t = 10T_{\mathrm{b}}$ data (Table 3.2) we extract a period P for the precession of each stable test particle. These range from as little as $50T_{\mathrm{b}}$ (or $5 \times \triangle t$) to greater than the simulation duration, but good fits are obtained for the vast majority.

In Figure 3.9 we plot test particle traces on the $(i \cos W, i \sin W)$ surface of section for our simulation of binary eccentricity $e_{\mathrm{b}} = 0.5$ and binary mass fraction $\alpha_{\mathrm{b}} = 0.5$, as a function of test particle radius a/a_{b}, colouring the traces by precession period.

We observe that the period of precession P is correlated with a test particle's orbital radius and proximity to a separatrix. Orbits which appear to be missing from Figure 3.9

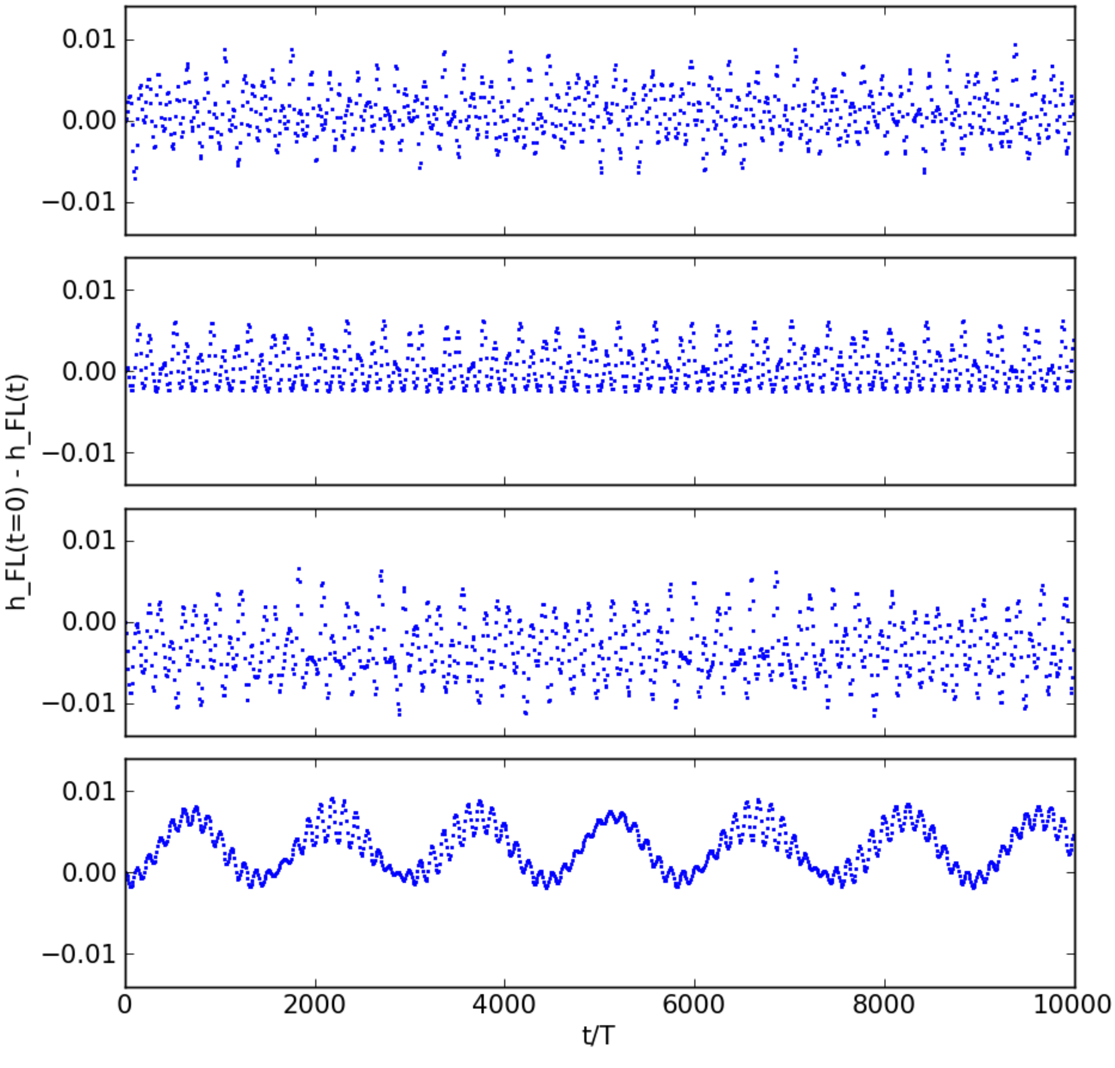

Figure 3.8: A plot of the variation in $h_{\rm FL}$ as a function of time, showing typical test particles from the radius $3a_{\rm b}$ bin.

have been rejected as unstable, and hence are not plotted. The subject of circumbinary stability is explored in detail in Chapter 4.

3.9.1 $P \propto a^n$

As discussed above and demonstrated by Figure 3.9 the closer a circumbinary test particle orbits to the binary system, the shorter is its period of precession P. We find that a powerlaw provides a very good fit to P as a function of distance from the binary, and so we fit $P \propto a^n$ to all orbits sampled, where n is a free parameter. An example fit is shown in Figure 3.10. The data point from our simulation at radius $50a_{\mathrm{b}}$ provides an excellent constraint.

Our data show a tight clustering about $n = 3.5$, as plotted in Figure 3.11. This is not within the range given by Verrier and Evans (2009) of $n = 3.37 \pm 0.06$, but does agree with the time-averaged quadrupolar model of Farago and Laskar which predicts n of exactly 3.5.

But on closer inspection of Figure 3.11 we notice that $P \propto a^n$ appears to consist of two populations. One of these populations is comprised of the prograde and retrograde orbits, which cluster around $n = 3.53$, and the other corresponds to the polar orbits, which cluster around $n = 3.47$.

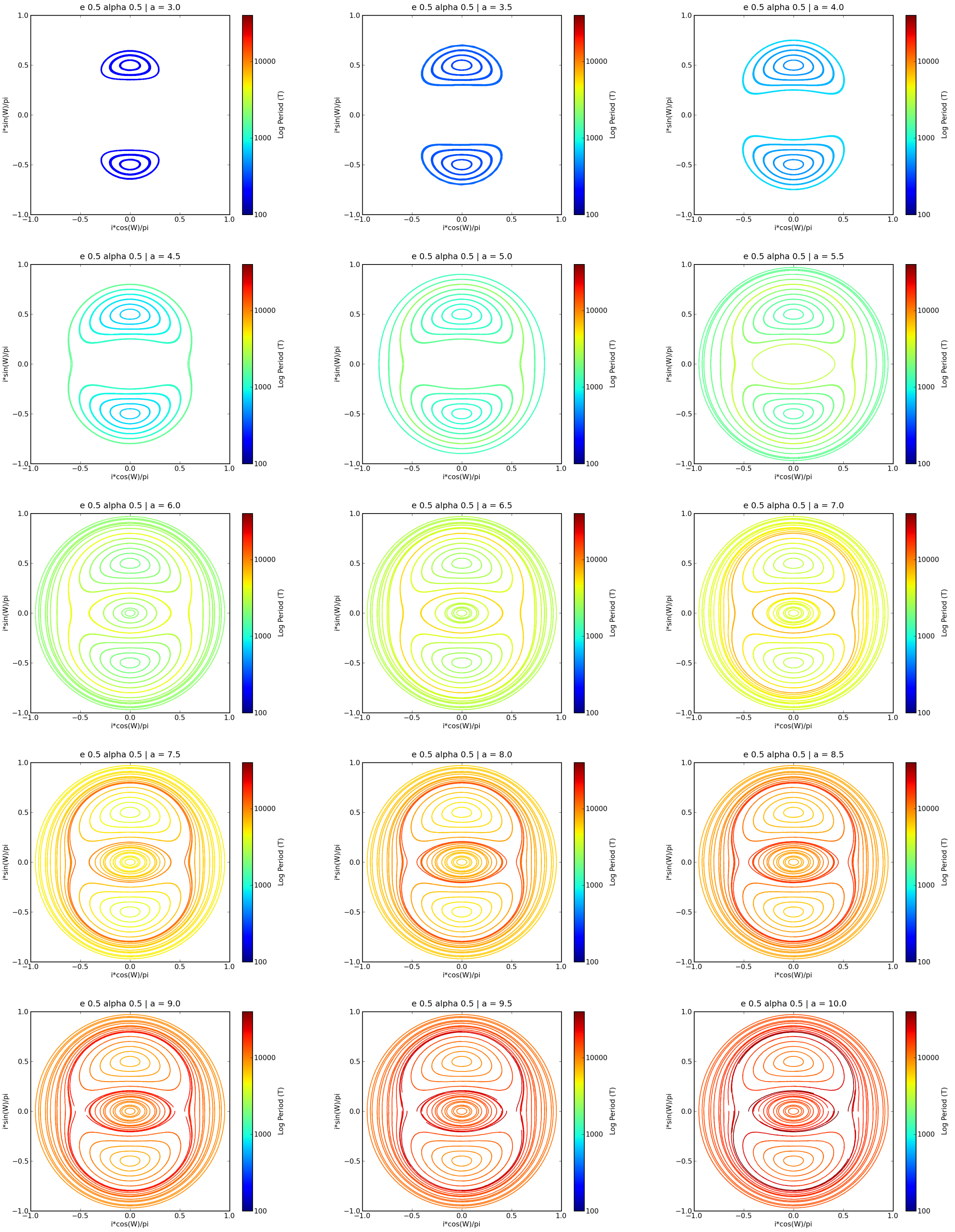

Figure 3.9: The $(i \cos W, i \sin W)$ surface of section for circumbinary orbits about a binary system of eccentricity $e_{\rm b} = 0.5$ and mass fraction $\alpha_{\rm b} = 0.5$ at varius radii (scaled by binary semi-major axis $a_{\rm b}$). Each track is coloured by the logarithm of precession period in units of binary orbital period $T_{\rm b}$.

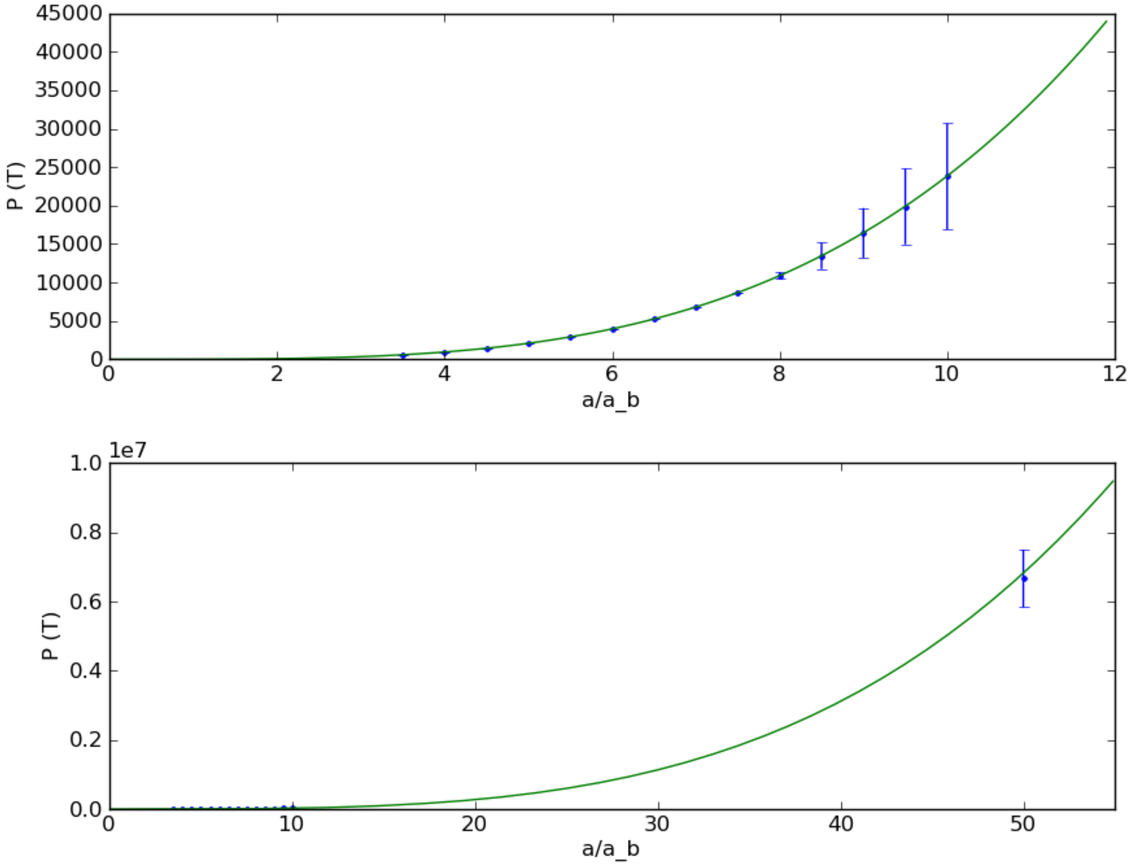

Figure 3.10: An example fit of $P \propto a^n$. This is for a prograde orbit of inclination $i = \pi/4$ about a binary of eccentricity $e_\mathrm{b} = 0$ and mass fraction $\alpha_\mathrm{b} = 0.5$. Plotted is precession period P (in units of binary orbital period T_b) vs test particle semi-major axis a (in units of binary semi-major axis a_b).

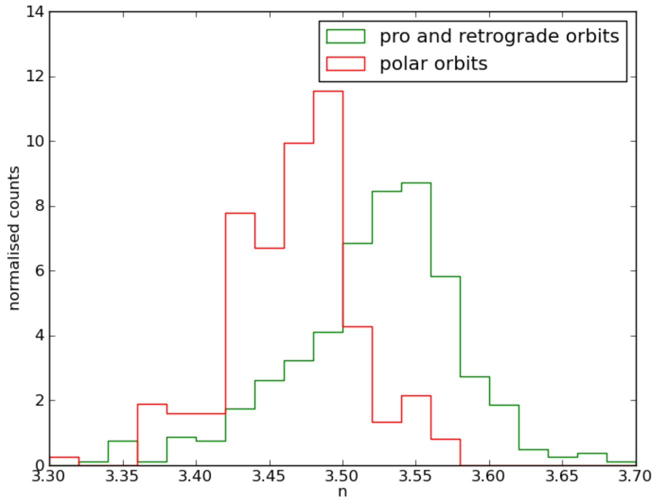

Figure 3.11: A histogram of fitted n in $P \propto a^n$ showing two distinct populations: the polar orbits and the pro/retrograde orbits.

3.9.2 An analytic expression for period of precession

The time-averaged quadrupolar model of Farago and Laskar (2010) makes the following prediction (their equation 2.32):

$$\frac{P}{T_{\mathrm{b}}} = \frac{8}{3\pi}\frac{1}{\alpha_{\mathrm{b}}(1-\alpha_{\mathrm{b}})}\left(\frac{a}{a_{\mathrm{b}}}\right)^{7/2}\frac{F(k^2)(1-e^2)^2}{\sqrt{(1-e_{\mathrm{b}}^2)(h+4e_{\mathrm{b}}^2)}}, \tag{3.5}$$

where $h = h_{\mathrm{FL}}$ as defined in Equation 3.4,

$$k^2 = \frac{5e_{\mathrm{b}}^2}{1-e_{\mathrm{b}}^2}\frac{1-h}{h+4e_{\mathrm{b}}^2}. \tag{3.6}$$

The function $F(k^2)$ is given by Farago and Laskar (2010) in terms of complete and incomplete elliptical integrals of the first kind. But a substitution of equation 17.4.15 from Abramowitz (1964) for the incomplete integral allows us to define $F(k^2)$ in terms of the complete elliptical integral of the first kind $K(k^2)$ alone.

$$F(k^2) = \begin{cases} K(k^2) & \text{where } k^2 < 1 \\ k^{-1}K(k^{-2}) & \text{where } k^2 > 1 \end{cases} \tag{3.7}$$

$$K(k^2) = \int_0^{\pi/2} \frac{d\theta}{\sqrt{1-k^2\sin^2\theta}}. \tag{3.8}$$

The limiting case of $k^2 = 1$ at points of $h_{\mathrm{FL}} = e_{\mathrm{b}}^2$ gives a non-finite period. These points therefore define the location of the separatrix thusly:

$$h_{\mathrm{FL}} = \cos^2 i - e_{\mathrm{b}}^2\sin^2 i(5\sin^2 W - 1) = e_{\mathrm{b}}^2. \tag{3.9}$$

We calculate the expected period (Equation 3.5) for each test particle that we sample, and in Figure 3.12 we plot a straight one-to-one comparison between the predicted and measured periods of precession.

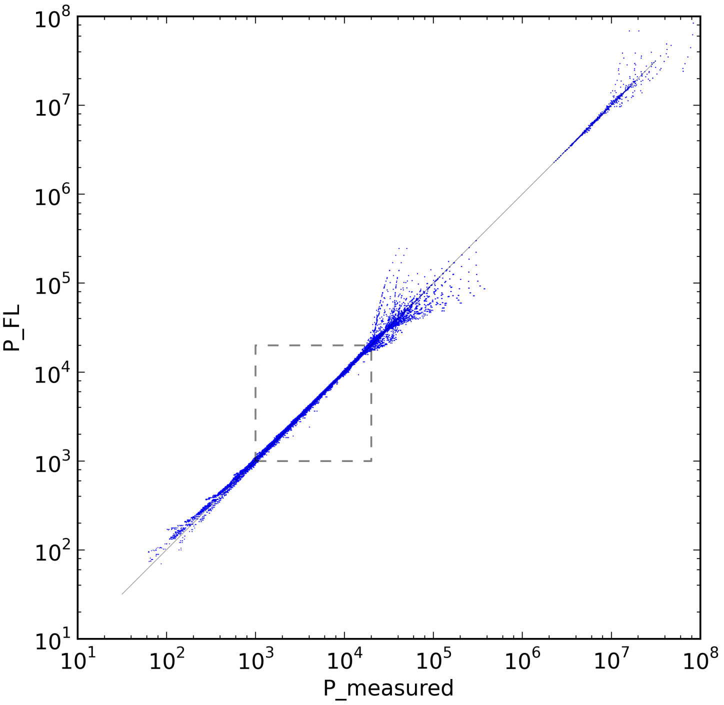

Figure 3.12: A plot of precession period P in units of binary orbital period T_{b}: measured vs predicted (Farago and Laskar, 2010) for all particles in our simulation.

Figure 3.12 shows two populations — the small upper right group consists of test particles from our radius $50a_\mathrm{b}$ simulations (hence larger precession periods), whereas the larger group in the centre and lower left represents every test particle from the main body of our simulations ($1.5a_\mathrm{b} \leq a \leq 10a_\mathrm{b}$, summarised in Table 3.2).

The scatter in period at the upper end of both groups of Figure 3.12 is due to these periods being significantly greater than the duration of the simulation, and hence badly fitted. The scatter at low periods ($P \lesssim 10^3 T_\mathrm{b}$) is due to real deviations of the measured periods from the quadrupolar model at low radii.

But to demonstrate the level of agreement between our numerical experiments and the time-averaged quadrupolar model of Farago and Laskar (2010) we calculate statistics from the well behaved boxed region of Figure 3.12 ($10^3 T_\mathrm{b} \leq P \leq 2 \times 10^4 T_\mathrm{b}$), showing a 1:1 correlation to around 3%:

$$P_\mathrm{FL}/P_\mathrm{measured} = 1.008 \pm 0.029.$$

3.10 Conclusions

Circumbinary phase space in the elliptically-restricted three-body problem has a rich structure. A nodal libration mechanism produces three distinct families of behaviour: close-to-coplanar prograde ($i \sim 0$) and retrograde ($i \sim \pi$) orbits which precess in the longitude of the ascending node, whilst close-to-polar orbits ($i \sim \pi/2$ and $W \sim \pm\pi/2$) have their longitude of the ascending node and inclination coupled to precess about the centre of an island of libration.

The analytic time-averaged quadrupolar model of Farago and Laskar (2010) provides an excellent description of the behaviours of circumbinary orbits at radii $\geq 50a_\mathrm{b}$. We have also shown that their model becomes inaccurate to greater than 1% at orbital radii $\leq 5a_\mathrm{b}$, and especially in cases of high binary eccentricity.

Chapter 4

Stability of Circumbinary Orbits

The work presented in this chapter is based on Doolin and Blundell (2011).

4.1 Introduction

In Chapter 3 I explored the dynamics of a circumbinary nodal libration mechanism in the elliptically restricted three-body problem. The time-averaged quadrupolar model of Farago and Laskar (2010) was shown to fit the behaviour of circumbinary test particles orbiting at large distances from a central binary system. But their model can make no attempt to discern whether these orbits are actually viable.

In this chapter I explore the long-term feasibility of circumbinary orbits with the first dynamically aware analysis of circumbinary orbital stability. In the following analysis I reveal characteristics which are due to resonances between the binary and test particle orbital periods which the Farago and Laskar model cannot explain due to the time-averaging carried out in their derivation.

4.2 Previous work

Many studies of orbital stability in binary systems have focused on “S-type”, or circumstellar, orbits. This is the case whereby a planet (or other structure) directly orbits one star of a binary system, with the secondary star being a distant component. And indeed of the exoplanets known to exist in binary systems to date the circumstellar planets greatly outnumber the circumbinary.

In this chapter I consider “P-type”, or circumbinary, orbital stability. This regime is underexplored in observational campaigns and yet in the following sections I show that it is a promising place to search for exoplanets.

Previous work on the stability of circumbinary orbits has taken the form of both analytic and numerical analysis. Szebehely (1980) and Szebehely and McKenzie (1981) investigated analytic stability in circular binaries as a function of binary mass fraction for both circumstellar and circumbinary orbits. Their results formed the basis of comparison for the early numerical studies such as Dvorak (1984), who integrated 300 test particles around binaries of varying eccentricity.

As computational power has increased over the past 30 years, authors have expanded on these early numerical works by considering more test particles and sampling a wider range of binary parameter space (Dvorak et al., 1989; Holman and Wiegert, 1999; Pilat-Lohinger et al., 2002; Musielak et al., 2005). These publications consider various regimes of the coplanar elliptically restricted 3-body problem, but none has strived to relax the coplanar constraint.

4.2.1 Inclined stability

The only previous study of inclined circumbinary stability is found in Pilat-Lohinger et al. (2003). Here the authors performed three dimensional numerical experiments but they were not aware of the circumbinary libration mechanism (Chapter 3). The simulations of Pilat-Lohinger et al. (2003) contained only test particles of initial longitude of the ascending node $W = 0$ (Pilat-Lohinger, private communication). As such they did not sample any of the polar librating orbits, as these do not intersect the $W = 0$ or $W = \pi$ axes (Figure 3.1). Pilat-Lohinger et al. also restricted themselves to a limited region of phase-space, considering only prograde inclinations of up to 50° and systems of equal mass fraction ($\alpha_\mathrm{b} = 0.5$).

4.2.2 Derived concepts

Of the many studies mentioned above the general aim has been to attempt to divide phase-space into three regions:

1. an inner (small radii) completely unstable region where all test particles are accreted or ejected from the system.
2. an intermediate quasi-stable region where some test particles are stable but others are not.
3. an outer (large radii) stable region where all test particles are stable.

Analytic functions are fitted to the boundaries between these regions, known as the lower and upper critical orbits respectively (see Dvorak et al., 1989). In studies of circumbinary structures, generally the upper critical orbit is taken to define the innermost stable orbit, and as such the inner edge, or “disk gap” of a circumbinary disk (Blundell et al., 2008).

Table 4.1: Sampling of circumbinary phase space.
a_b = binary semi-major axis and T_b = binary orbital period.

Orbital Element	min	max	$\triangle$
semi-major axis a	$\leq 1.5a_\mathrm{b}$	$\geq 5a_\mathrm{b}$	$0.05a_\mathrm{b}$
inclination i	0	π	$\pi/80$
longt. of the asc. node W	$\pi/2$	$\pi/2$	–
true anomaly v	0	2π	$\pi/3$
sim. length and snapshot $\triangle t$		$5 \times 10^4 T_\mathrm{b}$	$200T_\mathrm{b}$

4.3 Suite of simulations

I ran a suite of simulations to investigate the long-term stability of circumbinary orbits. As discussed in § 3.7 the dynamics of the circumbinary phase space are such that every orbit crosses the $W = \pm\pi/2$ axis and there exists a symmetry which reflects $W = +\pi/2$ onto $W = -\pi/2$. We may therefore narrow down the region of phase space which we sample to only one value of the longitude of the ascending node, $W = +\pi/2$.

I ran these simulations to 5×10^4 binary orbital periods, considering some 2 million test particles in total, to achieve a detailed sampling of phase space, especially in orbital radius a and inclination i. The circumbinary phase space sampling is laid out in Table 4.1.

This suite of simulations consists of 35 separate numerical experiments, equivalent to those discussed in Chapter 3. Each simulation considers a synthetic binary system of prescribed eccentricity and mass-fraction as laid out in Table 3.1.

4.4 A measure of stability

As discussed in § 2.6.1, each test particle is monitored during integration for instability. Unstable orbits are identified and removed during integration where:

1. A test particle is perturbed sufficiently from its initial orbit to approach either star

too closely, i.e. to within it's region of gravitational influence (Hill radius).

2. A test particle receives a gravitational kick and evolves onto an unbound trajectory. In orbital elements about the centre of mass this equates to a condition on test particle eccentricity $e > 1$. Whilst in the full three-body system this is strictly valid only at large radii, we consider such a condition to be indicative of circumbinary instability at all radii.

Post-simulation stability criteria are applied to identify and reject test particles which approach but do not quite reach escape velocity.

Whereas in Chapter 3 we were concerned with test particles which survived the simulation, here we are more interested in those which don't. In Figure 4.1 I plot a histogram of the escape times t_{escape} at which particles are rejected from the simulation. The vast majority of unstable particles are identified at the start of the simulation — of the approximately half a million unstable test particles, over half of these are caught within the first 1000 binary orbital periods, with the distribution tailing off steeply even in log-space.

Since we sample each orbit from multiple initial values of the true anomaly v (Table 3.2) we measure an orbit's long-term stability by the fraction of initial test particles which survive the simulated duration of $5 \times 10^4 T_{\mathrm{b}}$.

In Figure 4.2 I show a plot of this measure of stability across the entire sampled parameter space. The major axes of this figure correspond to the simulation parameters of binary eccentricity and mass fraction, whilst the minor axes correspond to orbital radius and inclination. This is a density plot where each pixel represents a sampled orbit, and the transparency to our measure of stability — a darker colour indicates a more stable orbit. For consistency the orbital behaviour colour scheme of Chapter 3 is maintained.

Previous investigations of circumbinary stability have attempted to fit analytic functions to the boundary of the innermost stable orbit (§ 4.2.2), but we find such a rich and

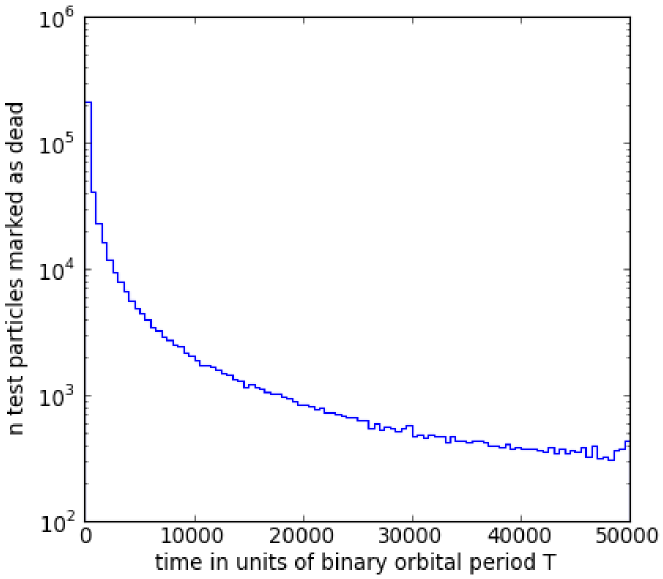

Figure 4.1: A histogram of the escape time $t_{\rm escape}$ for particles which sample unstable orbits.

complex structure in stability across inclined phase space that such a reduction is inappropriate. As such I present a complete view of the data in its final form in Figure 4.2. The following features are qualitatively highlighted:

1. First, and broadly speaking, orbits are more stable at lower binary eccentricity $e_{\rm b}$.
2. With equal generality, retrograde orbits (blue) appear to be the most stable, followed by librating orbits (red) and prograde orbits (green). The difference in radius of the innermost stable orbit across inclination can be larger than $1a_{\rm b}$.
3. There are vertical striations of instability, most noticeable in the higher eccentricity simulations $e_{\rm b} \geq 0.5$, and predominantly at coplanar inclinations of $i \sim 0$ and $i \sim \pi/2$. These regions of instability are due to orbital resonances between the orbital period of a test particle and the orbital period of the central binary.
4. We note very thin horizontal *pinnacles* of instability in non-librating orbits $0.2 \leq$

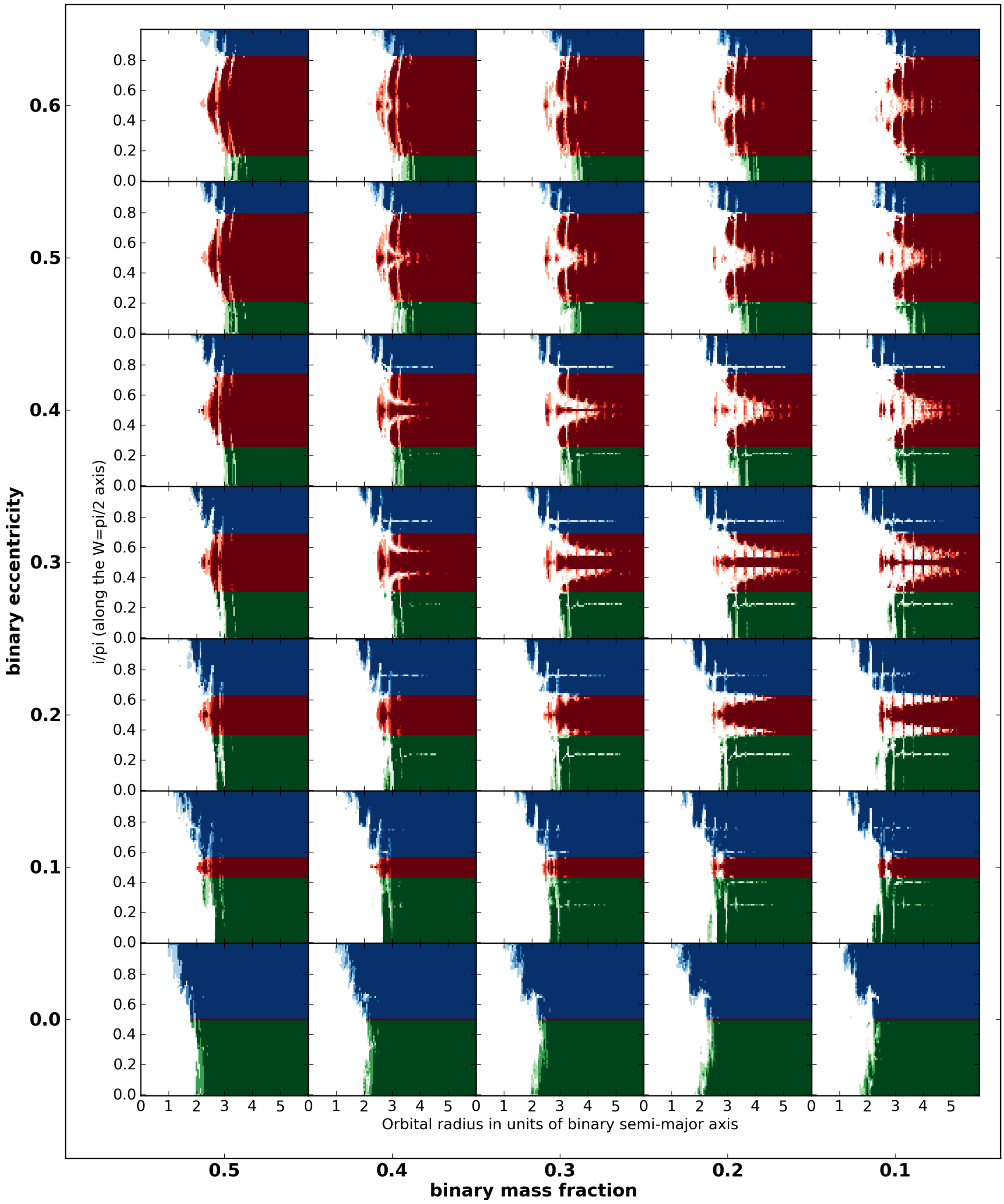

Figure 4.2: Orbital stability plotted as a function radius a/a_b and inclination i on the $W = \pi/2$ axis, across binary eccentricity — mass fraction parameter space. Colours:
Green: prograde ($i < \pi/2$)
Blue: retrograde ($i > \pi/2$)
Red: island of libration centred at ($i = \pi/2, W = \pi/2$)

$e_{\mathrm{b}} \leq 0.4$. These pinnacles are located at inclinations $i \approx \pi/4$ and $i \approx 3\pi/4$, and extend up to $3a_{\mathrm{b}}$ into otherwise stable phase space.

5. More central to the pinnacles discussed above are wider *peninsulas* of instability in the librating region. These appear symmetrically either side of $i = \pi/2$ in the librating region for simulations of $e_{\mathrm{b}} \geq 0.2$ and converge upon each other as $e_{\mathrm{b}} \to 0.6$.
6. The horizontal pinnacles and peninsulas are a function of binary mass fraction α_{b}. These features do not appear in the $\alpha_{\mathrm{b}} = 0.5$ simulations, and are magnified towards increasingly extreme values of α_{b}.

4.4.1 Escape time

In a companion figure to the stability plot of Figure 4.2 I show the escape time of each unstable orbit in Figure 4.3. Here we use the same axes as Figure 4.2 — with major axes corresponding to the simulation parameters of binary eccentricity and mass fraction, and minor axes corresponding to orbital radius and inclination. This is a density plot where each pixel corresponds to an orbit sampled, and the transparency to the inverse of escape time $1/t_{\mathrm{escape}}$ — a darker colour indicates a longer surviving orbit. Since we consider multiple test particles per sampled orbit we take an average for the escape time and do not plot completely stable orbits. We again preserve the colour scheme of Figure 3.1.

In Figure 4.3 we find matching features to those in Figure 4.2, as described in § 4.4. But here we can also observe how long-lived the unstable orbits are. For example, in the low binary eccentricity simulations ($e_{\mathrm{b}} < 0.2$) we find that orbits are either very quickly unstable, or definitely stable. But for the simulations of higher binary eccentricity e_{b} and more imbalanced binary mass fraction α_{b}, the most striking features are long-lived. The test particles which sample phase space at these extreme points are *almost* stable, and survive for times of order the simulated duration $\sim 50,000 T_{\mathrm{b}}$ (Table 4.1).

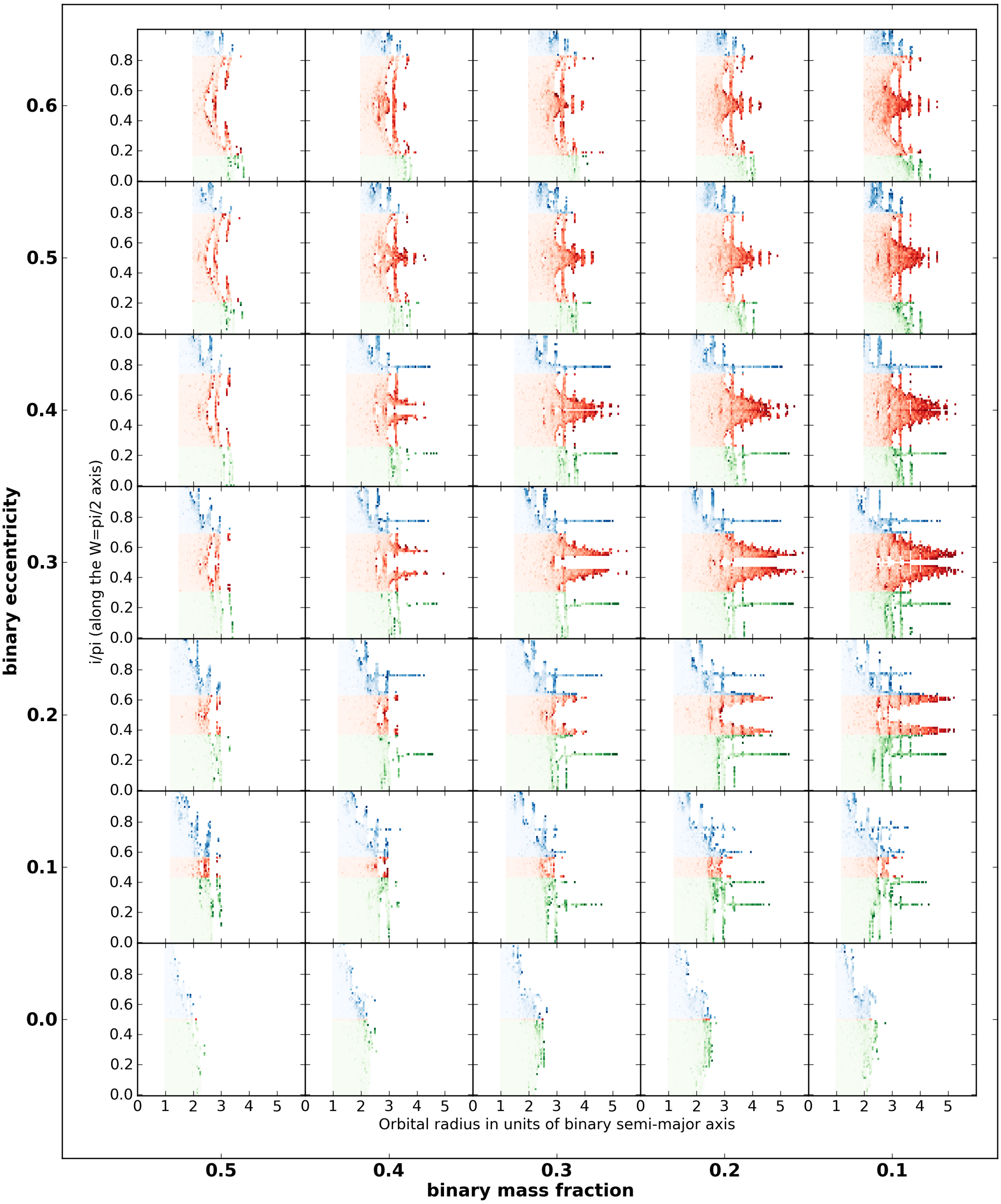

Figure 4.3: Inverse escape time $1/t_{\text{escape}}$ as a function of radius a/a_{b} and inclination i on the $W = \pi/2$ axis, across binary eccentricity — mass fraction parameter space. Colours:
Green: prograde ($i < \pi/2$)
Blue: retrograde ($i > \pi/2$)
Red: island of libration centred at ($i = \pi/2, W = \pi/2$)

Test particles on unstable orbits further inside the unstable region (closer to the binary) are quickly accreted onto the binary stars and/or ejected from the system. It is within this region of instability that inflows and outflows corresponding to mass loss are likely to be important.

4.5 Discussion

The phase space underlying our study of stability within the three-body problem is arguably significantly chaotic. It is likely that further phase-space structure exists in regions near the separatrix when one considers additional terms in the expanded Hamiltonian. However, these terms are higher order corrections, and so we believe that the features reported here are real and significant to the consideration of matter around binaries, but we advise caution before cranking up the phase-space resolution any further. The model which we have investigated here is idealised, and hence unphysical when examined in detail. Perturbations should be considered such as the finite volume of the bodies considered and the feedback effect on the internal binary of a third body of non-negligible mass.

4.5.1 Circumbinary Disks

There are many examples in the literature of circumbinary disks. These are observed around young binaries as remnants of the system's protostellar disk (Monin et al., 2007), or around evolved binaries as relics of a phase of mass outflow (Deroo, 2007). In Figure 4.4 I show an image of a circumbinary disk around the pre-main-sequence binary GG Tau A (McCabe et al., 2002). The central binary has been modelled as a point spread function (PSF) and subtracted, leaving the circumbinary disk clearly visible, scattering $\sim 1.5\%$ of the stellar flux.

4.5.2 Circumbinary Planets

The formation of planets in and around binary systems may be hindered by multi-stellar gravitational perturbations (Artymowicz and Lubow, 1994). But as discussed above, young binary systems often possess circumstellar and/or circumbinary disks (Monin et al., 2007), which may provide the seeds for planetary formation (Haghighipour, 2010).

The regime of circumbinary planets has yet to be targeted observationally. Until recently circumbinary planets had only been inferred indirectly, mainly via timing and radial velocity measurements of the stellar components of binary systems (e.g. Lee et al., 2009; Beuermann et al., 2011; Qian et al., 2011), although studies of the feasibility to detect such planets directly had been undertaken (Schwarz et al., 2011).

Recently Doyle et al. (2011) presented the first direct evidence for a circumbinary planet in the binary star system Kepler-16. This evidence takes the form of multiple transits of a circumbinary planet across each of the stellar components of Kepler-16, visible in the system's light curve observed with NASA's Kepler spacecraft. The circumbinary planet Kepler-16b orbits coplanar to its host binary system, and at a radius of $3.147a_{\mathrm{b}}$, comfortably within the stable region of phase space.

4.6 Conclusions

The results presented here provide a map of the regions of circumbinary phase space where we may find long-lived structures, such as disks or planets. We should not presume any given binary system to lack a circumbinary component unless otherwise demonstrated. Such a component may be a source of obscuration, emission, inflow or outflow.

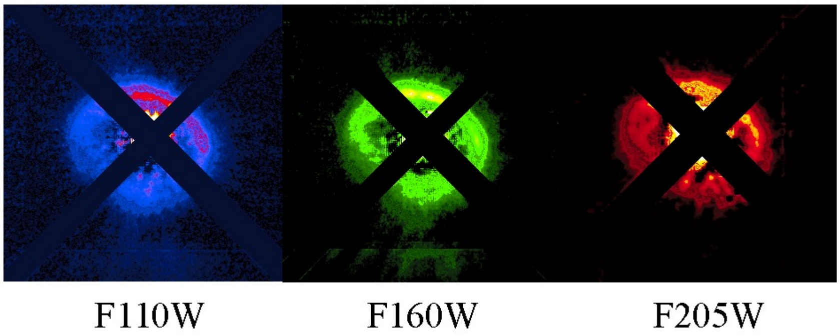

Figure 4.4: Hubble Space Telescope NICMOS near-infrared images of the GG Tau A circumbinary disk in the J, H and K bands, reproduced from McCabe et al. (2002), their figure 1. The central binary has been PSF-subtracted and regions containing instrumental diffraction spikes are masked.

Chapter 5

Anatomy of a Microquasar

5.1 Microquasars

Microquasars are a special sub-group of binary stars. These are close binary systems where two stellar components orbit each other in close enough proximity to interact. Microquasars belong to a broader class of objects known as X-ray binaries, where one of the binary components has evolved to become a compact object, such as a white dwarf, neutron star or black hole. The compact object accretes matter from the second “donor” star onto itself.

In high mass X-ray binaries (HMXB) the donor star is massive and hot, and emits a strong radiation pressure driven stellar wind. This stellar wind provides the mechanism for mass transfer to the compact object.

In low mass X-ray binaries (LMXB) the donor star is less massive but fills its Roche lobe (§ 5.1.1) and overflows its gravitational bounds. This mechanism provides a high rate of mass transfer as the outer layers of the donor star are stripped away by its compact companion.

5.1.1 The Roche potential and Lagrange points of a circular binary

It is informative to examine the gravitational potential in a binary system. We consider a circular binary ($e_{\mathrm{b}} = 0$) with stars of masses M_1 and M_2 located at positions $\mathbf{r}_1$ and $\mathbf{r}_2$ in the xy plane. In a frame of reference co-rotating with the binary the angular velocity vector $\boldsymbol{\Omega}$ is given by Equation 2.7 and is directed out of the plane of the binary along $\hat{z}$,

$$\Omega^2 = \frac{G(M_1 + M_2)}{a^3}. \tag{5.1}$$

The co-rotating potential Φ at some point $\mathbf{r}$ is given by the equation

$$\Phi(\mathbf{r}) = -\frac{GM_1}{|\mathbf{r}_1 - \mathbf{r}|} - \frac{GM_2}{|\mathbf{r}_2 - \mathbf{r}|} - \frac{1}{2}(\boldsymbol{\Omega} \times \mathbf{r})^2, \tag{5.2}$$

where the third term accounts for centrifugal acceleration in the rotating frame. The Coriolis force is not apparent in Equation 5.2 as it cannot be represented by a scalar potential, but for motions within the rotating coordinate frame it does exert an influence. Equipotentials of Equation 5.2 in the xy plane are plotted in Figure 5.1 for a binary of mass fraction $\alpha_{\mathrm{b}} = 0.3$.

At small distances from each star the potential behaves roughly spherically, but at larger distances the equipotential lines distort towards the companion. The Roche lobe is shown by the darker "∞-like" equipotential in Figure 5.1, which defines the maximum radius of gravitational influence of each star. The point at which the Roche lobes meet is known as Lagrange-1 or "L1", which is generally not co-located with the centre of mass.

When the donor star in a LMXB fills its Roche lobe it is clear from Figure 5.1 that excess material will overflow across the L1 point and down onto the surface of the other star.

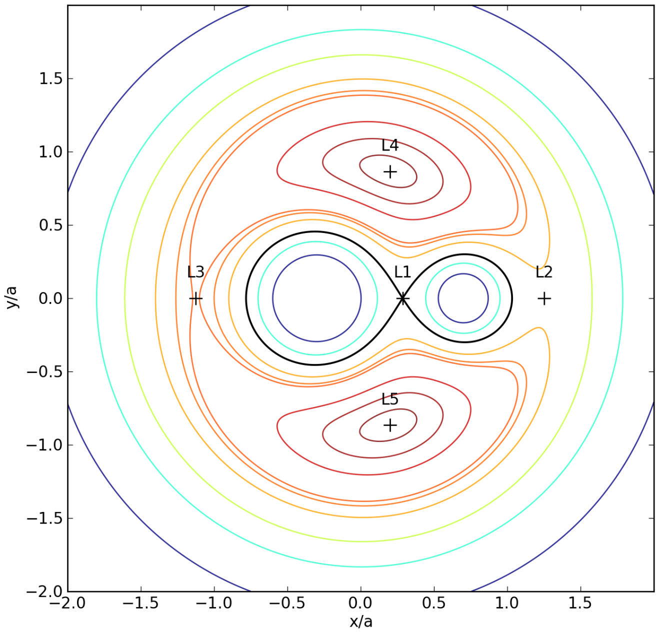

Figure 5.1: The Roche potential and Lagrange points in the binary orbital plane.

Also shown in Figure 5.1 are the other four Lagrange points. The Lagrange points are stationary points of the potential $\nabla\Phi = 0$, where the gravitational attraction of the two stars M_1 and M_2 is precisely balanced by the centripetal force of the rotating frame. At these points a third body of negligible mass can co-orbit with the binary. The points L1, L2 and L3 are unstable, meaning that a perturbed body will experience a net force away from the point of equilibrium. However, L4 and L5 are points of stable equilibria, and as such we observe several thousand "Trojan" asteroids resident here in the Sun-Jupiter system.

5.1.2 Accretion Disk

The accretion at the heart of X-ray binaries releases massive amounts of energy. For comparison — nuclear fusion of Hydrogen to Helium which fuels stars during the first stage of their lifetime has an efficiency of $\sim 0.7\%$, equating to an energy release of 0.7% of rest mass. But accretion onto compact objects can release energy with an efficiency $> 10\%$ of rest mass, theoretically as high as 40%. Accretion is therefore the most efficient energy-releasing astrophysical process.

For matter is to accrete inwards towards the compact object it must lose both gravitational energy and angular momentum. Since angular momentum is a conserved quantity, an accretion disk forms to transport angular momentum outwards, permitting efficient accretion (Shakura and Sunyaev, 1973). Accretion disks around solar mass compact objects produce high energy photons after which X-ray binaries are eponymously named.

5.1.3 Radio jets

Microquasars form a particular subclass of X-ray binaries, characterised by the ejection of relativistic plasma jets. These jets extend outwards to great distances from the system perpendicular to the accretion disk and are very bright in radio wavelengths. Microquasars are thus occasionally referred to as radio-X-ray binaries.

Jets are an efficient way to shed angular momentum from the inner edge of an accretion disk but the process of jet ejection is not well understood. Candidate theories must reproduce strong acceleration and collimation of ejected material. The most promising current models rely on jet ejection through a funnel out of the centre of the accretion disk, with material accelerated by strong, collimated radiation pressure (Fabrika, 2004). The accretion flow and the jet production at the inner regions of the accretion disk must be coupled, but the details are not understood.

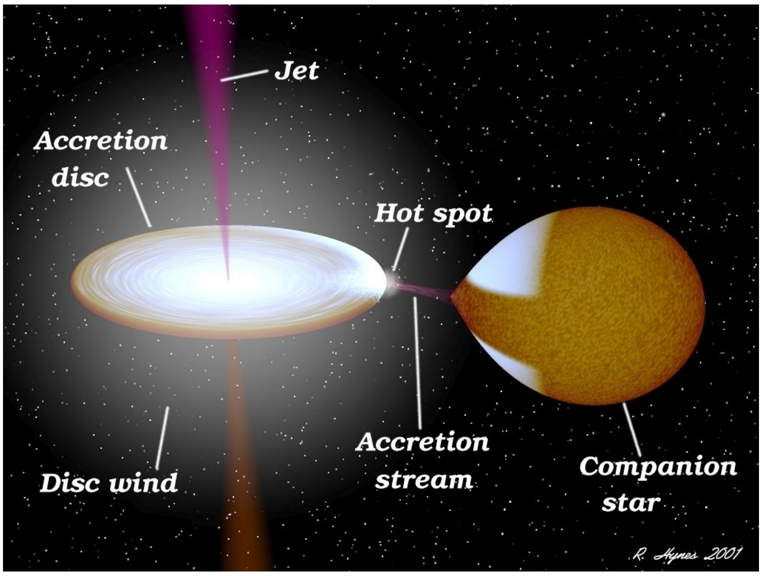

Figure 5.2: Impression of a microquasar. Image: Rob Hynes, BINSIM.

5.1.4 Astronomical Laboratories

Figure 5.2 is an impression of a microquasar showing a donor star, the accretion flow across the L1 point, accretion disk and jets. The compact object at the centre of the accretion disk is hidden from view by the surrounding material.

Microquasars are scaled-down companions of the distant and highly energetic quasars (Mirabel and Rodríguez, 1999). They present us with a local and rapidly evolving laboratory to study accretion and jet formation. Both quasars and microquasars play a significant role during galaxy formation and evolution — they enrich and stir up the interstellar medium with supernova, winds and jets. It has recently been suggested that microquasars may have played a substantial part in cosmological re-ionisation, ending the Dark Ages of the universe (Mirabel, 2011).

5.2 Observing the various components of a microquasar

5.2.1 The donor star

It is usually difficult to directly observe the donor star in a microquasar. Other components of the system tend to be significantly brighter and dominate the observed light. The exception to this rule is in the case of an eclipsing system where the compact object and accretion disk may pass behind the star along the line of sight.

5.2.2 The compact object and accretion disk

It is considered impossible to directly observe the compact object in a microquasar. Compared to the surrounding accretion disk it does not emit much energy itself and sits in the middle of an exceptionally active and bright region of mass flow. In the case where the compact object is a black hole then there is no light emitted whatsoever. Instead we look for observable signatures from the accretion disk.

The surface of an accretion disk around a stellar mass compact object is very hot and bright at short wavelengths (Shakura and Sunyaev, 1973). The composition of the light which we observe is dependent on the orientation of the disk to our line of sight.

In the unlikely case that the disk is face on to our line of sight we would attain a birds-eye-view down onto the surface of the accretion disk. Unfortunately in this configuration the jet would be pointing directly at us, and would completely obscure the system (a micro-blazar: Aharonian et al. (2005)).

At oblique inclinations of the accretion disk to our line of sight the orbital motion of the disk will cause a Doppler shift. The Doppler shift in emitted radiation is proportional to the line-of-sight velocity, and so each differently rotating region of the accretion disk will appear Doppler shifted to a different amount. Horne and Marsh (1986) show that an emission line from an inclined Kepler-rotating disk will have a specific broadened, double-peaked profile.

A simple case to consider is a ring of emitting material in a circular orbit with some rotational velocity $v_{\rm rot}$. If this ring is inclined to our line of sight with inclination i, one side of the ring will always appear to be rotating away from us, whilst the other side will be rotating towards us. From the discussion of redshift in § A.1 the maximum redshift will appear as a component of wavelength

$$\lambda_+ = \lambda_0 + \lambda_0 v_{\rm rot} \sin i / c, \tag{5.3}$$

whilst the approaching section of the disk will be maximally blueshifted to a wavelength

$$\lambda_- = \lambda_0 - \lambda_0 v_{\rm rot} \sin i / c. \tag{5.4}$$

The wavelength splitting of $\triangle\lambda = \lambda_+ - \lambda_-$ informs us of the rotational speed of the ring. The faster the disk rotates the more split $\triangle\lambda$ appears,

$$v_{\rm rot} \sin i = \frac{c\triangle\lambda}{2\lambda_0}. \tag{5.5}$$

The factor of $\sin i$ in Equation 5.5 is due to Doppler shifts being a function of line-of-sight velocity, and so strictly speaking we measure orbital velocity along the line of sight, which gives a lower limit on the true orbital velocity.

In Figure 5.3 I plot the line-of-sight orbital velocity as a function of line splitting in K-band, and in V-band for reference. In Chapter 7 I present observational data from the Gemini Telescope, obtained with the instrument "NIRI" in K-band, and so here I show that NIRI's spectral resolution of 1300 equates to a rotational velocity-resolution $\sim$ 115km/s. It is important to note that circumbinary disks will rotate much more slowly than accretion

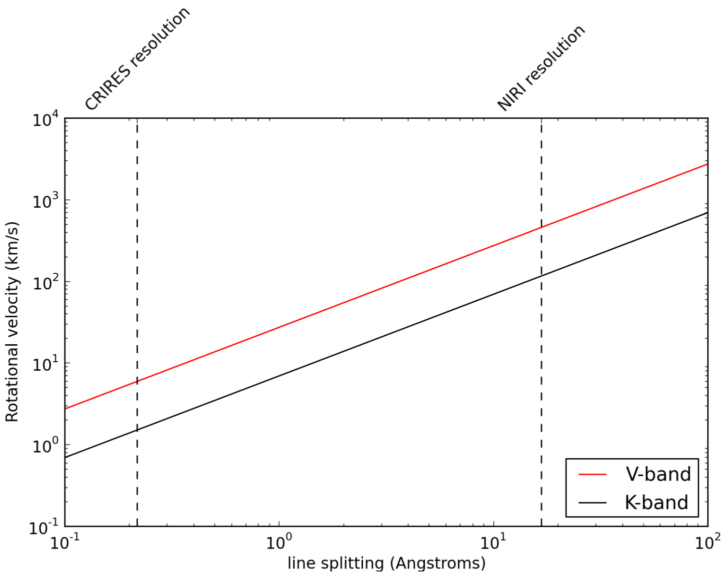

Figure 5.3: Rotational Velocity versus Line Splitting. Also shown are the spectral resolution of two K-band spectrographs — NIRI (Gemini) and CRIRES (VLT).

disks as they are located a considerable distance from the main body of the system, and as such a good spectral resolution is required for their observation.

5.2.3 Winds

Whereas jets are highly directional and travel at great velocities, winds are a significantly more isotropic and non-relativistic form of outflow. Winds from microquasars come in different varieties. In the case of high mass X-ray binaries (HMXB: § 5.1), or in microquasars with particularly hot or rapidly rotating donor stars, the stellar wind from the companion star can dominate the spectrum. These stellar winds are like the Sun's solar wind which produces the northern lights, only much more powerful.

Another source of wind can be the accretion disk itself. Begelman et al. (1983) and Begelman and McKee (1983) note that in addition to heating from within the accretion disk, its surface is exposed to highly energetic X-rays. These sources of energy should produce a high temperature corona on the surface of the disk, which steadily escapes as it is heated.

In contrast to the collimated jet, the disk wind blows from the outer region of the accretion disk, and across a wide range of angles. Disk winds serve as another mechanism of mass outflow from microquasars, and may also remove angular momentum. Whereas jets may be intermittent (Nipoti et al., 2005; Blundell, 2008), so long as there is an accretion disk we may expect a disk wind.

Winds are difficult to observe with direct imaging techniques. But due to their isotropic nature they can leave a distinct “P-Cygni fingerprint” (§ A.2) in emission lines, particularly during the eclipse of the donor star by the accretion disk (Falomo et al., 1987).

5.2.4 Jets

The jets of a microquasar may be observed on many scales. At the very base of the jet, where material is accelerated and collimated, the jet emits X-rays and possibly γ-rays. Further away from the accretion disk and the accelerating region, as the jet cools and expands, it emits ultraviolet and optical wavelengths. Then at parsec-scales the radio jets are observed.

5.3 The microquasar SS433

The microquasar SS433 was discovered in a survey of bright Hydrogen-line emitting stars (Stephenson and Sanduleak, 1977). Its spectrum showed unusual “moving” emission lines of highly red and blue-shifted components. Abell and Margon (1979), Milgrom (1979) and Fabian and Rees (1979) pioneered the “kinematic model” to explain these spectral features as originating in two oppositely directed jets moving at 0.26c. The angle of these jets was shown to precess in cone of opening angle $\sim 20^\circ$ and on a timescale of 162 days. Hjellming and Johnston (1981) later demonstrated the precession of SS433’s jets at radio wavelengths.

The precession of SS433's jets, probably due to the precession in the orientation of SS433's accretion disk, has been a constant behaviour in over 30 years of observation. In addition to this 162 day periodicity Katz et al. (1982) showed a nutational behaviour of 3° in the angle of SS433's jets with a period of ~ 6 days. This "nodding" of the accretion disk (and hence jet angle) may be due to a tidal interaction of the accretion disk with the donor star, or to perturbations in the accretion flow.

SS433 was first identified as a binary system by Crampton et al. (1980) and Margon et al. (1980) who noticed that the "stationary" (non-jet) lines of SS433 are not entirely fixed in wavelength, and exhibit an orbital periodicity of 13.1 days. Later, SS433 was shown to be an eclipsing binary with observations of eclipses of the compact object and the base of the jet.

SS433 is the only system currently known to produce baryonic jets. These are composed mainly of hydrogen and helium although numerous other elements have been detected in X-ray spectra (e.g. Lopez et al., 2006).

It is believed that the compact object in SS433 may be the progenitor of the W50 supernova remnant (Goodall et al., 2011b,a), with its jets influencing W50's elongated morphology.

5.4 A circumbinary disk in the microquasar SS433

5.4.1 Observational Appearance

Blundell et al. (2008) observed the presence of two stationary components in SS433's Balmer Hα complex in a series of 30 nightly spectra. SS433's Hα emission is complex and sometimes double-peaked. Blundell et al. (2008) demonstrated that this feature may be decomposed into a minimum of three components (see Figure 5.4):

- A strong and broad component identified to be the accretion disk wind. This central wavelength of the wind component varies with orbital period, which is to be expected as the accretion disk is red and blue-shifted by its orbital motion.
- Two narrow components, stationary in wavelength over entire orbital periods. The wavelengths of these components are fixed and do not show any variation with binary orbital motion. They are therefore identified as being circumbinary in nature.

Perez and Blundell (2009) also detected SS433's circumbinary ring in a similar way in high resolution infrared spectroscopy.

5.4.2 Discussion

Blundell et al. (2008) measured the rotation velocity of the SS433's circumbinary disk, inferred via the splitting of the circumbinary components, to be $175 - 200$km/s. With an estimate of the disk gap (§ 4.2.2) Blundell et al. (2008) determined SS433's system mass at $\sim 40\mathrm{M}_\odot$, with the compact object being a black hole of mass $\sim 16\mathrm{M}_\odot$ and a $\sim 24\mathrm{M}_\odot$ companion star.

Filippenko et al. (1988) first proposed a circumbinary excretion disk in SS433, fed by accretion overflow from the L2 point in the binary system in response to their double-peaked Paschen line spectroscopy. Fabrika (1993) remarked that the intensities of the two circumbinary lines should vary with the phase of the orbit due to a hotspot on the inner edge of the circumbinary disk, which will follow the outflowing stream of gas. Figure 5.6 shows an idealised model (not to scale) of this outflow.

Tantalisingly, the data presented in Blundell et al. (2008) do show that whilst SS433's circumbinary lines are stationary in wavelength their intensities oscillate with binary orbital period, and in such a manner as to be out of phase with each other (see Figure 5.5). SS433's circumbinary disk does appear to behave as predicted by Fabrika (1993), fed by an accretion

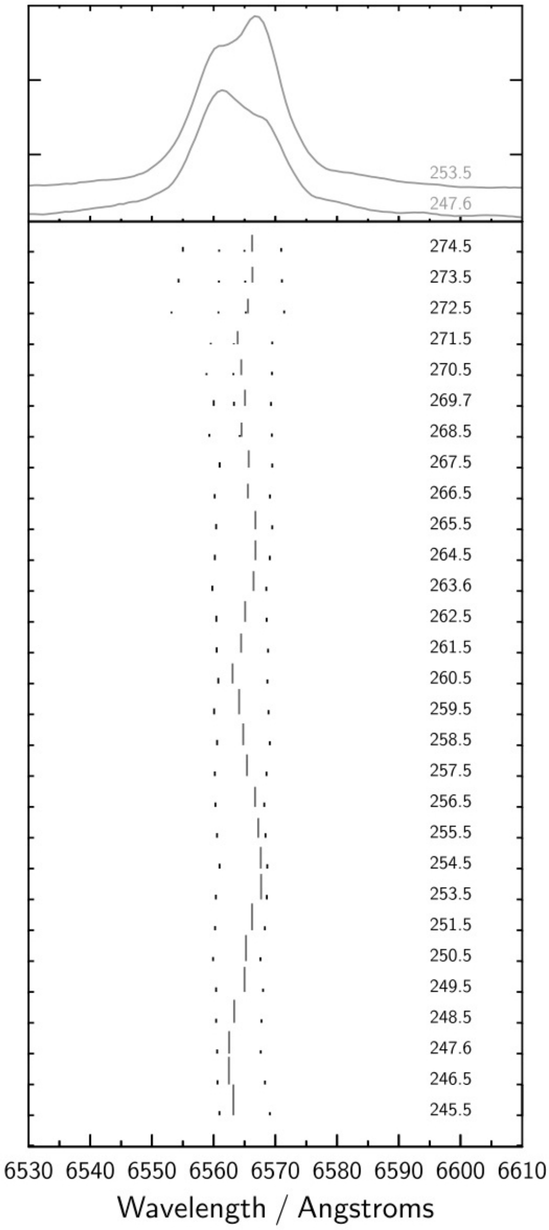

Figure 5.4: The circumbinary lines of SS433.
Reproduced from Blundell et al. 2008: their figure 1.
Upper panel: Examples of two spectra of SS433's Hα line observed half an orbital period apart.
Lower panel: Wavelengths of the deblended components in each observation.

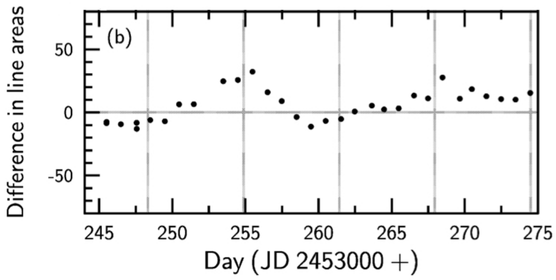

Figure 5.5: The line strengths of SS433's circumbinary lines. Reproduced from Blundell et al. 2008: their figure 3b. The grey vertical lines correspond to orbital phases of 0 and 0.5.

overflow, which creates a hotspot that moves around the inner edge of the circumbinary disk (according to orbital motion). The outflow to the circumbinary disk is a direct product of the accretion process internal to the system. Observing the circumbinary disk presents a new diagnostic tool towards the study of the dynamics of the system.

SS433's circumbinary disk represents a new means of mass-loss from this system, distinct from its radio jets and accretion-disk wind. Blundell et al. (2001) estimated the equatorial mass-loss rate to be $\sim 10^{-4} M_{\odot}/\mathrm{yr}$ (which has since been shown to be a lower limit due to the revised distance to SS433 (Blundell and Bowler, 2004)).

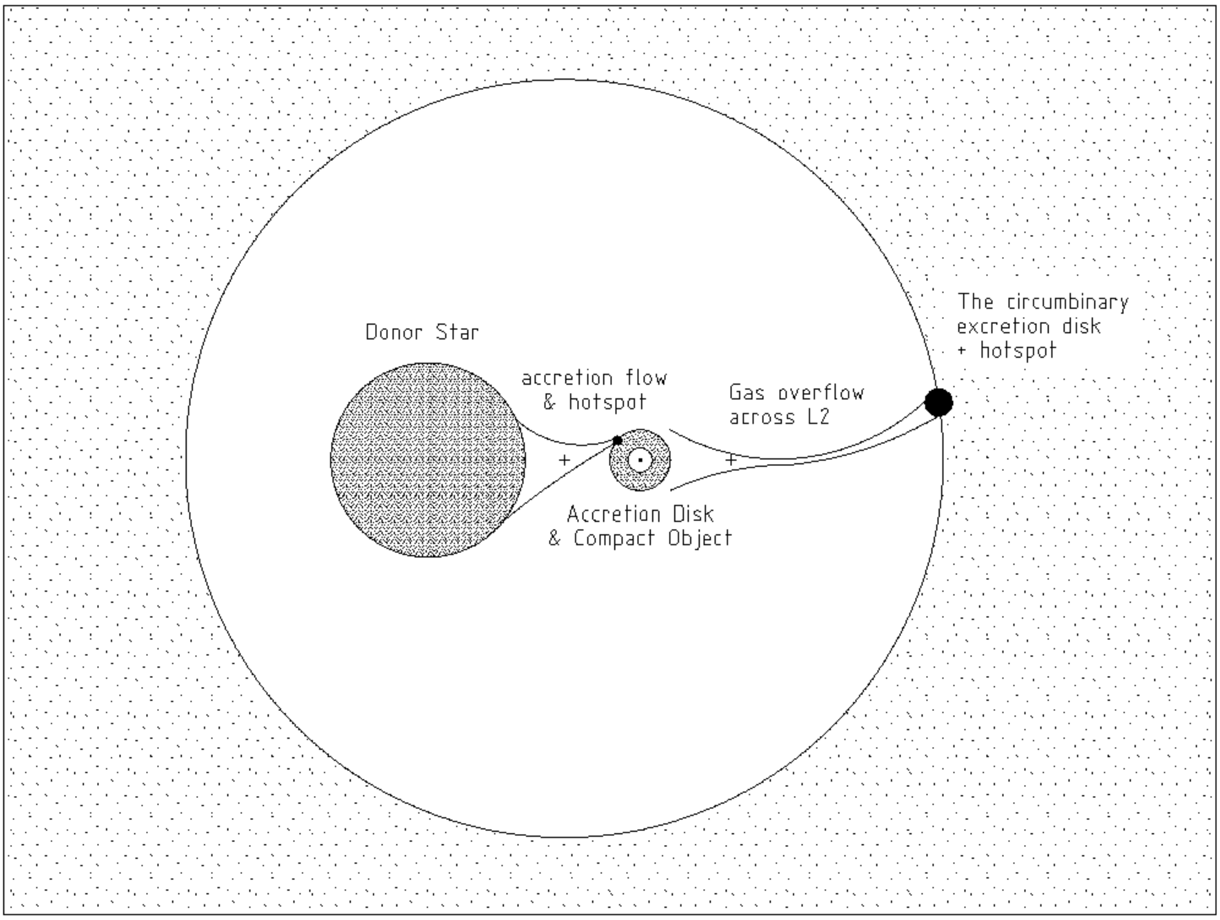

Figure 5.6: A circumbinary excretion disk (not to scale). Perez and Blundell (2009) estimate the size of SS433's binary orbit to have a semi-major axis of 150 solar radii, with a large donor star of radius ≤ 75 solar radii.

Chapter 6

The Ruff of the Microquasar SS433

The work presented in this chapter is based on Doolin and Blundell (2009).

6.1 The Ruff Feature

Imaging on milli-arcsecond scales is routine only at radio wavelengths with very long baseline interferometry (VLBI) techniques. Such techniques, applied to observations of the microquasar SS433 reveal its famous precessing, knotty jets, which lie predominantly east-west on the sky (Figure 6.1). The exact orientation of SS433's jets at any epoch is predicted fairly well by the kinematic model (§ 5.3), which encodes the systematic precession and nutation in the angle subtended by the jets relative to the binary orbital plane.

Roughly perpendicular to SS433's precessing jets is an equatorial outflowing "ruff" of radio-emitting plasma, extending up to $\sim$100 AU from the jet source, predominantly along a north-south axis (Figure 6.1 — highlighted in green). Mioduszewski et al. (2004) measure the equatorial outflow speed to be $10,000\,\mathrm{km/s}$, although the launch mechanism for these observed high speeds remains to be established.

Whilst the jets of SS433 are ejected perpendicular to the accretion disk and roughly perpendicular to the binary orbital plane, the ruff outflow is predominantly in the orbital plane of the binary. Fabrika (2004) remarks that an equatorial outflow from SS433 in the plane of the binary system is confirmed by multiple independent observations at many wavelengths.

Over the last decade, images of SS433 reveal that the orientation of the ruff changes over time with respect to a fixed sky co-ordinate grid. These observations are mainly comprised of single snapshots in time (such as those shown in Figure 6.1) except for the observing campaign of Mioduszewski et al. (2004) who undertook two months of daily observations of SS433 with the Very Long Baseline Array (VLBA). Mioduszewski et al. (2004) packaged their observations into a movie which, at the time of writing, is available with their press release[1]. In these data a steady rotation of the ruff is revealed (§ 6.2).

Blundell et al. (2008) proposed that SS433's ruff is fed by a circumbinary excretion disk. Here I investigate the viability of this scenario and discuss the implied consequences for the SS433 system.

6.2 The changing orientation of SS433's ruff

From each of the images in the Mioduszewski et al. (2004) "Summer of SS433" observational campaign, 26 June 2003 — 6 August 2003, I extracted an estimate of the mean angle of the ruff. Angles are measured on the sky anti-clockwise from celestial north (rotating into east). These data are plotted in Figure 6.2, and whilst the uncertainty in each measurement is at least 5° a clear and steady rotation through $\sim 10°$ is observed over the course of these two months.

We supplement the data presented in Figure 6.2 with ruff angles measured from images presented by Paragi et al. (1999); Blundell et al. (2001); Paragi et al. (2002) and Paragi

---

[1] `http://www.nrao.edu/pr/2004/ss433/`

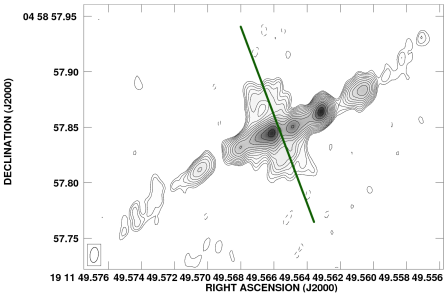

(a) 7 March 1998, Blundell et al. (2001) (their fig. 2)

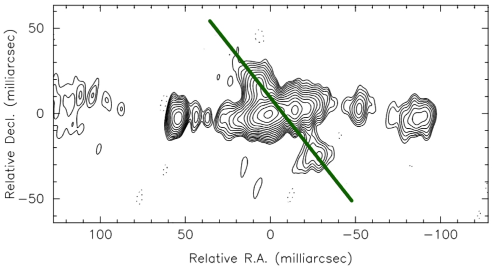

(b) 6 June 1998, Paragi et al. (2002) (their fig 3)

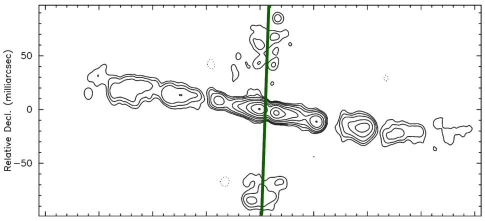

(c) 13 Feb 2000, Paragi et al. (2002) (their fig 3a)

Figure 6.1: Radio images of SS433 on milli-arcsec scales showing the precessing jets (east-west) and the *differently* precessing ruff (north-south) — highlighted in green.

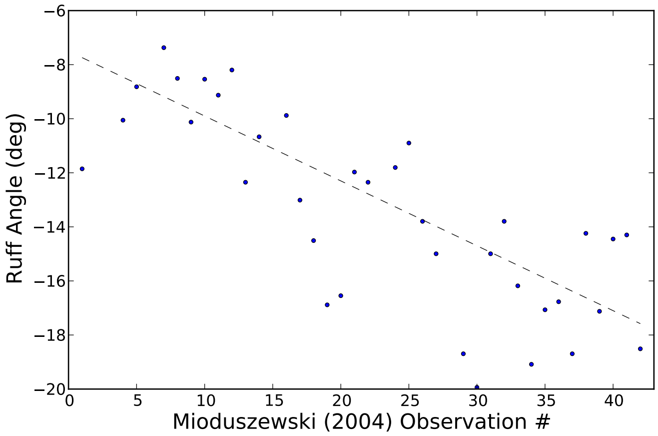

Figure 6.2: The orientation of SS433's ruff with trend line (data from Mioduszewski et al., 2004). Observations are daily commencing 26 June 2003.

et al. (2002), covering VLBI observations of SS433 from 1995 to 2003. We show a subset of these images in Figure 6.1 that clearly demonstrates the change in angle, projected on the plane of the sky, of SS433's ruff with time.

From each of the VLBI images available we extracted this "ruff angle", measured anti-clockwise from celestial north. Where more than one published image was available for a given observation we measured all images. Higher resolution images reveal inner (more recently launched) ruff material, compared to the more extended ruff emission visible in lower-resolution images.

We infer the epoch of emission (hereafter referred to as the "corrected" date) via the extent of the features of the observable ruff assuming a distance to SS433 of 5.5 kpc (Blundell and Bowler, 2004) and the average wind speed of $10,000\,\mathrm{km/s}$ as reported by Mioduszewski et al. (2004). These corrections, which relate observations on different scales back to the epoch of emission, are of order 30 days.

In Figure 6.3 we plot the ruff angle as a function of corrected Julian Date. These data clearly show systematic variations through a range of at least 50°. We also show

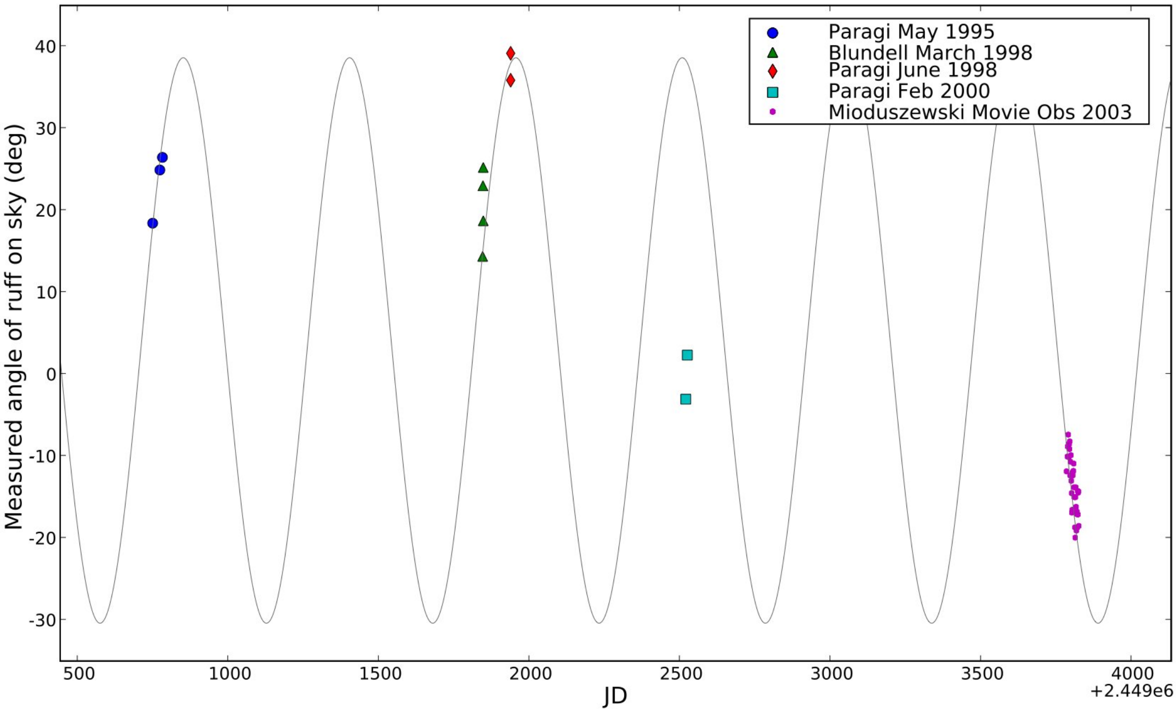

Figure 6.3: SS433's Ruff Angle vs Corrected Julian Date. The sinusoid was fitted *only* to the Mioduszewski et al. (2004) data; details in text.

in Figure 6.3 the best fitting sinusoid. This fit is *only* to the Mioduszewski data-points, giving an initial guess for the amplitude of 35° with no vertical offset, after which frequency, phase, amplitude and vertical offset are fitted.

It is remarkable that many of the earlier data points lie (without any further fitting) on this sinusoid, which shows a periodicity in the apparent angle of the ruff of 552.5 days, which is equivalent to 42.2 binary orbital periods. This period is constrained by the slope of the highly time-resolved Mioduszewski et al. (2004) data, and the fit is not significantly improved by considering all data points.

6.3 Independence of ruff motion from other periodicities

We first consider whether the apparent precession of SS433's ruff simply reflects other known periodicities in the SS433 system. There are three known periodicities to consider:

1. SS433's jet axis precession period of 162.375 days (Eikenberry et al., 2001)
2. SS433's binary orbital period of 13.08 days (Kemp et al., 1986)
3. SS433's jet nutation (or nodding) period of 6.06 days (Katz et al., 1982)

Fortunately, the time sampling of the available data enable us to rule out such correlations. In Figure 6.4 we plot the measured ruff angles folded over SS433's three major periodicities and show an absence of a preferred ruff orientation with orbital, nodding or precession phase. We note that the periodicity plotted in Figure 6.3 of 552.5 days is neither commensurate with the precession period, orbital period, nor nodding period.

We also remark that the fit to the ruff angle varies through 69°, whereas the jet angle projected on the plane of the sky only has a range of 40° (Hjellming and Johnston, 1981).

6.4 An inclined circumbinary disk

Blundell et al. (2008) posited that SS433's ruff is fed from its circumbinary disk. But as demonstrated above, the ruff rotates in orientation on the sky. A solution to this problem lies in the supposition that SS433's circumbinary disk is inclined to the plane of the binary, and therefore the change in ruff angle arises because of an evolution in the orientation of this circumbinary structure.

Since SS433 is an eclipsing system its orbital plane must lie (nearly) orthogonal to the plane of the sky. Consider an inclined prograde circumbinary disk about such a binary

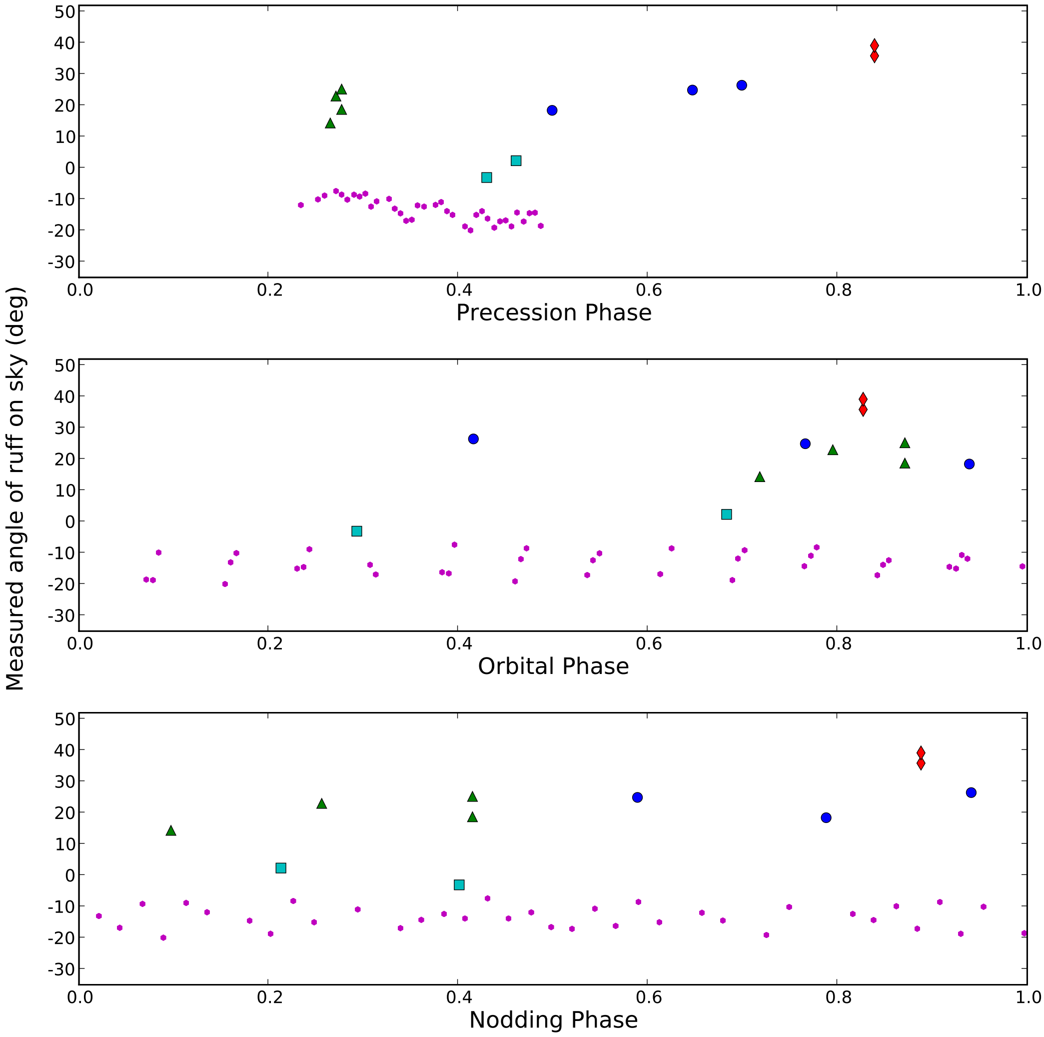

Figure 6.4: SS433's observed ruff angle folded over precession, orbital and nodding phases, showing no discernible dependences. Legend as Figure 6.3.

system. If the circumbinary disks behaves according to the librating mechanism described in Chapter 3 (exhibiting a precession in the longitude of the ascending node of all orbits), then when we consider the projected plane of this evolving disk on the sky we recover a behaviour which closely matches the observed ruff evolution of Figure 6.3.

Put a different way, the circumbinary libration mechanism causes the projection onto the sky of an inclined circumbinary disk to oscillate back and forth across the edge-on plane of the binary.

6.4.1 A preferred inclination

From the fit shown in Figure 6.3 we deduce that the ruff precesses with an amplitude of 34.5°. At the maxima and minima of the curve the plane of the circumbinary disk contains our line of sight, actually perpendicular to the plane of the sky. Since the orbital plane is also into the plane of the sky we determine that the circumbinary disk is therefore inclined to the plane of the binary by 34.5°.

But what could determine this preferred angle? There has been the occasional suggestion that SS433 may be a triple star system (see e.g. Fabian et al., 1986). These theories attempt to explain the multitude of periodicities, and their regularity, within the SS433 system by invoking an external counterpart. But there is little direct evidence thus far to support such claims.

6.4.2 Determination of orientations within SS433

Our fit also tells us the angle of rotation of the plane of the binary from north-south. Since we assume a symmetry in the precession of the ruff, spending equal time rotated clockwise and anticlockwise from the plane of the binary, the offset of the fit tells us that the plane of the binary (into the sky) is rotated $\sim 2°$ east of north.

This angle is comparable with, but not equivalent to, the mean angle perpendicular to SS433's radio jets of $\sim 10^\circ$ east of north (Hjellming and Johnston, 1981; Blundell and Bowler, 2004). But since the jets are produced by a warped and possibly non-co-planar accretion disk around the compact object we think this disagreement may be informing us about misalignment of the disk plane and jet-launch axis.

6.5 Physical parameters

Comparing the results of our simulations (Chapter 3) describing the period of circumbinary nodal precession (Equation 3.5) with observations of SS433's ruff angle (Figure 6.3) we conclude that to achieve a circumbinary precession period as short as the observed ruff precession period of ~ 42 binary periods, we require some fairly limiting conditions.

To satisfy Equation 3.5 under the constraint of a precession period of ~ 42 binary periods we are required to consider orbits close to the binary system. Here we must take into account that not all such orbits are stable, as explored in Chapter 4, and as such it is necessary to minimise Equation 3.5 in the space of stable orbits, as a function of binary eccentricity, mass fraction and orbital radius. This implies a significantly non-zero value for both SS433's binary eccentricity and mass fraction.

It is also necessary to conclude that SS433's circumbinary disk is present at the innermost allowed stable orbit (Chapter 4), i.e. an orbital radius of close to twice the binary semi-major axis. It could be the case that the inner edge of SS433's circumbinary disk lies within the unstable region (see § 4.4), which may be permitted if the disk is continually fed at these radii. This does seem to be the case in the spectroscopy of Blundell et al. (2008).

6.5.1 Independent constraints on SS433's orbital eccentricity and mass fraction

Optical photometry, such as in Kemp et al. (1986), reveals that SS433's primary and secondary minima eclipses lie close to 0.5 of an orbital phase apart. This points towards a circular (non-eccentric) orbit, but is not conclusive because the orbit could still be eccentric if the axis of symmetry[2] is along our line-of-sight.

There are other pointers towards a non-zero eccentricity in SS433's orbit. First, the sinusoidally varying component of the jet speed (Blundell and Bowler, 2005; Blundell et al., 2007) depends on orbital phase, implying a break in the symmetry of the orbit. Second, Perez and Blundell (2009) find that the radius of the companion star must be rather large ($> 39\mathrm{R}_\odot$) if the orbit is circular; but smaller radii for the star are permitted if the orbit has some eccentricity.

Blundell et al. (2008), from over a month of high resolution optical spectroscopy of the circumbinary disk, extracted the masses of SS433's binary components as being $\sim 16\mathrm{M}_\odot$ for the compact object and $\sim 24\mathrm{M}_\odot$ for the companion. On the basis of this measurement a mass fraction of ~ 0.4 seems likely, i.e. significantly different from equal masses.

6.6 Conclusions and further work

In Doolin and Blundell (2009) we remarked that the changing orientation of the precessing circumbinary disk will be manifested in how split the circumbinary lines appear to be. When the circumbinary disk is orthogonal to the plane of the sky the circumbinary line-splitting will be enhanced. And when the circumbinary disk appears to align with the plane of the binary it will be maximally face-on to Earth, and hence the line-splitting will be reduced, and with insufficient spectral resolution, becomes harder to resolve.

---

[2] binary orbital semi-major axis

We have been awarded a long-term VLBI monitoring study to track the precession of SS433s ruff over the coming few years. This will test the predictive capabilities of the inclined circumbinary disk model.

I conclude that the motions of collective orbits, comprising circumbinary disks, have considerable potential to reveal system properties, if suitably time-resolved, high-resolution data are available.

Chapter 7

A Pilot Search for Circumbinary Disks in Microquasars

A circumbinary disk has recently been discovered around the microquasar SS433. Blundell et al. (2008) observed the presence of two stationary components in SS433's Balmer Hα complex in a series of 30 nightly spectra (§ 5.4). The question posed by these observations is to ask whether SS433's circumbinary disk is a unique feature, or perhaps we should expect there to be a circumbinary component to all interacting binary systems. To address this issue I present the results from a small pilot survey of Galactic microquasars in search of circumbinary disk characteristics.

7.1 Technical Considerations

In view of the significant extinction towards many Galactic microquasars in optical bands (Mirabel et al. (1994) report an optical extinction towards GRS 1915+105 of $\gtrsim 30$!) this survey is executed in the near infrared. Infrared extinction due to interstellar dust along the line of sight to targets in the galactic centre can be an order of magnitude less than optical extinction (Cardelli et al., 1989). The microquasar SS433 shows exceptionally clear emission lines in the near-IR, particularly the Brackett-γ line at $\lambda = 2.17\mu$m (see figure 3 of Perez and Blundell, 2009) which lies in the K-band. Also the Brackett-γ line lies in a comparably transparent region of atmospheric absorption (Figure 7.1) and hence is the target line in this survey.

7.1.1 Instrument

The data presented here are near-IR K-band spectra of three microquasars CI Camelopardalis (CI Cam), GRS 1915+105 and Cygnus X-3, taken with the Gemini North 8.1m Telescope on Mauna Kea, Hawai'i. The program identification number is GN-2009A-Q-98.

The instrument used is Gemini's Near InfraRed Imager and Spectrometer (NIRI) (Hodapp et al., 2003; Hora et al., 1995). NIRI was used in long-slit spectroscopy mode with the f/6 camera, a 2 pixel slit mask and K-grism disperser ($\lambda = 1.90...2.49\mu$m). In this mode NIRI can achieve a spectral resolution $\lambda/\delta\lambda = 1300$ which equates to a velocity resolution of $\sim$ 230km/s (see discussion in § 5.2.2).

7.1.2 Observing Schedule

The key to identifying emission from regions external to a binary system is to demonstrate spectral components which are independent of the binary orbital motion, i.e. stationary in wavelength. I therefore required time resolved and sub-orbital-period observations, preferably covering 6 epochs during each target's orbit. The requested observing schedule is shown in Table 7.1.

Fortunately the targets are unusually bright in K-band, such that observations may be executed under cloudy conditions or in poor seeing. This flexibility makes the time cadencing possible as Gemini North is a queue-operated telescope. Exposure times were calculated

Table 7.1: Target Microquasars and requested observing schedule

Target	Orbital Period	Schedule
CI Cam	19.41 days	every 3 ± 1 days
GRS 1915+105	30.8 days	every 5 ± 1 days
Cygnus X-3	4.79 hours	1 night

using K-band magnitudes from the literature (SIMBAD Astronomical Database[1], which quotes 2MASS magnitudes, (Cutri et al., 2003)) to achieve a signal to noise > 20. Whilst this provides a good estimate for the exposure time required to detect the continuum it cannot account for variations in local conditions or the relative line strengths of the targets. Each observation was performed in a minimum of four separate exposures to facilitate removal of cosmic rays. A guide star was identified for each target.

7.1.3 Atmospheric background and absorption

Observing in the infrared from a ground-based telescope is trickier than in the optical because at infrared wavelengths the atmosphere is not necessarily transparent. Atmospheric emission, or sky background, is dominated by narrow hydroxyl (OH) lines. These lines vary in brightness by 5 to 10% and on a timescale of ~ 10 minutes as the atmosphere shifts.

To compensate for this rapidly changing sky background we use a technique called "nodding along the slit" or "nod and shuffle". Instead of putting the target in the centre of the slit in the spatial axis each observation is divided into two telescope pointings: (A) with the target moved -5" along the slit, and (B) with the target moved +5" along the slit respectively. In this manner the target spectrum falls along a different region of the CCD. We then subdivide an observation into a number of sequences of the positions $\{ABBA\}$.

---

[1] The SIMBAD Astronomical Database is operated at CDS, Strasbourg, France

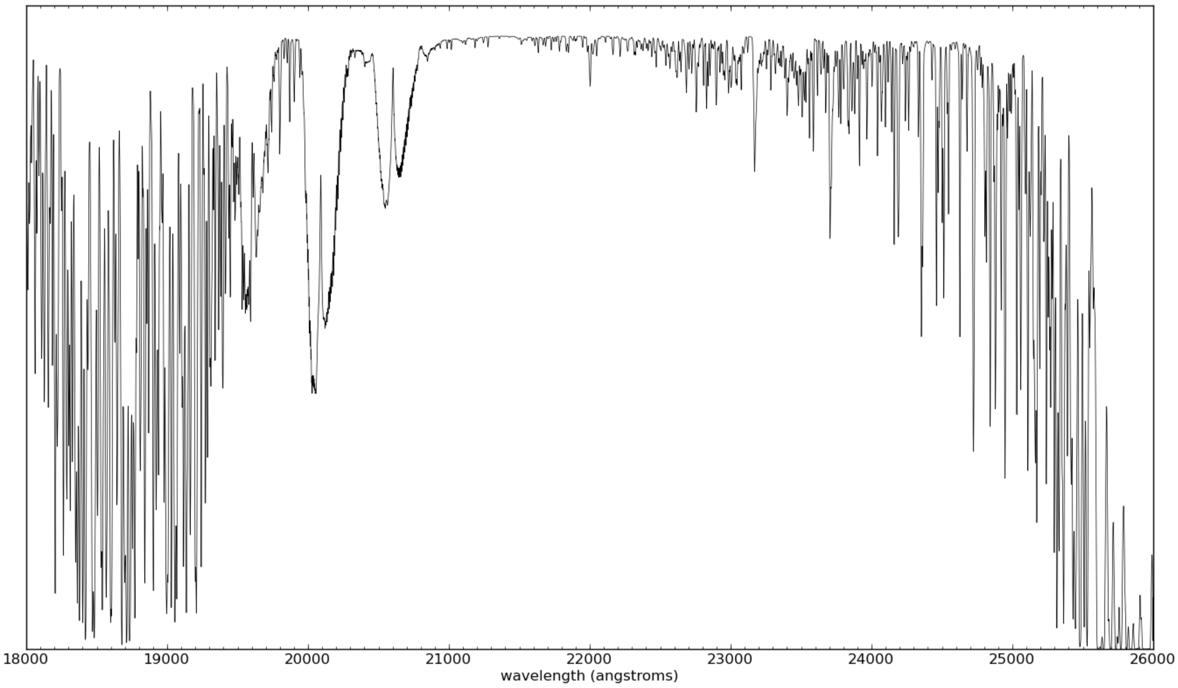

Figure 7.1: Atmospheric transmission in the infrared K-band

In the data reduction (§ 7.2.6) we use neighbouring positions to remove sky lines from each other via a pixel-for-pixel subtraction, where the target spectrum which we wish to preserve is maintained due to the 10" offset in the spatial axis. The $\{ABBA\}$ sequence also compensates for a linear change in sky brightness with time.

The second problem with the atmosphere in the infrared is "telluric" absorption. Water vapour in the atmosphere absorbs a significant amount of incoming stellar infrared radiation at various discrete wavelengths. Figure 7.1 is a plot of a synthetic sky transmission function in the K-band with an optimistic water vapour column of 1mm as generated by the ATRAN code (Lord, 1992). The water vapour column varies across the sky with airmass, amongst other things, and temporally on a timescale $<$ hours.

To compensate for the telluric sky absorption we also observe a "telluric" standard star with each science observation. This extra observation is not for the usual purpose of flux calibration, as is standard practice at optical wavelengths, but the star is purposefully chosen to have a smooth and featureless spectrum. Knowing that the telluric star has a smooth spectrum one may infer that any features observed in the telluric star's spectrum are in fact imposed by the atmosphere, and hence a wavelength-specific telluric correction may be applied to the science spectrum (§ 7.2.7).

Extremely hot stars of types O and B have few spectral features, and as such are ideal candidates for telluric standards. Unfortunately stars of these types are rare and it is important to ensure that the telluric observation samples the same column of atmosphere as the science observation, hence the two cannot be greatly separated in position on the sky.

7.1.4 Data reduction tools

To perform the data reduction I used the Image Reduction and Analysis Facility (IRAF) (Tody, 1986, 1993) provided by the National Optical Astronomy Observatories. Additionally I used the Gemini IRAF Package (Version 1.10), released and maintained by Gemini, which integrates instrument-specific functionality into IRAF via a suite of additional tasks.

IRAF was not used directly but rather integrated into PYTHON with the PYRAF module to take advantage of the flexibility and functionality offered by the PYTHON programming language and modules such as PYFITS, NUMPY and MATPLOTLIB.

I also used the PYTHON scripts *nirlin.py* and *cleanir.py*, released by Gemini to linearise saturated pixels and remove characteristic CCD features from the data where possible.

7.2 Reduction Pipeline

7.2.1 Data Format

The raw data from each observation were captured by the instrument NIRI and written to disk in Multi-Extension FITS[2] (MEF) files. Each observation consists of:

- Flat fields (§ 7.2.3).
- Argon arc lamp spectra for wavelength calibration (§ 7.2.4).
- Telluric observations - one file for each observation in the $\{ABBA\ldots\}$ sequence.
- Science observations - one file for each observation in the $\{ABBA\ldots\}$ sequence.

IRAF is built to handle these files, keeping track of reduction parameters and information in header data. Additionally tasks supplied in the Gemini IRAF Package create and propagate data quality and variance planes to track bad pixels and signal levels throughout the reduction.

7.2.2 Dark Frames

We did not take any dark frames. The primary purpose of calibrating via dark frames is to characterise the thermal noise of the detector, but with our $\{ABBA\}$ nodding and later sky subtraction (§ 7.2.6) we remove the dark current along with the sky emission lines.

The secondary purpose of taking dark frames is to catch hot pixels in the detector. In this reduction I make use of the bad pixel mask supplied by Gemini for the NIRI instrument as a baseline. This pixel mask is updated at various points during the reduction as additional bad pixels are identified.

---

[2] Flexible Image Transport System

7.2.3 Flat Field

The flat field characterises the pixel-by-pixel baseline response of the CCD to a bright uniform illumination. Approximately 10 flats are taken to produce an averaged final flat. The calibration flat frames are checked individually for an anomalous mean or standard deviation, with bad frames rejected, before being passed through the following reduction:

1. Cut the unilluminated edges of the CCD out of each frame.
2. First the flat fields are averaged and a smoothed illumination pattern is generated. Then then the flats are divided by the illumination pattern, averaged again, and finally normalised to produce the individual pixel response to a constant illumination across the CCD — the final flat. This procedure also performs pixel rejection and updates the bad pixel mask.

7.2.4 Wavelength Calibration

An observation of an argon arc lamp is used to wavelength calibrate the spectra:

1. Cut the unilluminated edges of the CCD out of each frame.
2. Apply the flat field correction by dividing each pixel by its counterpart in the final flat.
3. Apply an approximate wavelength solution (provided in the Gemini IRAF Package) to the arc lamp files to provide an initial guess for the following procedure.
4. Establish the wavelength calibration from the arc lamp spectra. A database of expected argon lines is mapped onto the observed image in order to fit a precise wavelength — dispersion solution.

7.2.5 Spatial Distortion

The telluric observations are first used to compute a spatial distortion correction. This step is not normally required, but the observations here possess a small rotation, suggesting that the slit is out of alignment with the CCD by $\sim 5^{\circ}$. To determine a more precise spatial distortion correction one generally takes a specific set of calibrations, stepping a bright star all the way along the slit. Unfortunately we did not run this calibration, but the tellurics are bright enough to allow a low order spatial distortion correction to be computed.

1. Cut the unilluminated edges of the CCD out of each frame.
2. Apply the flat field correction by dividing each pixel by its counterpart in the final flat.
3. Combine the spectra (via a pixel-for-pixel addition).
4. Use the curvature of the bright telluric spectra in the spatial axis to derive a low-order s-distortion correction.

7.2.6 Spectral Extraction

Once telluric and science observations were reduced a 1D spectrum was extracted from each by the following process:

1. Cut the unilluminated edges of the CCD out of each frame.
2. Apply the flat-field correction by dividing each pixel by its counterpart in the final flat.
3. Sky subtract the images. Recall that an observation is comprised of a sequence of the positional offsets A and B. For clarity consider this sequence to be $\{A_1 B_2 B_3 A_4 \ldots\}$.

Each frame is assigned its nearest neighbour of the alternate position as a sky image, and a pixel-for-pixel subtraction performed. For example $A_1 \to A_1 - B_2$, producing an image with a positive spectrum at position A and a negative spectrum at position B, but importantly no sky lines! A typical reduction is shown in Figure 7.2.

4. Each of the sky-subtracted images is rectified according to the wavelength dispersion solution and spatial distortion information derived earlier in the reduction.

5. We then shift all images along the spatial axis to align the positive spectra. This is enhanced, where possible, with a cross-correlation search for the optimum spatial shift. Once all images are aligned an average is computed, with bad pixels rejected via a sigma-clipping algorithm.

6. Finally a 1D spectrum is extracted from the averaged central spectrum in the combined image.

7.2.7 Telluric Correction

The telluric spectrum was inspected and any photospheric features were carefully removed. Atmospheric lines are modelled with Voigt profiles — the convolution of a Lorentz profile (to characterise pressure broadening) with a Gaussian (doppler broadening). Once fitted, telluric features were subtracted to produce a clean telluric spectrum.

Atmospheric features were removed from the science spectrum by normalising the cleaned telluric to a typical continuum value of ~ 1 and then dividing through the science spectrum.

The above reduction does not flux calibrate the spectra. A reasonable approach to do so would be to divide the telluric spectrum by a stellar model of an appropriate type and

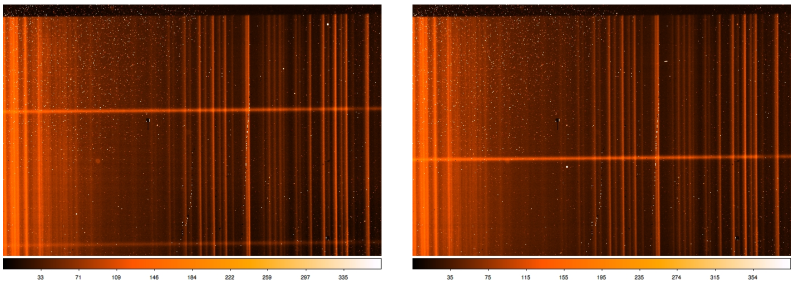

(a) position *A* (b) position *B*

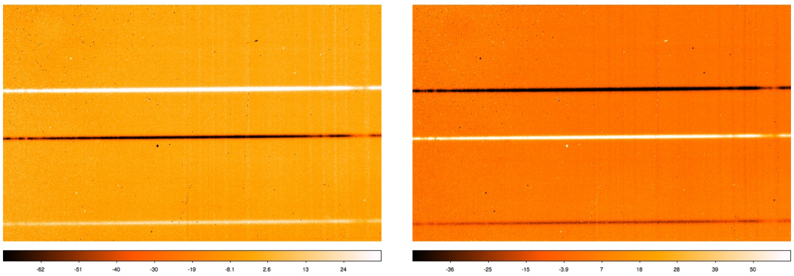

(c) $A - B$ (d) $B - A$

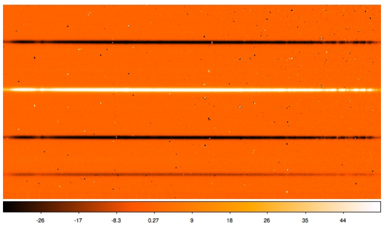

(e) shifted and combined

Figure 7.2: A typical reduction

temperature, rather than normalising the continuum to ~ 1. The telluric correction would then additionally apply an approximate flux calibration.

We do not flux calibrate because we are much more interested in the shape of any line features found in the science spectrum than the absolute strength of these lines.

7.2.8 Signal to Noise

The signal to noise (S/N) of each observation was computed via two methods:

1. The tasks supplied in the Gemini IRAF Package create and propagate data quality and variance planes throughout the reduction. The science data were divided by the square root of the variance, and a typical value taken in order to estimate the signal to noise.
2. The final spectrum was median-smoothed to compute an approximate continuum. The continuum is subtracted from the spectrum, regions with spectral features are rejected, and the noise in the result is measured.

7.3 Line Deblending

To investigate individual spectral features we make use of a deblending procedure to identify individual components within a complex profile.

The procedure of continuum subtraction described in § 7.2.8 was considered unreliable in preserving the exact line shape of a feature, however the methods described there to estimate the signal to noise of each spectrum are sound.

We consider a region of the spectrum encompassing a feature of interest, including as much clean continuum on either side as possible. The data are a set of unscaled (not flux calibrated) spectral brightnesses $\boldsymbol{S}_i$ binned across wavelength space $\boldsymbol{\lambda}_i$, along with a measurement of the root-mean-squared noise σ_0 present in the spectrum.

A model M is considered as a function of $\boldsymbol{\lambda}_i$, $\boldsymbol{M}_i = f(\boldsymbol{\lambda}_i)$, which aims to fit the spectrum $\boldsymbol{S}_i$. The model is comprised of a number of components, the first of which is a continuum term C which has the form of a low-order ($n \leq 2$) polynomial:

$$C(\boldsymbol{\lambda}, a, b, c) = a + b\boldsymbol{\lambda} + c\boldsymbol{\lambda}^2. \tag{7.1}$$

Additional components of the model M are Gaussian profiles G_j:

$$G_j(\boldsymbol{\lambda}) = G(\boldsymbol{\lambda}, A_j, \mu_j, \sigma_j) = A_j \exp\left\{-\frac{(\boldsymbol{\lambda} - \mu_j)^2}{2\sigma_j^2}\right\}, \tag{7.2}$$

producing a final model M of:

$$M = C + \sum_j G_j. \tag{7.3}$$

The model parameters $\{a, b, c, A_1, \mu_1, \sigma_1, \ldots\}$ are stepped iteratively from initial guesses to minimise the chi-squared parameter given by

$$\chi^2 = \sum_i \left(\frac{\boldsymbol{S}_i - M(\boldsymbol{\lambda}_i)}{\sigma_o}\right)^2. \tag{7.4}$$

This fitting procedure is carried out in PYTHON using the SCIPY.OPTIMIZE module, which is a wrapper around MINPACK's LMDIF and LMDER algorithms.

7.3.1 Model Selection

The fitting procedure described above will iterate towards a local minimum of χ^2 based on the initial guess for each of the fitting parameters. It is therefore essential to provide the algorithm with a reasonable initial guess, and to apply intuition to the result to ensure that the final fit has no unphysical components.

The above procedure computes the best fitting model for a fixed set of n_{gauss} gaussian components. But surely a model of $n_{\text{gauss}} + 1$ components will produce a better fit to the data? The solution to this conundrum is to consider the reduced chi-squared for each model

$$\chi^2_{\text{reduced}} = \frac{\chi^2}{n_{\text{wavelength bins}} - n_{\text{fitting parameters}} - 1}. \tag{7.5}$$

Whilst the chi-squared is weighted to account for noise in the data (σ_0) the reduced chi-squared is weighted to additionally account for the number of fitting parameters versus the quantity of data available. A reduced chi-squared < 1 implies that the model is over-fitting, hence fitting the noise and not extracting any useful information.

The judgement of whether a model requires another component is made by inspecting the residual $\boldsymbol{S}_i - M(\boldsymbol{\lambda}_i)$ after fitting, and checking if the reduced chi-squared is > 1. For example, in Figure 7.3 a model of one gaussian has been fitted to the Brackett-γ line of CI Cam. The residuals of this fit clearly show additional features in the line which have not been modelled, and the reduced chi-squared is 3.01, permitting the inclusion of further components. For the full and continuum subtracted fit see Figure 7.5.

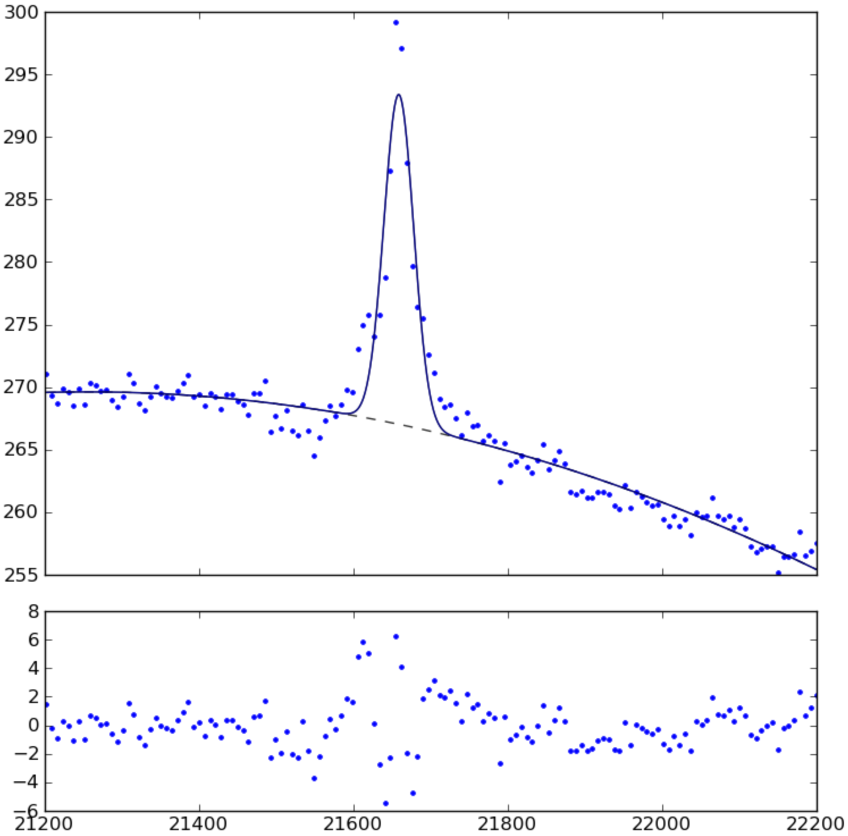

Figure 7.3: A partial fit to the Brackett-γ line of CI Cam.
Upper panel: data & single gaussian fit.
Lower panel: residuals.
The x axis has units of wavelength (Å) and the y axis has units of (flux / σ).

7.4 CI Cam

Hjellming et al. (1998a) first identified the star CI Cam as the optical counterpart to the X-ray source XTE J0421+560 which exhibited a large outburst in April 1998. Hjellming et al. (1998b) claimed to directly observe radio jets in observations taken with the Very Large Array Telescope shortly after this flare, but these proved difficult to confirm. Mioduszewski et al. (1998a). Miller-Jones et al. (2008) investigated the radio emission of CI Cam with very long baseline interferometry using the High Sensitivity Array. They report synchrotron radiation, possibly from a jet.

CI Cam is identified as a B[e] supergiant X-ray binary. The supermassive B[e] donor star is determined by Hynes et al. (2002) via a compilation of spectroscopic observations and supported by Robinson et al. (2002). These authors suggest a two-component wind from the donor star, typical of massive winds from supermassive B[e] stars (Stee, 1998). The geometry is a fast, hot polar wind and a slower, dense equatorial outflow. Yan et al. (2007) attributed their double-peaked spectroscopy to a circumstellar disk around the donor star.

The nature of the CI Cam's compact object is debated. Ishida et al. (2004) argue in favour of a white dwarf, a conclusion supported by Barsukova et al. (2006). Whilst other authors (Robinson et al., 2002; Hynes et al., 2002; Belloni et al., 1999) prefer a neutron star or black hole.

It was long accepted that CI Cam was situated at the centre of a spherical shell of warm dust due to a mid-infrared excess in the spectral energy distribution. But Thureau et al. (2009) showed that the infrared-emitting region is elongated, confirming a disc-shaped circumstellar environment via long baseline optical interferometry.

Barsukova et al. (2005, 2006) identified CI Cam's orbital period of 19.407 ± 0.020 days in a study of 7 years of optical monitoring. They fit an elliptical orbit of $e = 0.62$ and conclude system components of a type B4 III-V[e] donor star and a white dwarf plus

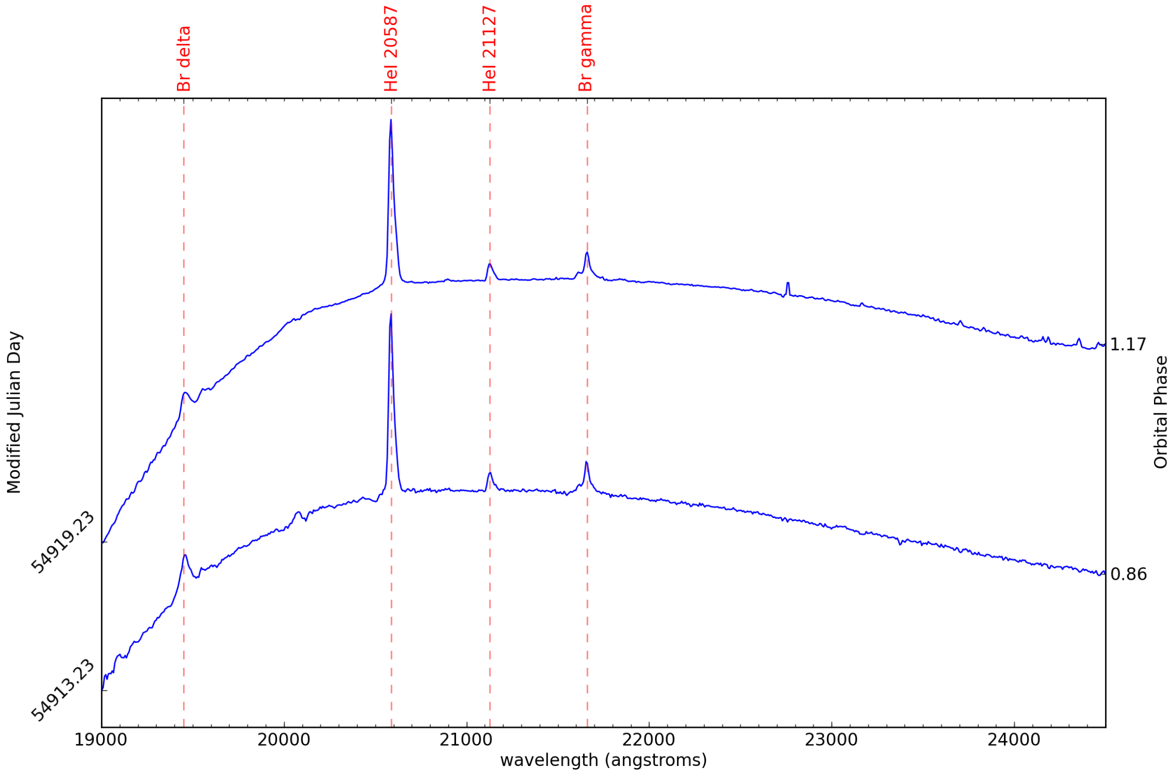

Figure 7.4: K-band spectra of CI Cam

accretion disk, with an inferior conjunction of the compact object at Modified Julian Day 52199.0 ± 0.2, thereafter defining orbital phase zero.

7.4.1 Our observations

Of the six requested observations of CI Cam unfortunately only two were executed during the telescope observing semester. But these two spectra, shown in Figure 7.4, have excellent signal to noise (~ 25), strong emission features, and are well worth consideration.

The emission lines present in CI Cam's K-band spectra (see Table 7.2) are identified from infrared line lists provided by the Joint Astronomy Centre, the Atomic Line List maintained by Peter van Hoof, and lines in Cox (2000). The Brackett-δ line is resolved at the far blue end of the spectrum, even though this wavelength lies in the wings of the filter

Table 7.2: CI Cam — spectral lines

Species	Transition	Wavelength (Å)
H I	Brackett-δ : $n = 8 - 4$	19451
He I	$2p\ (^1P^\circ) - 2s\ (^1S)$	20587
He I	$4s\ (^3S) - 3p\ (^3P^\circ)$	21127
H I	Brackett-γ : $n = 7 - 4$	21661

profile. The neutral helium line at 20587Å is the strongest feature in the spectrum, but unfortunately this line lies in a deep and complex region of atmospheric absorption (see Figure 7.1) and given poor, moist observing conditions, the precise line shape, especially in the wings, should not be considered exact.

7.4.2 Brackett-γ

The Brackett-γ complex of CI Cam shows fascinating and well resolved structure. The line itself is broadened to an approximate full width half max (FWHM) of ~ 45Å and has definite shoulders. Deblending this line as described in § 7.3 I find a best-fit model which accommodates four components. These models are continuum subtracted and plotted in Figure 7.5. Qualitatively, on the assumption that there are good analogies between the features which we observe and the components of the system (§ 5.2) we identify:

- A broad FWHM 67 ± 5Å component which accounts for $\sim 40\%$ of the line flux, likely to be a strong wind.
- A sharper component of FWHM 20 ± 3Å, providing a further $\sim 40\%$ of the line flux. This component could be a second wind (Hynes et al., 2002; Robinson et al., 2002), but I suggest that it could equally be the signature of a slowly rotating and hence unresolved disk. If this line were correctly identified as arising from circumbinary orbiting material then its width gives an upper limit on the circumbinary orbital

speed of 138 km/s. However the only way to discriminate between the two competing theories is with higher spectral and temporal resolution follow-up observations. If we can show that this component is stable in wavelength to a very good degree of accuracy, and at various orbital phases, then it must be circumbinary.

- Two smaller narrow components are required to model the shoulders of the line and make up the remaining $\sim 20\%$ of the line flux. I argue that these components are emitted from the receding (red-shifted) and approaching (blue-shifted) regions of an accretion disk, similar to that seen in Perez and Blundell (2009). If this assumption is correct one extracts an implied accretion disk orbital velocity (along the line of sight) to be approximately 950 ± 55km/s. Unfortunately there may exist a He I line at 21614 Å, corresponding to the transition $7f\ (^3F^{\circ}) - 4d\ (^3D)$, which may contaminate the blue wing of the Brackett-γ complex, and so we cannot definitely conclude that we have detected the accretion disk.

7.4.3 He I 21127Å

No evidence for a pair of lines was found in He I 21127Å. This line was modelled with a single component of FWHM 31 ± 2Å (Figure 7.6) and demonstrates a slightly asymmetric profile with a suggestion of a P Cygni profile. Further analysis was limited by the spectral resolution.

7.4.4 Final Thoughts on CI Cam

Unfortunately these data do not sample sufficient epochs of orbital phase to allow for the diagnosis of truly stationary features. But in the case of CI Cam the data can be interpreted as implying a circumbinary disk, however this cannot be conclusive until the nature of the compact object in this binary has been identified: if the compact object is

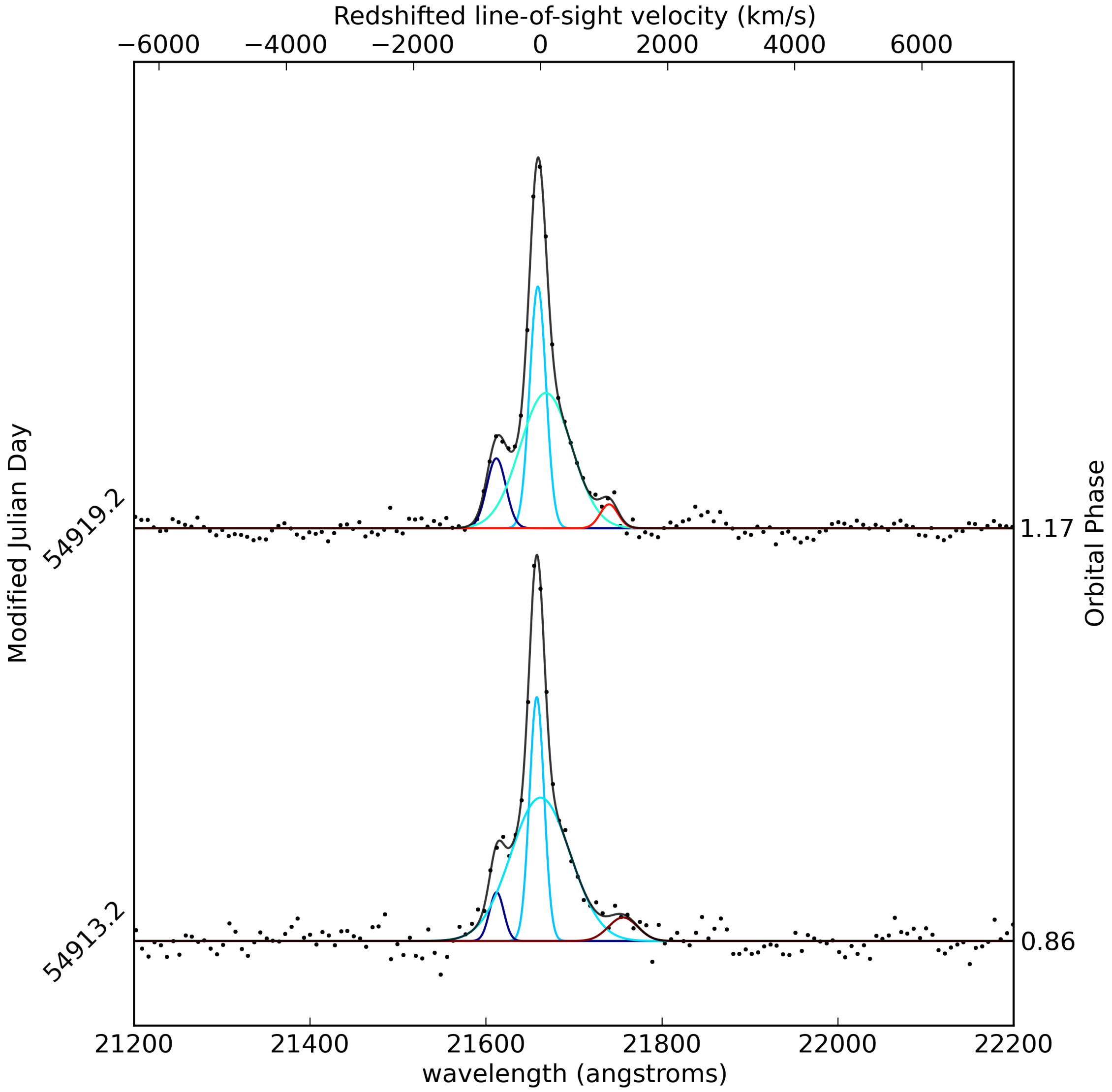

Figure 7.5: The (continuum subtracted) Brackett-γ line of CI Cam

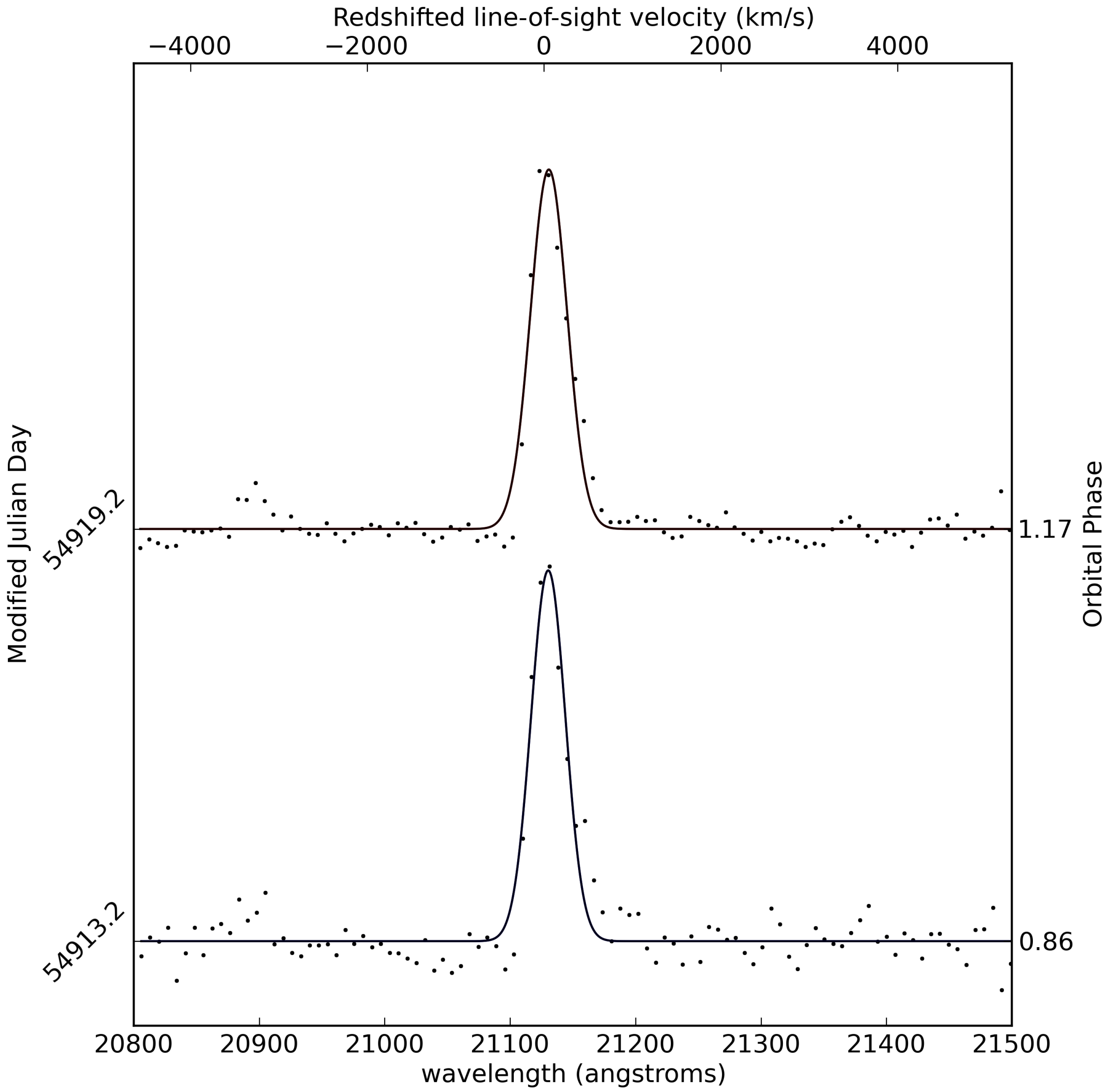

Figure 7.6: The (continuum subtracted) He I 21127Å line of CI Cam

a light neutron star or white dwarf then in principle this component could come from a circumstellar disk around the massive donor. The B[e] supergiant donor star in any case has a strong equatorial wind, which Robinson et al. (2002) argue is the primary source for matter accreting onto the compact object, rather than via Roche-lobe overflow. It is feasible that this equatorial wind may flow out of the system in a circumbinary excretion disk, as imaged by Thureau et al. (2009).

7.5 GRS 1915+105

The variable X-ray source GRS 1915+105 was discovered in August of 1992 by the WATCH all-sky X-ray monitor on board the GRANAT satellite (Castro-Tirado et al., 1992, 1994). The X-ray emission from this object is highly variable. Belloni et al. (2000) identified 12 classes of X-ray emission, corresponding to as many accretion states!

Mirabel et al. (1994) identified an infrared counterpart to GRS 1915+105 but no optical source has been observed due to high optical extinction. Mirabel and Rodríguez (1994) observed that GRS 1915+105 displays the first known “superluminal” jets in the Galaxy — a relativistic effect whereby the projected velocity of the jet on the sky appears to exceed the speed of light.

Greiner et al. (2001b) identified the donor star in the GRS 1915+105 system as spectral type K-M III due to the presence of CO bandheads in high spectral resolution ($\lambda/\delta\lambda = 3000$) near-infrared spectra. Greiner et al. (2001a) used Doppler shifts in these CO bandheads to establish the orbital period of GRS 1915+105 as 33.5 ± 1.5 days. More recently Neil et al. (2007) updated this estimate with an analysis of 7 years of X-ray and near infra red monitoring to give an orbital period of 30.8 ± 0.2 days, with an inferior conjunction of the companion star at MJD 53945.7 ± 0.2, thereafter defining orbital phase zero.

Greiner et al. (2001a) estimate that GRS 1915+105 has a black hole of mass $14 \pm 4\mathrm{M}_\odot$, which is comfortably above the Tolman-Oppenheimer-Volkoff mass limit of $2 - 3\mathrm{M}_\odot$ for a neutron star (Oppenheimer and Volkoff, 1939).

Rahoui et al. (2010) detected polycyclic aromatic hydrocarbon molecules in GRS 1915+105 with mid-infrared spectra from Spitzer. They show the presence of a dust component in all but one of their observations and remark that the structure is likely in a disk, photoionized by the high-energy emission from an accretion disk. Rahoui et al. (2010) remark that dusty disks might be ubiquitous around isolated compact objects and X-ray binaries because of

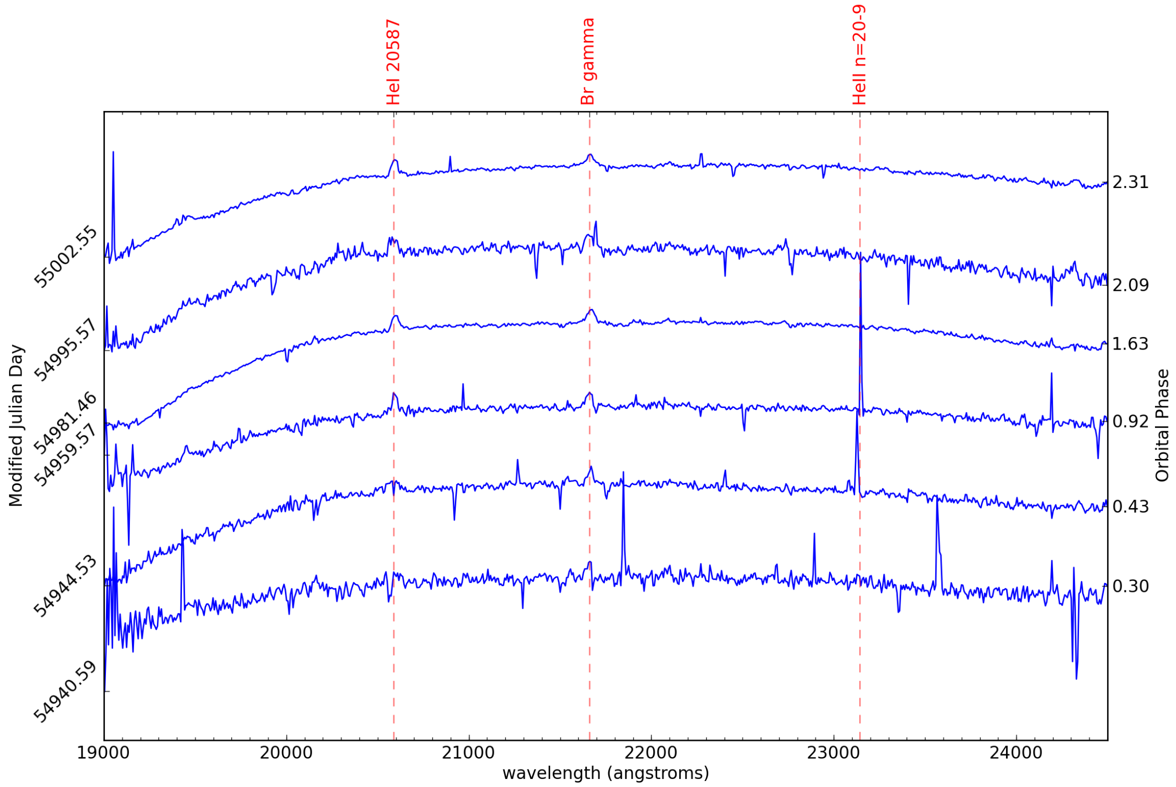

Figure 7.7: K-band spectra of GRS 1915+105

mass transfer during the common envelope phase or material from supernova fallback. I would add outflow from interacting binaries to that list.

7.5.1 Our observations

In Figure 7.7 I plot the spectra from our six observations of GRS 1915+105. These are of variable quality, predominantly due to poor observing conditions at the telescope.

All observations except those made on MJD 54981 and 55002 are of low signal to noise ($\lesssim 4$), although the Brackett-γ and He I 20587 Å lines may still be identified.

The relatively narrow lines in the vicinity of He II ($n = 20 - 9$) in the observations from MJD 54940 and 54959 are unique to these dates. He II lines have been reported intermittently in the literature (Castro-Tirado et al., 1996; Eikenberry et al., 1998; Greiner

Table 7.3: GRS 1915+105 — spectral lines

Species	Transition	Wavelength (Å)
He I	$2p\ (^1P^\circ) - 2s\ (^1S)$	20587
H I	Brackett-γ : $n = 7 - 4$	21661
He II	$n = 20 - 9$	23142

et al., 2001a), leading Eikenberry et al. (1998) to comment that ionised helium may be present at the inner edge of the accretion disk. This region is highly variable, and only visible just prior to an ejection event when the accretion disk should be well extended down to the lowest stable orbit.

I now consider only the observations of reasonable (> 5) signal to noise, taken on MJD 54981 and 55002. The He I line at 20587 Å is measured to have a full width half max of 38 ± 2Å, which may plausibly be identified as a wind.

The Brackett-γ line, having signal to noise (~ 10), is fitted with one gaussian, as plotted in Figure 7.8. Whilst the reduced chi-squared does not allow for additional components, it is clear that this line has un-modelled wings, implying a blend of a broader and a narrower component. Finer spectral resolution and higher signal-to-noise data would be required to fully discriminate the possible blends that may be comprised here.

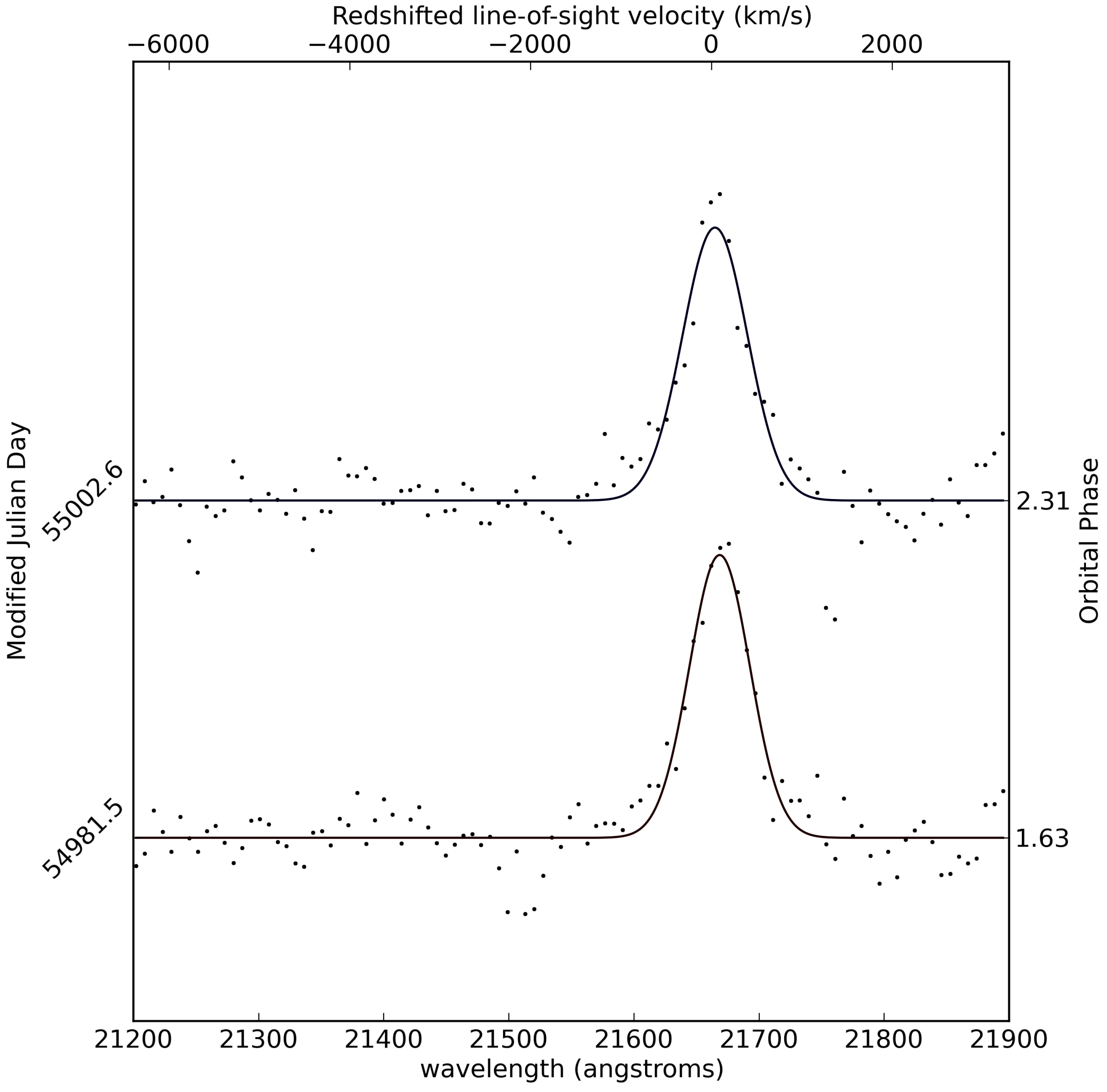

Figure 7.8: The Brackett-γ line of GRS 1915+105

7.6 Cygnus X-3

Cygnus X-3 was discovered by Giacconi et al. (1967) in an X-ray survey of the Cygnus region. It has a sub-day orbital period of approximately 4.8 hours. Stark and Saia (2003) give orbital parameters of period $0.19968462 \pm 6 \times 10^{-8}$ days and an X-ray minima at MJD 40949.89016 ± 0.00064, thereafter defining orbital phase zero.

Cygnus X-3 undergoes radio outbursts and there is evidence of radio jets with velocities in the range $0.3 - 0.9c$ (Mioduszewski et al., 1998b, 2001; Martí et al., 2001).

The nature of the compact object in Cygnus X-3 is debated, but the consensus seems to be converging on a black hole with a recent mass estimate of $10 \pm 3.2\mathrm{M}_{\odot}$ (Shrader et al., 2010). The companion star has been identified as a Wolf-Rayet star with strong, broad emission lines of He I and He II , but no strong hydrogen lines (van Kerkwijk et al., 1992).

With mid-infrared spectroscopy Koch-Miramond et al. (2002) identify a black-body component with temperature $T \sim 250$K which they attribute to thermal emission from circumstellar dust.

7.6.1 Our observations

Due to the 4.79 hour orbital period of Cygnus X-3 (Singh et al., 2001) our six requested observations could be scheduled for the same night and the telescope left on target to minimise slewing overheads. Unfortunately our observing run was interrupted by a Target of Opportunity and was resumed 6 days later. Our spectra are plotted in Figure 7.9, with spectral features identified in Table 7.4.

The structures unique to observations MJD 54950.52 and 54950.54 in the wavelength range $2.0\mu\mathrm{m} < \lambda < 2.1\mu\mathrm{m}$ indicate that Cygnus X-3 was in outburst (see similarity with Fender et al. (1999)).

The signal to noise of these spectra are > 10 but, as mentioned in § 7.1.2, this merely

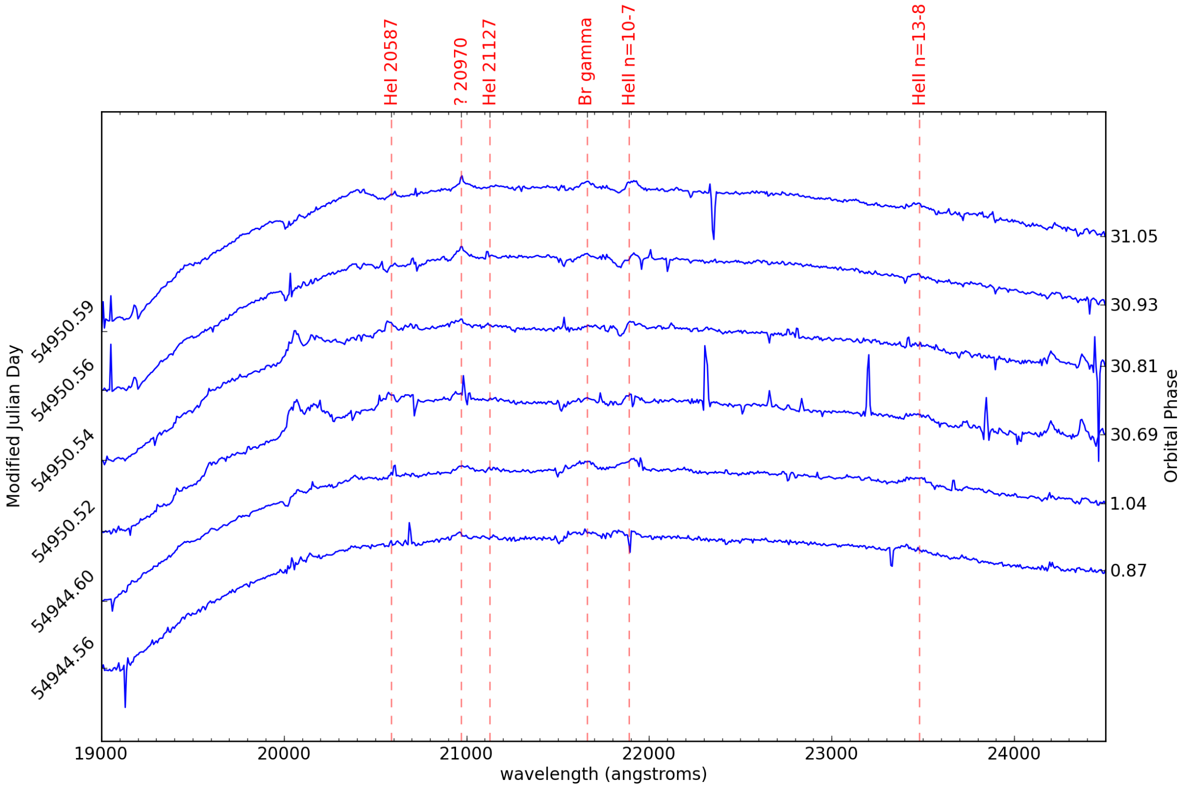

Figure 7.9: K-band spectra of Cygnus X-3

Table 7.4: Cygnus X-3 — spectral lines

Species	Transition	Wavelength (Å)
He I	$2p\ (^1P^\circ) - 2s\ (^1S)$	20587
?	?	20970
He I	$4s\ (^3S) - 3p\ (^3P^\circ)$	21127
H I	Brackett-γ : $n = 7 - 4$	21661
He II	$n = 10 - 7$	21891
He II	$n = 13 - 8$	23480

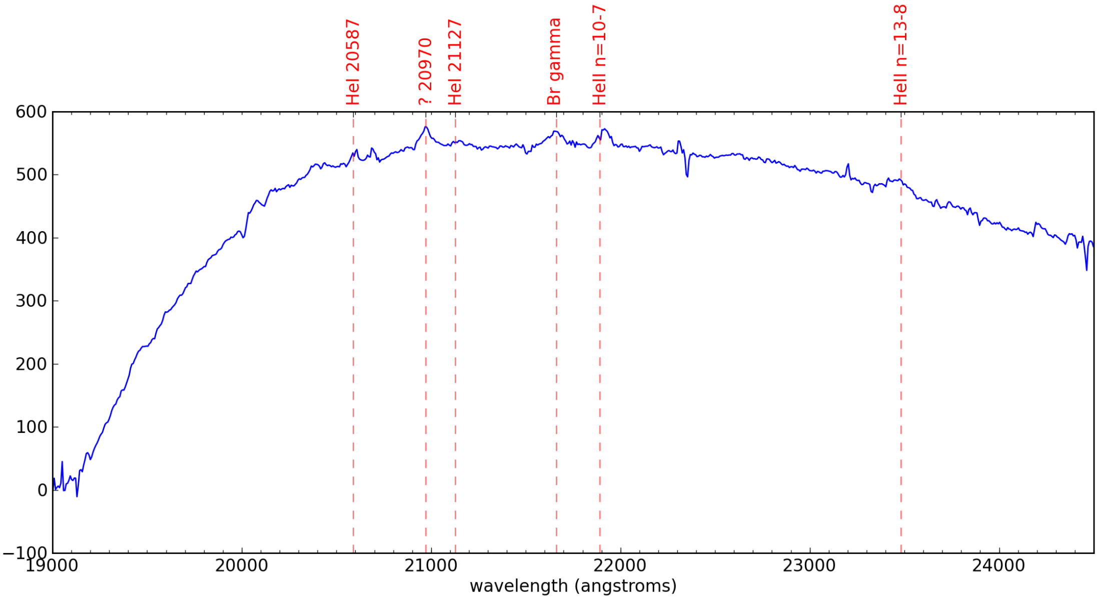

Figure 7.10: Stacked K-band spectra of Cygnus X-3

guarantees detection of the continuum. The spectral lines of Cygnus X-3 were weak during our observations, often comparable to the noise (amplitudes $\lesssim 3\sigma_0$), so we stack the obtained spectra via a signal-to-noise weighted mean to give an orbitally naive spectrum with more signal in the spectral lines, plotted in Figure 7.10. This stacked spectrum enables a better line identification although the line-widths are now broadened by orbital motion.

The unidentified component labelled "?" lies close to the N V emission line $n = 11-10$ at 2.1μm, although if this is the correct line then it is blueshifted by 30Å. This would support the identification of the companion as a WN Wolf-Rayet star.

Unfortunately, due to the low line-strengths in our orbitally resolved spectra, we cannot identify any circumbinary features in Cygnus X-3. To attempt higher spectral resolution observations would be complicated by the short orbital period of 4.79 hours, and so we do not believe that Cygnus X-3 is a good candidate to pursue for follow-up observation.

7.7 Conclusions

A pilot infra-red spectroscopy campaign on three microquasars has produced some suggestive results, particularly in the case of CI Cam, although until more is securely known about this system it is not possible to be definitive. It is certainly clear that the combined challenge of obtaining fine spectral resolution together with fine time sampling is essential to make progress in this area.

Chapter 8

Conclusions

In this thesis I have explored the circumbinary regime and shown it to be a dynamically rich environment. Circumbinary orbits in the elliptically-restricted three-body problem display a nodal libration mechanism in the longitude of the ascending node and inclination to the plane of the binary. This mechanism produces three distinct families of behaviour: close-to-coplanar prograde ($i \sim 0$) and retrograde ($i \sim \pi$) orbits which precess in the longitude of the ascending node, and polar orbits ($i \sim \pi/2$ and $W \sim \pm\pi/2$) which have their longitude of the ascending node and inclination coupled to precess about the centre of an island of libration.

I have demonstrated that the structure of circumbinary phase-space is dependent on binary eccentricity, but not orbital radius. Whilst this is perhaps counterintuitive it is supported by the analytic model of Farago and Laskar (2010). I have experimentally determined a critical angle which defines the location of the separatrix as a function of e_{b}. However, the exact details of motion in the $i - W$ plane, such as the period of precession, have a deep dependency on other factors such as binary mass fraction and test particle orbital radius.

The analytic time-averaged quadrupolar model of Farago and Laskar (2010) provides an excellent description of the behaviours of circumbinary orbits at radii $\geq 50a_{\mathrm{b}}$. I have shown that their model becomes inaccurate to greater than 1% at orbital radii $\leq 5a_{\mathrm{b}}$, and especially in cases of high binary eccentricity.

I have demonstrated that circumbinary phase space is a surprisingly stable place, where long-lived orbits may exist as close to the binary system as 2 or $3a_{\mathrm{b}}$. This work is the first dynamically-aware exploration of inclined circumbinary orbital stability, taking into account the circumbinary nodal libration and resulting phase-space structure.

I have found that there is no definite radius which divides stable and unstable orbits, and that more general derived concepts of zones of partial stability fail to describe the complex structure in stability across phase-space. I therefore present Figure 4.2 as an atlas of circumbinary stability as a function of (i) binary eccentricity, (ii) binary mass fraction, (iii) orbital inclination, and (iv) orbital radius. The results presented in Figure 4.2 provide a map of the regions of circumbinary phase space where we may find long-lived structures, such as disks or planets.

I have applied my theoretical work on circumbinary dynamics and stability to analyse the precessing radio-ruff of the microquasar SS433, which may originate from a circumbinary excretion disk. The observed ruff precession may be explained by a precessing inclined circumbinary disk which obeys the librating behaviour explored in Chapter 3.

SS433's circumbinary disk is thought to be fed by mass overflow across the L2 point and is present at the innermost permitted orbits. This structure represents a significant new component to the system as it is aware of the mass flows within (and emanating from) the internal binary.

The existence of the circumbinary disk around the microquasar SS433 led me to investigate whether circumbinary disks may be a common feature of microquasars. My pilot study of three microquasars via infrared spectroscopy of the Brackett-γ emission line has demonstrated that features within the Brackett-γ complex may be suggestive of a circumbinary origin, however these pilot studies require higher spectral and temporal resolution follow-up observations to ensure that the identified components are truly stationary in wavelength.

8.1 Future work

I believe that the next phase in the theoretical investigation of circumbinary behaviour should be to consider whole and self-gravitating circumbinary disks with hydrodynamic simulations. It is vital to verify that large-scale structures obey the librating behaviour observed with massless test particles. Such simulations may possibly constrain the dynamic mass flows observed in the microquasar SS433.

We have been awarded a long-term VLBI monitoring study to track the precession of SS433s ruff over the coming years. This will test the predictive capabilities of the inclined circumbinary disk model.

And finally I propose to add to the pilot study of Chapter 7 whilst seeking follow-up, higher spatial and temporal resolution spectroscopy of the promising candidates. These targeted observations could be carried out with the instrument CRIRES on the Very Large Telescope.

8.2 Final words

The circumbinary regime has proved to be a dynamic and surprisingly stable environment. With the first confirmed detection of a circumbinary planet (Doyle et al., 2011), and given the plentiful observations of circumbinary disks around young and evolved binaries, we should not presume any given binary system to lack a circumbinary component unless otherwise demonstrated. Such a component may be a source of obscuration, emission, inflow or outflow.

Appendix A

Appendix

A.1 Redshift

The wavelength of light received at a telescope is shifted via the Doppler effect if there is relative motion between the source and observer.

Consider the star in Figure A.1 which emits light of frequency f_{em} and wavelength λ_{em} ($c = f\lambda$, where c is the speed of light). This star is moving away from an observer with velocity of v. It emits the peak of a wave of light at some position A and the successive peak at some position B. The time elapsed between these two events τ_{em} is given by

$$\tau_{\mathrm{em}} = 1/f_{\mathrm{em}} = \lambda_{\mathrm{em}}/c, \tag{A.1}$$

and in that time the star moves a distance

$$d = v\tau_{\mathrm{em}}. \tag{A.2}$$

The observer meanwhile receives the peak of light emitted by the star at A, but the following peak must travel an additional distance d, which takes a small extra time $\delta t = d/c$.

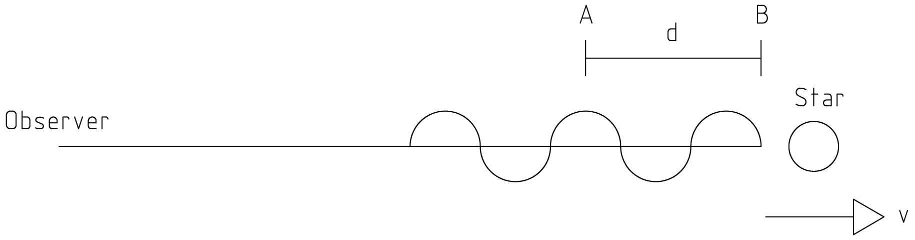

Figure A.1: Redshift

The time that the observer measures between the two peaks of light is therefore

$$\tau_{\text{obs}} = \tau_{\text{em}} + \delta t = \tau_{\text{em}}(1 + v/c). \tag{A.3}$$

The observer will infer a wavelength

$$\lambda_{\text{obs}} = c\tau_{\text{obs}} = c\tau_{\text{em}}(1 + v/c) = \lambda_{\text{em}}(1 + v/c). \tag{A.4}$$

We define the “redshift” z as

$$z = \frac{\lambda_{\text{obs}} - \lambda_{\text{em}}}{\lambda_{\text{em}}} = \frac{v}{c}. \tag{A.5}$$

Astronomical objects which are moving towards us appear to emit shorter wavelengths (their light is “blueshifted”), whilst receding objects are “redshifted”. The above considerations apply to line of sight velocities, and at non-relativistic speeds. As $v \to c$ we must consider additional terms to compensate for relativistic effects.

A.2 P Cygni feature

The characteristic P Cygni profile is manifested as a steep absorption feature in the blue-wing of an asymmetric spectral line. The presence of a P Cygni profile is considered to diagnose outflowing material.

The physical mechanism which causes the P Cygni profile is material along the line of sight between source and observer which selectively absorbs passing photons. If this absorbing material is moving at sufficient speed towards the observer then it experiences the light emitted by the source to be redshifted, and hence selectively absorbs bluer photons, reducing the blue flux arriving at the observer.

Bibliography

G. O. Abell and B. Margon. A kinematic model for SS433. *Nature*, volume 279, page 701, 1979.

S. Abramowitz. *Handbook of Mathematical Functions.* Dover Publications, 1964.

F. Aharonian, A. G. Akhperjanian, K.-M. Aye, A. R. Bazer-Bachi, M. Beilicke, W. Benbow, D. Berge, P. Berghaus, K. Bernlöhr, C. Boisson, et al. Discovery of Very High Energy Gamma Rays Associated with an X-ray Binary. *Science*, volume 309, page 746, 2005.

P. Artymowicz and S. H. Lubow. Dynamics of binary-disk interaction. 1: Resonances and disk gap sizes. *ApJ*, volume 421, page 651, 1994.

P. Artymowicz and S. H. Lubow. Mass Flow through Gaps in Circumbinary Disks. *ApJ Lett.*, volume 467, 1996.

E. A. Barsukova, N. V. Borisov, A. N. Burenkov, V. P. Goranskii, V. G. Klochkova, and N. V. Metlova. Photometry and spectroscopy of CI camelpardalis from 1998 - 2005. *Astronomy Reports*, volume 50, page 664, 2006.

E. A. Barsukova, N. V. Borisov, A. N. Burenkov, V. G. Klochkova, V. P. Goranskij, and N. V. Metlova. The orbital period of CI Cam (XTE J0421+560). *The Astronomer's Telegram*, volume 416, 2005.

M. C. Begelman and C. F. McKee. Compton heated winds and coronae above accretion disks. II Radiative transfer and observable consequences. *ApJ*, volume 271, page 89, 1983.

M. C. Begelman, C. F. McKee, and G. A. Shields. Compton heated winds and coronae above accretion disks. I Dynamics. *ApJ*, volume 271, page 70, 1983.

T. Belloni, S. Dieters, M. E. van den Ancker, R. P. Fender, D. W. Fox, B. A. Harmon, M. van der Klis, J. M. Kommers, W. H. G. Lewin, and J. van Paradijs. On the Nature of XTE J0421+560/CI Camelopardalis. *ApJ*, volume 527, page 345, 1999.

T. Belloni, M. Klein-Wolt, M. Méndez, M. van der Klis, and J. van Paradijs. A model-independent analysis of the variability of GRS 1915+105. *A&A*, volume 355, page 271, 2000.

K. Beuermann, J. Buhlmann, J. Diese, S. Dreizler, F. V. Hessman, T.-O. Husser, G. F. Miller, N. Nickol, R. Pons, D. Ruhr, et al. The giant planet orbiting the cataclysmic binary DP Leonis. *A&A*, volume 526, 2011.

K. M. Blundell. Radio-loud and radio-quiet quasars: one population, different epochs of observation. In *ASP Conference Series*. 2008.

K. M. Blundell and M. G. Bowler. Symmetry in the changing jets of ss 433 and its true distance from us. *ApJ Lett.*, volume 616, page L159, 2004.

K. M. Blundell and M. G. Bowler. Jet Velocity in SS 433: Its Anticorrelation with Precession-Cone Angle and Dependence on Orbital Phase. *ApJ Lett.*, volume 622, page L129, 2005.

K. M. Blundell, M. G. Bowler, and L. Schmidtobreick. Fluctuations and symmetry in the speed and direction of the jets of SS 433 on different timescales. *A&A*, volume 474, page 903, 2007.

K. M. Blundell, M. G. Bowler, and L. Schmidtobreick. SS 433: Observation of the circumbinary disk and extraction of the system mass. *ApJ Lett.*, volume 678, page L47, 2008.

K. M. Blundell, A. Mioduszewski, T. Muxlow, P. Podsiadlowski, and M. Rupen. Images of an equatorial outflow in SS433. *ApJ Lett.*, volume 562, page L79, 2001.

J. A. Cardelli, G. C. Clayton, and J. S. Mathis. The relationship between infrared, optical, and ultraviolet extinction. *ApJ*, volume 345, page 245, 1989.

A. J. Castro-Tirado, S. Brandt, and N. Lund. GRS 1915+105. *IAU Circ.*, volume 5590, page 2, 1992.

A. J. Castro-Tirado, S. Brandt, N. Lund, I. Lapshov, R. A. Sunyaev, A. A. Shlyapnikov, S. Guziy, and E. P. Pavlenko. Discovery and observations by watch of the X-ray transient GRS 1915+105. *ApJS*, volume 92, page 469, 1994.

A. J. Castro-Tirado, T. R. Geballe, and N. Lund. Infrared Spectroscopy of the Superluminal Galactic Source GRS 1915+105 During the September 1994 Outburst. *ApJ Lett.*, volume 461, page L99, 1996.

A. N. Cox. *Allen's astrophysical quantities.* The Athlone Press, London, UK, 2000.

D. Crampton, A. P. Cowley, and J. B. Hutchings. The probable binary nature of SS 433. *ApJ Lett.*, volume 235, page L131, 1980.

R. M. Cutri, M. F. Skrutskie, S. van Dyk, C. A. Beichman, J. M. Carpenter, T. Chester, L. Cambresy, T. Evans, J. Fowler, J. Gizis, et al. 2MASS All-Sky Catalog of Point Sources (Cutri+ 2003). *VizieR Online Data Catalog*, volume 2246, 2003.

P. Deroo. Resolving the dusty discs around post-AGB binaries. In *Asymmetrical Planetary Nebulae IV*. 2007.

S. Doolin and K. M. Blundell. The Precession of SS433's Radio Ruff on Long Timescales. *ApJ Lett.*, volume 698, page L23, 2009.

S. Doolin and K. M. Blundell. The Dynamics and Stability of Circumbinary Orbits. *MNRAS*, volume 418, page 2656, 2011.

L. R. Doyle, J. A. Carter, D. C. Fabrycky, R. W. Slawson, S. B. Howell, J. N. Winn, J. A. Orosz, A. Prsa, W. F. Welsh, S. N. Quinn, et al. Kepler-16: A Transiting Circumbinary Planet. *ArXiv e-prints*, 2011.

R. Dvorak. Numerical experiments on planetary orbits in double stars. *Celestial Mechanics*, volume 34, page 369, 1984.

R. Dvorak, C. Froeschle, and C. Froeschle. Stability of outer planetary orbits (p-types) in binaries. *A&A*, volume 226 (1), page 335, 1989.

S. Eikenberry, K. Matthews, T. W. Murphy, Jr., R. W. Nelson, E. H. Morgan, R. A. Remillard, and M. Muno. Spectroscopy of Infrared Flares from the Microquasar GRS 1915+105. *ApJ Lett.*, volume 506, page L31, 1998.

S. S. Eikenberry, P. B. Cameron, B. W. Fierce, D. M. Kull, D. H. Dror, J. R. Houck, and B. Margon. Twenty Years of Timing SS 433. *ApJ*, volume 561, page 1027, 2001.

A. C. Fabian, P. P. Eggleton, J. E. Pringle, and P. Hut. A phenomenological triple star scenario for SS 433. *ApJ*, volume 305, page 333, 1986.

A. C. Fabian and M. J. Rees. SS 433 - A double jet in action. *MNRAS*, volume 187, page 13P, 1979.

S. Fabrika. The jets and supercritical accretion disk in SS433. *Astrophysics and Space Physics Reviews*, volume 12, 2004.

S. N. Fabrika. An extended disc around SS 433. *MNRAS*, volume 261, page 241, 1993.

R. Falomo, A. Boksenberg, E. G. Tanzi, M. Tarenghi, and A. Treves. The complex, variable structure of stationary lines in SS433. *MNRAS*, volume 224, page 323, 1987.

F. Farago and J. Laskar. High-inclination orbits in the secular quadrupolar three-body problem. *MNRAS*, volume 401, page 1189, 2010.

E. Fehlberg. Low order runge-kutta formulas with step control for heat transfer problems. Technical Report NASA-TR-R-315, NASA, 1969.

R. P. Fender, M. M. Hanson, and G. G. Pooley. Infrared spectroscopic variability of Cygnus X-3 in outburst and quiescence. *MNRAS*, volume 308, page 473, 1999.

A. V. Filippenko, R. W. Romani, W. L. W. Sargent, and R. D. Blandford. Possible evidence for disk emission in SS433. *AJ*, 1988.

R. Giacconi, P. Gorenstein, H. Gursky, and J. R. Waters. An X-Ray Survey of the Cygnus Region. *ApJ Lett.*, volume 148, page L119, 1967.

P. T. Goodall, F. Alouani-Bibi, and K. M. Blundell. When microquasar jets and supernova collide: hydrodynamically simulating the SS 433-W 50 interaction. *MNRAS*, volume 414, page 2838, 2011a.

P. T. Goodall, K. M. Blundell, and S. J. Bell Burnell. Probing the history of SS 433's jet kinematics via decade-resolution radio observations of W 50. *MNRAS*, volume 414, page 2828, 2011b.

R. M. Green. *Spherical Astronomy.* Cambridge University Press, 1985.

J. Greiner, J. G. Cuby, and M. J. McCaughrean. An unusually massive stellar black hole in the Galaxy. *Nature*, volume 414, page 522, 2001a.

J. Greiner, J. G. Cuby, M. J. McCaughrean, A. J. Castro-Tirado, and R. E. Mennickent. Identification of the donor in the X-ray binary GRS 1915+105. *A&A*, volume 373, page L37, 2001b.

N. Haghighipour. *Planets in Binary Star Systems*, volume 366 of *Astrophysics and Space Science Library.* Springer, 2010.

R. M. Hjellming and K. J. Johnston. An analysis of the proper motions of SS 433 radio jets. *ApJ Lett.*, volume 246, page L141, 1981.

R. M. Hjellming, A. J. Mioduszewski, E. L. Robinson, W. F. Welsh, M. T. Adams, and M. E. Cornell. XTE J0421+560 and CI Camelopardalis. *IAU Circ.*, volume 6862, page 1, 1998a.

R. M. Hjellming, A. J. Mioduszewski, Y. Ueda, M. Ishida, H. Inoue, T. Dotani, W. H. G. Lewin, and J. Greiner. XTE J0421+560 and CI Camelopardalis. *IAU Circ.*, volume 6872, page 1, 1998b.

K. W. Hodapp, J. B. Jensen, E. M. Irwin, H. Yamada, R. Chung, K. Fletcher, L. Robertson, J. L. Hora, D. A. Simons, W. Mays, et al. The Gemini Near-Infrared Imager (NIRI). *PASP*, volume 115, page 1388, 2003.

M. J. Holman and P. A. Wiegert. Long-term stability of planets in binary systems. *ApJ Lett.*, volume 117, page 621 , 1999.

J. L. Hora, K.-W. Hodapp, E. M. Irwin, T. J. Keller, and T. T. Young. Design of the near-infrared camera for the Gemini telescope. In *Society of Photo-Optical Instrumentation Engineers (SPIE) Conference Series*, (edited by A. M. Fowler), volume 2475 of *Society of Photo-Optical Instrumentation Engineers (SPIE) Conference Series*, page 308. 1995.

K. Horne and T. R. Marsh. Emission line formation in accretion discs. *MNRAS*, volume 218, page 761, 1986.

R. I. Hynes, J. S. Clark, E. A. Barsukova, P. J. Callanan, P. A. Charles, A. Collier Cameron, S. N. Fabrika, M. R. Garcia, C. A. Haswell, K. Horne, et al. Spectroscopic observations of the candidate sgB[e]/X-ray binary CI Camelopardalis. *A&A*, volume 392, page 991, 2002.

M. Ishida, K. Morio, and Y. Ueda. Possibility of a White Dwarf as the Accreting Compact Star in CI Camelopardalis (=XTE J0421+560). *ApJ*, volume 601, page 1088, 2004.

J. I. Katz, S. F. Anderson, S. A. Grandi, and B. Margon. Nodding motions of accretion rings and disks - A short-term period in SS 433. *ApJ*, volume 260, page 780, 1982.

J. C. Kemp, G. D. Henson, D. J. Kraus, L. C. Carroll, I. S. Beardsley, K. Takagishi, J. Jugaku, M. Matsuoka, E. M. Leibowitz, T. Mazeh, et al. Ss 433 - a 6 year photometric record. *ApJ*, volume 305, page 805, 1986.

L. Koch-Miramond, P. Ábrahám, Y. Fuchs, J.-M. Bonnet-Bidaud, and A. Claret. A 2.4-12 mu m spectrophotometric study with ISO of Cygnus X-3 in quiescence. *A&A*, volume 396, page 877, 2002.

Y. Kozai. Secular perturbations of asteroids with high inclination and eccentricity. *AJ*, volume 67, page 591, 1962.

L. D. Landau and E. M. Lifshitz. *Mechanics*. Butterworth-Heinemann, 1969.

J. W. Lee, S. Kim, C. Kim, R. H. Koch, C. Lee, H. Kim, and J. Park. The sdB+M Eclipsing System HW Virginis and its Circumbinary Planets. *ApJ*, volume 137, page 3181, 2009.

L. A. Lopez, H. L. Marshall, C. R. Canizares, N. S. Schulz, and J. F. Kane. Determining the Nature of the SS 433 Binary from an X-Ray Spectrum during Eclipse. *ApJ*, volume 650, page 338, 2006.

S. D. Lord. Nasa technical memorandum 103957. Technical report, NASA, 1992.

B. Margon, S. A. Grandi, and R. A. Downes. The 164 and 13 day periods of SS 433 - Confirmation of the kinematic model. *ApJ*, volume 241, page 306, 1980.

J. Martí, J. M. Paredes, and M. Peracaula. Development of a two-sided relativistic jet in Cygnus X-3. *A&A*, volume 375, page 476, 2001.

C. McCabe, G. Duchene, and A. M. Ghez. Nicmos images of the gg tauri circumbinary disk. *ApJ*, volume 575, page 974, 2002.

M. Milgrom. On the interpretation of the large variations in the line positions in SS433. *A&A*, volume 76, page L3, 1979.

J. C. A. Miller-Jones, E. Gallo, M. P. Rupen, A. J. Mioduszewski, W. Brisken, R. P. Fender, P. G. Jonker, and T. J. Maccarone. Zooming in on a sleeping giant: milliarcsecond High Sensitivity Array imaging of the black hole binary V404 Cyg in quiescence. *MNRAS*, volume 388, page 1751, 2008.

A. J. Mioduszewski, R. M. Hjellming, and M. P. Rupen. VLBI Images of Relativistic Galactic Jet Sources: SS433 and CI Cam. In *American Astronomical Society Meeting Abstracts #192*, volume 30 of *Bulletin of the American Astronomical Society*, page 930. 1998a.

A. J. Mioduszewski, R. M. Hjellming, M. P. Rupen, E. B. Waltman, G. G. Pooley, F. D. Ghigo, and R. P. Fender. An Image of a Highly Relativistic Jet from a Large Flare in the X-Ray Binary CYG X-3. In *IAU Colloq. 164: Radio Emission from Galactic and Extragalactic Compact Sources*, (edited by J. A. Zensus, G. B. Taylor, & J. M. Wrobel), volume 144 of *Astronomical Society of the Pacific Conference Series*, page 351. 1998b.

A. J. Mioduszewski, M. P. Rupen, R. M. Hjellming, G. G. Pooley, and E. B. Waltman. A One-sided Highly Relativistic Jet from Cygnus X-3. *ApJ*, volume 553, page 766, 2001.

A. J. Mioduszewski, M. P. Rupen, R. C. Walker, K. M. Schillemat, and G. B. Taylor. A summer of ss433: Forty days of vlba imaging. In *Bulletin of the American Astronomical Society*, volume 36, page 967. 2004.

I. F. Mirabel. Microquasars. *Mem. Soc. Astron. Italiana*, volume 82, page 14, 2011.

I. F. Mirabel, P. A. Duc, P. A. Rodriguez, R. Teyssier, J. Paul, A. Claret, M. Auriere, D. Golombek, and J. Marti. The radio/infrared counterpart of the hard X-ray transient in Aquila: A possible source of repeated soft gamma-ray bursts. *A&A*, volume 282, page L17, 1994.

I. F. Mirabel and L. F. Rodríguez. A superluminal source in the Galaxy. *Nature*, volume 371, page 46, 1994.

I. F. Mirabel and L. F. Rodríguez. Sources of Relativistic Jets in the Galaxy. *ARA&A*, volume 37, page 409, 1999.

J.-L. Monin, C. J. Clarke, L. Prato, and C. McCabe. Disk Evolution in Young Binaries: From Observations to Theory. *Protostars and Planets V*, page 395, 2007.

A. Morbidelli. *Modern celestial mechanics : aspects of solar system dynamics*. CRC Press, 2002.

Z. E. Musielak, M. Cuntz, E. A. Marshall, and T. D. Stuit. Stability of planetary orbits in binary systems. *A&A*, volume 434, page 355, 2005.

E. T. Neil, C. D. Bailyn, and B. E. Cobb. Infrared Monitoring of the Microquasar GRS 1915+105: Detection of Orbital and Superhump Signatures. *ApJ*, volume 657, page 409, 2007.

I. Newton, A. Motte, and J. Machin. *The mathematical principles of natural philosophy*. Number v. 1 in The Mathematical Principles of Natural Philosophy. Printed for B. Motte, 1729.

C. Nipoti, K. M. Blundell, and J. Binney. Radio-loud flares from microquasars and radio-loudness of quasars. *MNRAS*, volume 361 (633), 2005.

J. R. Oppenheimer and G. M. Volkoff. On Massive Neutron Cores. *Physical Review*, volume 55, page 374, 1939.

Z. Paragi, I. Fejes, R. C. Vermeulen, R. T. Schilizzi, R. E. Spencer, and A. M. Stirling. The Equatorial Outflow of SS 433. In *Proceedings of the 6th EVN Symposium*, (edited by E. Ros, R. W. Porcas, A. P. Lobanov, and J. A. Zensus), page 263. 2002.

Z. Paragi, R. C. Vermeulen, I. Fejes, R. T. Schilizzi, R. E. Spencer, and A. M. Stirling. The inner radio jet region and the complex environment of ss433. *Astronomy and Astrophysics*, volume 348, page 910, 1999.

S. Perez and K. M. Blundell. Inflow and outflow from the accretion disc of the microquasar SS 433: Ukirt spectroscopy. *MNRAS*, volume 397, 2009.

S. Perez M. and K. M. Blundell. SS433's circumbinary ring and accretion disc viewed through its attenuating disc wind. *MNRAS*, volume 408, page 2, 2010.

E. Pilat-Lohinger, B. Funk, and R. Dvorak. Stability limits in double stars: a study of inclined planetary orbits. *A&A*, volume 400, page 1085, 2003.

E. Pilat-Lohinger, B. Funk, F. Freistetter, and R. Dvorak. Stability of planetary orbits in double stars. In *Exo-Astrobiology*, (edited by H. Lacoste), volume 518 of *ESA Special Publication*, page 547. 2002.

Press, Teukolsky, Vetterling, and Flannery. *Numerical Recipes in C*. Cambridge University Press, 1988.

S.-B. Qian, L. Liu, W.-P. Liao, L.-J. Li, L.-Y. Zhu, Z.-B. Dai, J.-J. He, E.-G. Zhao, J. Zhang, and K. Li. Detection of a planetary system orbiting the eclipsing polar HU Aqr. *MNRAS*, page L241, 2011.

D. Raghavan, T. J. Henry, B. D. Mason, J. P. Subasavage, W.-C. Jao, T. D. Beaulieu, and N. C. Hambly. Two Suns in The Sky: Stellar Multiplicity in Exoplanet Systems. *ApJ*, volume 646, page 523, 2006.

F. Rahoui, S. Chaty, J. Rodriguez, Y. Fuchs, I. F. Mirabel, and G. G. Pooley. Long-term Multi-wavelength Studies of GRS 1915+105. I. A High-energy and Mid-infrared Focus with RXTE/INTEGRAL and Spitzer. *ApJ*, volume 715, page 1191, 2010.

E. Regös, V. C. Bailey, and R. Mardling. Mass transfer in eccentric binary stars. *MNRAS*, volume 358, page 544, 2005.

E. L. Robinson, I. I. Ivans, and W. F. Welsh. High-Dispersion Spectroscopy of the X-Ray Transient RXTE J0421+560 (=CI Camelopardalis) during Outburst. *ApJ*, volume 565, page 1169, 2002.

R. Schwarz, N. Haghighipour, S. Eggl, E. Pilat-Lohinger, and B. Funk. Prospects of the Detection of Circumbinary Planets With Kepler and CoRoT Using the Variations of Eclipse Timing. *ArXiv e-prints*, 2011.

N. I. Shakura and R. A. Sunyaev. Black holes in binary systems. Observational appearance. *A&A*, volume 24, page 337, 1973.

C. R. Shrader, L. Titarchuk, and N. Shaposhnikov. New Evidence for a Black Hole in the Compact Binary Cygnus X-3. *ApJ*, volume 718, page 488, 2010.

N. S. Singh, K. Y. Singh, S. Naik, B. Paul, P. C. Agrawal, A. R. Rao, S. Seetha, and K. Kasturirangan. Observation of X-ray binary Cygnus X-3 by Indian X-ray Astronomy Experiment. *Bulletin of the Astronomical Society of India*, volume 29, page 351, 2001.

M. J. Stark and M. Saia. Doppler Modulation of X-Ray Lines in Cygnus X-3. *ApJ Lett.*, volume 587, page L101, 2003.

P. Stee. How thin B[e] supergiant disks can be? *A&A*, volume 336, page 980, 1998.

C. B. Stephenson and N. Sanduleak. New H-alpha emission stars in the Milky Way. *ApJS*, volume 33, page 459, 1977.

V. Szebehely. Stability of planetary orbits in binary systems. *Celestial Mechanics*, volume 22, page 7, 1980.

V. Szebehely and R. McKenzie. Stability of outer planetary systems. *Celestial Mechanics*, volume 23, page 3, 1981.

N. D. Thureau, J. D. Monnier, W. A. Traub, R. Millan-Gabet, E. Pedretti, J.-P. Berger, M. R. Garcia, F. P. Schloerb, and A.-K. Tannirkulam. Imaging the asymmetric dust shell around CI Cam with long baseline optical interferometry. *MNRAS*, volume 398, page 1309, 2009.

D. Tody. The IRAF Data Reduction and Analysis System. In *Society of Photo-Optical Instrumentation Engineers (SPIE) Conference Series*, (edited by D. L. Crawford), volume 627 of *Society of Photo-Optical Instrumentation Engineers (SPIE) Conference Series*, page 733. 1986.

D. Tody. IRAF in the Nineties. In *Astronomical Data Analysis Software and Systems II*, (edited by R. J. Hanisch, R. J. V. Brissenden, & J. Barnes), volume 52 of *Astronomical Society of the Pacific Conference Series*, page 173. 1993.

M. H. van Kerkwijk, P. A. Charles, T. R. Geballe, D. L. King, G. K. Miley, L. A. Molnar, E. P. J. van den Heuvel, M. van der Klis, and J. van Paradijs. Infrared helium emission lines from Cygnus X-3 suggesting a Wolf-Rayet star companion. *Nature*, volume 355, page 703, 1992.

P. E. Verrier and N. W. Evans. Planetary stability zones in hierarchical triple star systems. *MNRAS*, volume 382, page 1432, 2007.

P. E. Verrier and N. W. Evans. High-inclination planets and asteroids in multistellar systems. *MNRAS*, volume 394, page 1721, 2009.

J. Yan, Q. Liu, and H. Hang. Optical Spectroscopic Observations of CI Camelopardalis. *AJ*, volume 133, page 1478, 2007.